

The effect of size and void configuration on the
stress intensity factor of regular and stochastic
porous materials

Dimitra Touliatou

Department of Mechanical and Aerospace Engineering
University of Strathclyde, Glasgow

A dissertation submitted in partial fulfillment of the requirements for the degree of
Doctor of Philosophy

2019

This thesis is the result of the author's original research. It has been composed by the author and has not been previously submitted for examination which has led to the award of a degree.

The copyright of this thesis belongs to the author under the terms of the United Kingdom Copyright Acts as qualified by University of Strathclyde Regulation 3.50. Due acknowledgement must always be made of the use of any material contained in, or derived from, this thesis.

Abstract

Both, naturally occurring and manufactured porous materials, offer unique and attractive properties. Yet, the inclusion of even a small porosity percentage in materials is usually considered a threat to their integrity and strength. Novel manufacturing technologies, like additive manufacturing, are especially likely to introduce a low percentage of porosity on manufactured components. Additionally, such technologies allow for the manufacturing of smaller, more delicate geometries and mesostructures, whose fracture behaviour deviates from the so far accepted theories.

The aim of this study is to map the relationship between the mesostructural parameters of low to medium porosity brittle materials and their fracture properties in mode I loading. A multi-parameter investigation was conducted and specimens with different topologies of idealised and probabilistic porosity were considered.

Results showed that the use of a single fracture parameter in porous materials is often inadequate. More specifically, prominent size effects were observed, both numerically and experimentally, thereby deviating from the scaling predictions of Linear Elastic Fracture Mechanics under Small Scale Yielding conditions. These deviations are attributed to the loss of K-dominance in the presence of porosity, implying the increased significance of non-singular stresses on the local stress field. Focusing at the scale of the heterogeneity, it was found that each specimen is actually characterised by multiple, local stress intensities, depending on the relative location between the heterogeneity and the crack tip. Design of Experiments was employed to provide insight on how a heterogeneity's location can be designed to either amplify or diminish the stress at the crack tip, thus producing a tailored response.

These findings can act as a theoretical framework on which guidelines for the design of bespoke, novel materials can be drawn, so that porosity may no longer be viewed as a defect, but as a means for damage tolerant design, leading to controlled fracture.

Acknowledgements

The completion of this work would not have been possible without the help and support of a few instrumental people.

Firstly, I would like to thank my supervisor, Dr Marcus Wheel, for giving me the opportunity to do this research degree and his guidance and support throughout the project. Dr Wheel allowed me the space and freedom I needed to work and always asked insightful questions and offered his advice when he felt they were needed. I would also like to thank the engineering technician supervisor, Mr Drew Irvine, for providing his technical expertise during the set-up of my experimental work.

Special thanks to my partner and friend, Michael Frank, for being there for me all the times that I was ready to quit. From motivating me to try new ideas, helping me set realistic work plans, fishing out my coding mistakes and even reading journal papers in his free time to better understand my area of research, his contagious optimism and pure scientific spirit has inspired me to become better and more resilient both as a scientist and a person.

I would also like to express my gratitude to my family for always believing in me and supporting me to pursue my dreams, even if that meant that I could not always be there for them when they needed me. I owe a very important debt to my parents, Panagiota Bourouni and Paul Touliatos, for always encouraging me to aim high while providing me with all the necessary mental and physical resources that I needed to do that, but most importantly for shaping me into the person that I am. I wouldn't have pursued and completed this PhD if I hadn't been influenced by my father's hard working nature and love of engineering and logical problems, and my mother's creativity and restlessness. Finally, I would like to thank my brother, George Touliatos, who would often travel to Glasgow during the duration of my PhD and with his positive and nonchalant personality inspired me to re-evaluate things when I felt pressured.

Contents

Abstract	ii
Acknowledgements	iii
List of Figures	x
List of Tables	xi
Acronyms	xii
Nomenclature	xv
1 Introduction	2
1.1 Lightweight materials and structures	2
1.2 Aims and Objectives	4
1.3 Research output	5
1.4 Thesis Overview	6
2 Fracture mechanics of brittle heterogeneous materials	7
2.1 A brief historical perspective	7
2.2 Basic fracture mechanics concepts	9
2.2.1 Modes of fracture	9
2.2.2 Energy release rate, G	10
2.2.3 Stress intensity factor, K	11
2.2.4 Crack tip plasticity	12
2.3 Linear Elastic Fracture Mechanics	13
2.3.1 K-dominance	13
2.3.2 Stress analysis	14
2.4 Fracture of porous and cellular materials	15
2.4.1 Interaction of crack with near-tip heterogeneities	18
2.5 Size effects in fracture mechanics	20
2.5.1 Models accounting for non-singular stresses	22
2.6 Concluding remarks	23

3	Experimental and numerical methods for the evaluation of the stress intensity at the crack tip	25
3.1	Experimental approach	26
3.1.1	Specimen design	26
3.1.2	Testing procedure	31
3.2	Numerical approach	36
3.2.1	Finite Element model	37
3.2.2	Analysis of numerical results	40
4	Size effects in idealised brittle specimens of low to medium porosity	44
4.1	Finite Element model	45
4.2	Results and Discussion	47
4.2.1	Mesoscale: Porous structure	48
4.2.2	Macroscale: Homogenized material	52
4.3	Conclusions	58
5	Experimental validation and sensitivity to mesostructural changes	59
5.1	Methodology	60
5.1.1	Experimental setup	60
5.1.2	Numerical approach	63
5.2	Experimental results	66
5.3	Effects of manufacturing inaccuracies on the stress intensity at the crack tip	71
5.4	Conclusions	75
6	In-depth investigation of the effect of porosity in applications of engineering interest	77
6.1	Stress intensity variations for porous materials with a random mesostructure	78
6.2	Influence of near-tip isolated heterogeneities in the stress intensity ahead of a crack	83
6.2.1	Size effect in the design of stop-holes for finite size specimens	91
6.2.2	Influence of stress intensity on crack by single stiff inclusion instead of void	92
6.3	Influence of two neighboring near-tip isolated heterogeneities in the stress intensity ahead of a crack	94
6.4	Conclusions	97
7	Conclusions and future work	99
A	Clevis drawing	103
B	Supplementary material for Chapter 4	105
B.1	Additional plots for the mesoscopic behaviour of idealised materials	106

C	Supplementary material for Chapter 5	108
C.1	Quality assurance tables	109
C.2	Experimental force-displacement graphs	112
D	Supplementary material for Chapter 6	114
D.1	Additional contour plots for specimens with voids	115
D.2	Additional contour plots for specimens with stiff inclusions	119
	Bibliography	125

List of Figures

1.1	Heterogeneous, porous specimens can be either natural or man-made, and may be appear in many different size scales.	4
2.1	Different modes of fracture.	9
2.2	Top: Material representation in the atomic level. The crack is formed when the bond between two atoms is broken. Bottom: Lennard-Jones potential as a function of the interatomic distance.	10
2.3	Differences in plane stress (thin section) and plane strain (thick section) due to the crack-front constraint.	12
2.4	Illustration of K-dominant zone.	13
2.5	Scanning Electron Microscopy (SEM) pictures of materials with different porosities.	15
2.6	Different types of lattices. From left to right: kagome, triangular, square and hexagonal.	17
2.7	Crack arresting geometries.	19
2.8	Size effect transition laws: (a) Weibull distribution and (b) Bazant's SEL.	20
2.9	Scaled, homothetic specimens of foam used to demonstrate the size effect.	21
2.10	Photoelastic fringes observed in a homogeneous center-cracked compressed disk.	23
3.1	Schematic and summary of the specimen design specifications.	29
3.2	Top: MATLAB recognition of void pattern. Bottom: Graph produced by MATLAB with all inter-void distances estimated.	30
3.3	Designed (a) and manufactured (b) clevis.	31
3.4	Schematic representation of (a) a general stress tensor and (b) a stress tensor diagonalised by its principal stresses (eigenvalues).	33
3.5	Illustration of a circular polariscope and its elements.	35
3.6	Modelling details of FEA model at different focus levels.	38
3.7	Mesh convergence study.	39
3.8	a) Projection method to estimate the magnitude of the stress intensity at the crack tip, b) Linear extrapolation of the degree of K-significance Λ to estimate the size of the K-dominant zone.	41

4.1	Top: Void topology on idealised specimens. Bottom: Unrefined and near-tip, refined unit cells.	46
4.2	FEA solutions (solid lines) vs analytically determined K-field solution based solely on the on the influence of the SIF (dashed lines).	47
4.3	Fluctuations of SI_N for different crack initiation locations relative to the void.	49
4.4	Sizes $Nc_y = 1 - 6$ for 30% porosity model with triangularly arranged voids equilaterally to the crack.	50
4.5	Variation of SI_N with size of K-dominant zone.	51
4.6	Size effect in fracture of porous materials and dependence of K-dominant zone size with specimen size.	53
4.7	a) Average normalised stress intensity $\overline{SI_N}$ variation with averaged normalised amplitude of $A_{1/2}$ stresses \tilde{C} , b) Inclusion of correction factor $\sqrt{P/Nc_y}$ in graph (a)	55
4.8	Dependence of normalised amplitude of $A_{1/2}$ stresses \tilde{C} with number of cells in y-direction, Nc_y , and specimen porosity, P	56
4.9	Correlation of scaling factor with the geometrical dependency coefficient.	57
5.1	Designed and manufactured specimens.	61
5.2	Experimental setup	62
5.3	FE model with rectangular array, reflecting the topology of the manufactured specimens.	63
5.4	Difference of normalised stress intensity between the models with the triangular (idealised) and the rectangular void topology, for porosities of $P = 29.61\%$ ($d = 2mm$).	64
5.5	Difference between the values of normalised stress intensity as estimated by the projection method and the Beam Theory expression.	65
5.6	Isochromatic fringes in specimens during mode I loading.	67
5.7	Numerical variation in SI_N within unit cell with experimental data points appended for each different size.	69
5.8	Comparison of experimental results with fitted model from Chapter 4.	70
5.9	Models with different void shapes investigated in parametric analysis.	71
5.10	Influence of void shape on size effect of porous materials.	73
5.11	(a) Normalised amplitude of $A_{1/2}$ stresses versus the geometrical factor $1/Nc_yP$ that has been found to uniquely describe them for perfectly circular voids (dashed line represents the homogeneous case), (b) Average normalised stress intensity at the crack tip versus the amplitude of the $A_{1/2}$ stresses, multiplied by the geometrical factor $\sqrt{P/Nc_y}$	74
5.12	All parametric and experimental results against the empirical model of Equation 4.4.	75
6.1	Models of $Nc_y=4$, $d_{av} = 1.64$ and different levels of randomness: (a) Small randomness, (b) Medium randomness, (c) Large randomness.	79
6.2	Results for random models.	81
6.3	Illustration of factors used for DOE.	84

6.4	Contour plots representing the influence of a void with $d_{av} = 1.64mm$ in the near-tip area on the stress intensity at the crack tip for different sizes of specimens (a)-(e).	85
6.5	Contour plots to show the variations of the size of K-dominant zone and the amplitude of non-singular stresses for different locations of the near-tip void and different size specimens.	87
6.6	Pareto chart of effects for all DOE factors against the studied fracture parameters.	88
6.7	Relationship between material's fracture parameters for different specimen sizes.	90
6.8	Effect of stop-holes of different radii on finite size specimens	91
6.9	Results for specimens of $Nc_y = 50$, containing a single stiff inclusion in the near-tip area.	93
6.10	Relationship of fracture parameters for models with a single stiff inclusion	94
6.11	Variations of SI_N for models of different distance combinations between neighbouring voids.	95
6.12	Relationship of fracture parameters for models with two neighbouring voids.	96
A.1	Drawing of manufactured clevis	104
B.1	Additional plots of the mesoscopic stress intensity variation of different specimens, categorised by their value of Nc_y	106
B.2	Additional plots of the mesoscopic stress intensity variation of different specimens, categorised by their value of P	107
C.1	Force-displacement graph for manufactured homogeneous specimens with $d = 0mm$	112
C.2	Force-displacement graph for manufactured specimens with $d = 1.4mm$	113
C.3	Force-displacement graph for manufactured specimens with $d = 2mm$.	113
D.1	Additional graphs for the variations of the amplitude of $A_{1/2}$ stress and the size of K-dominant zone for specimens with voids of $d = 1.64mm$. .	115
D.2	Contour plots of stress intensity variations for specimens with voids of $d = 0.82mm$	116
D.3	Contour plots of the amplitude of $A_{1/2}$ stress variations for specimens with voids of $d = 0.82mm$	117
D.4	Contour plots of the size of K-dominant zone for specimens with voids of $d = 0.82mm$	118
D.5	Contour plots of stress intensity variations for specimens with stiff inclusions of $d = 0.82mm$	119
D.6	Contour plots of the amplitude of $A_{1/2}$ stress variations for specimens with stiff inclusions of $d = 0.82mm$	120
D.7	Contour plots of the size of K-dominant zone for specimens with stiff inclusions of $d = 0.82mm$	121

D.8	Contour plots of stress intensity variations for specimens with stiff inclusions of $d = 1.64mm$	122
D.9	Contour plots of the amplitude of $A_{1/2}$ stress variations for specimens with stiff inclusions of $d = 1.64mm$	123
D.10	Contour plots of the size of K-dominant zone for specimens with stiff inclusions of $d = 1.64mm$	124

List of Tables

3.1	Comparison of K_I values of the homogeneous case estimated analytically, using the interaction integral formulation in ANSYS and using the projection method.	42
4.1	Specimen porosity for each given void radius.	45
6.1	Distribution values used for each randomness level and resulting porosities P for each different average void diameter	79
6.2	Factors and levels used in DOE	83
C.1	Quality assurance of the tested specimens' macroscopic features	110
C.2	Quality assurance of the tested specimens' mesoscopic features as extracted by MATLAB	111

Acronyms

APDL	Ansys Parametric Design Language.	37
AR	Specimen aspect ratio.	63
ASTM	American Society for Testing and Material.	26
BT	Beam Theory.	35
CT	Compact Tension.	26
DCB	Double Cantilever Beam.	27
DOE	Design of Experiments.	83
FE	Finite Element.	63
FEA	Finite Element Analysis.	18
FPZ	Fracture Process Zone.	12
LEFM	Linear Elastic Fracture Mechanics.	13
PMMA	poly(methyl methacrylate).	27
SENB	Single-End-Notch Bending.	26
SIF	Stress Intensity Factor.	14
SSY	Small Scale Yielding.	13

Nomenclature

- A_0 Second, non-singular term in the Williams expansion series. 14
- $A_{1/2}$ Third, non-singular term in the Williams expansion series. 14
- B Specimen thickness. 27
- C Amplitude of the $A_{1/2}$ stresses normalised for crack length. 40
- D_c Geometrical dependency coefficient. 56
- E Young modulus. 11
- E_{11} Young modulus in the fiber direction in composite laminates. 28
- F Applied load. 35
- G Energy release rate. 11
- G_{Ic} Critical energy release rate for mode I loading. 28
- G_c Critical energy release rate. 11
- K Stress intensity factor. 11
- K_{Ic} critical stress intensity factor for mode I loading. 11
- K_I Stress intensity factor for mode I loading. 11
- N_{cy} Number of rows of unit cells in the y direction of each specimen arm. 39
- P Specimen porosity. 37
- Q Weighting function to estimate the significance of the near-tip region. 82
- R Level of randomness. 78
- R_d Level of randomness referring to the void radius. 78
- R_{loc} Level of randomness referring to the void's centroid location. 78

- SI_N Normalised stress intensity. 42
- SR Shape anisotropy ratio of voids. 71
- $Size_x$ Size of unit cell in x direction on the FE model/inter-void distances in x direction on the manufactured specimens. 29
- $Size_y$ Size of unit cell in y direction on the FE model/inter-void distances in y direction on the manufactured specimens. 29
- T T-stress component. 14
- W Specimen length. 27
- Λ Degree of K-dominance. 43
- α Crack length. 27
- α_0 Initial delamination length in composite laminates. 28
- δ Total opening displacement between two specimen arms. 35
- δ_{phase} Phase difference. 34
- λ Wavelength of light wave. 34
- σ_1 First principal stress. 33
- σ_2 Second principal stress. 33
- $\sigma_y^{non-sing}$ Non-singular stresses at the crack tip in the y direction. 43
- σ_y^{sing} Singular stresses at the crack tip in the y direction. 43
- τ_{ij} Component of the stress in the i direction acting on a surface perpendicular to the j direction, where i, j take the values of the coordinate axes.. 32
- θ Angle measured from the positive x -axis in a polar coordinate system. 13
- θ_A Distance of the nearest void to the crack tip from the crack tip. 95
- θ_B Distance of the second void nearest to the crack tip from the crack tip. 95
- \tilde{C} Average normalized amplitude of the $A_{1/2}$ stresses, for relative crack tip locations $sx = 0 - 0.75$. 54
- $\overline{SI_N}$ Average normalised stress intensity, for relative crack tip locations $sx = 0 - 0.75$. 52
- d Void diameter. 29
- d_{av} Average void diameter in models with random porosity. 79
- $dist$ Distance of the voids in the near-tip area from the crack tip. 95

- $dist_A$ Distance of the nearest void to the crack tip from the crack tip. 95
- $dist_B$ Distance of the second void nearest to the crack tip from the crack tip. 95
- h Specimen width. 28
- r Radial distance in a polar coordinate system. 13
- sx Relative crack tip location in x direction within a single unit cell, with 0 and 1 being the limiting values (beginning and end of unit cell respectively). 38
- t The vertical distance between the midplane of the specimen's arm and the loading point. 28
- ν Poisson ratio. 11
- x Component of the cartesian coordinate system in the direction of the crack. 40
- y Component of the cartesian coordinate system in the loading direction. 40

Superscripts

- H Referring to the homogeneous material
- P Referring to the porous material

CHAPTER 1

Introduction

1.1 Lightweight materials and structures

Lightweight materials are ubiquitous in nature. After years of evolution, natural structures have optimised to comprise of the minimum amount of material while maintaining their mechanical strength and stiffness. Load-bearing structures like bones, and porous rocks are characterised by an intricate, internal, cellular structure that allows them to exhibit extraordinary strength while remaining light. For example, the wings of a bird consist of a thin, dense exterior and almost hollow interior reinforced only with a thin network of struts. It is this design of their bones, which allows them to cover a large area, while remaining light and have an increased bending and torsional stiffness, that makes them a remarkable example of nature's architecture. Pith stems and bamboo have achieved a similar effect of high stiffness by the combination of a compliant, binding matrix (e.g. lignin) with stiffer, load-bearing fibers (e.g. cellulose and hemicelluloses). Other materials have developed porous microstructures for functionality reasons, such as fluid transport seen in teeth's dentin or compact bone.

Yet it is only during the last decades that lightweight materials and structures have gathered large amounts of attention both in academic and industrial circles. Especially, with increasing environmental concerns and government regulations, research is focused on materials that allow for more sustainable transportation in the automotive and aerospace industry, as structures of reduced weight immediately translate to reduced CO₂ emissions.

One of the most researched ways to achieve lightweight materials is by reinforcing a

compliant matrix with stiff particles or fibers which could either be randomly dispersed or ordered in laminated layers. These composite materials offer a high stiffness to weight ratio, are easily moldable, resistant to environmental degradation and can be tailored to achieve properties like heat and electricity conductance at a small price compared to more traditional materials. These benefits have made them highly desirable in a number of sectors and research on their properties and optimisation is generously funded.

A different category of lightweight materials is porous and cellular materials. These materials consist of a solid and a gaseous phase, which could either be enclosed in pockets inside the material or be part of an interconnecting network. These materials can achieve even lower densities than composite materials and provide additional benefits like thermal and acoustic insulation, buoyancy and high energy absorption in impact.

Despite their benefits, with a smaller percentage of solid material, there is usually a decline in these materials' strength and stiffness, and failure becomes more likely. In 2003, during take off of the space shuttle Columbia, a large piece of foam from the insulation of the external tank broke off, hit at a large speed and damaged the brittle carbon, heat shielding panels on the orbiter's left wing. The crew and ground engineers operated under the preconception that a piece of foam couldn't damage the shuttle and was not a "safety of flight" issue. Numerical simulations they used to estimate the extent of the damage, modelled ice instead of foam and gave conservative results which, as was later proved, were not accurate. As a result, during reentry superheated gases penetrated the orbiter's wing, which inevitably led to its destruction and the death of all seven crew members.

Since then, research on porous and cellular materials has intensified and their behaviour has become more comprehensible. Still, when referring to a heterogeneous material's properties, it is usually assumed that the specimen's scale is large enough that it can be considered a homogenised medium, characterized by unique mechanical properties applicable at all size scales. Such simplifications are common as all materials can be considered homogeneous at a proper scale. However, even steel, in the microscopic level behaves as a heterogeneous material, governed by its grains' size. Similarly, in porous and cellular materials where the heterogeneities can be observed with the naked eye, the homogenization of their properties can only be considered valid for specimens of larger dimensions, when the dimension of its voids are much smaller than any other macroscopic specimen dimension (Figure 1.1).

With the rise of new, precision manufacturing methods, a definitive turn towards smaller and lighter parts and components has emerged. Additive manufacturing has been one of the main drivers of this trend. Developments on the materials and techniques used in additive manufacturing have allowed for components of intricate, biomimetic

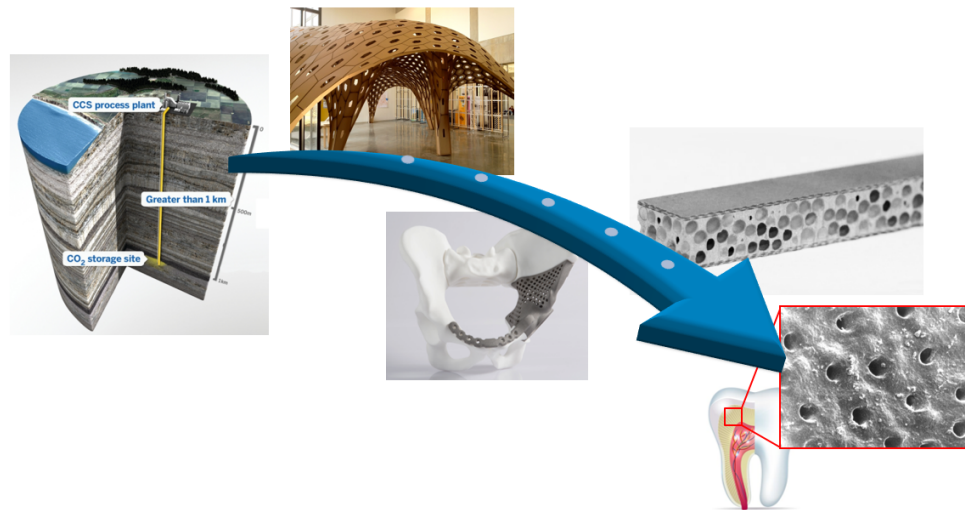


Figure 1.1: Heterogeneous, porous specimens can be either natural or man-made, and may appear in many different size scales. When the size of the heterogeneity becomes comparable to the size of the structure, size effects may appear.

internal structures to be effectively used in high-end applications where weight saving is essential, such as in aerospace. As the size of the manufactured component approaches the size of the heterogeneity, it can no longer be assumed that homogenized material properties apply. Even in the case where porosity is not designed in the material as a means to reduce weight, unwanted porosity can be introduced due to inefficiency of the manufacturing process. If not accounted for, this porosity can act as a stress concentration point and may ultimately lead to the catastrophic failure of the part.

With lightweight materials becoming increasingly more prevalent in engineering, and the shrinking size of structural components, it is imperative that the scaling laws of porous and cellular materials are accurately mapped.

1.2 Aims and Objectives

This study aims to correlate the fracture behaviour of heterogeneous materials in the presence of a long crack, to their mesostructural characteristics. As technologies turn to the minute, particular interest is placed on smaller structures, where the size of the heterogeneities is comparable to the specimen's dimensions. The apt understanding of this size effect and its correlation with the material's intrinsic geometrical properties will provide insight on ways to optimally design a material's mesostructure in order to achieve desired, tailored properties. Finally, this study aims to identify the underlying

cause for the variations observed in order to obtain a more complete understanding of this behaviour.

The following objectives were set in the path to achieve the above goals:

- Carry out a literature review of the broad field of size effects in fracture mechanics. Within the context of this literature review, special notice should be given to theories attempting to explain this size effect.
- Perform simulations of idealised heterogeneous specimens of different sizes to establish the existence of a size effect (proof of concept).
- Conduct experiments in order to provide validation of numerical findings.
- Perform a designed numerical experiment to accurately map stress variations emanating from voids in the vicinity of the crack tip.
- Extend observations to materials and structures of engineering interest.
- Suggest steps to advance findings to a higher technology readiness level (TRL) so that they can be more readily useful to the industry.

1.3 Research output

It was important that the major findings of this study are peer reviewed throughout the duration of this PhD, in order to ensure the validity of each step and receive constructive feedback and suggestions from the academic community to improve this work. Hence, the vast majority of the findings of this PhD have been submitted for publication in peer-reviewed journals as following:

- D. Touliatou, M. A. Wheel, “K-dominance and size effect in mode I fracture of brittle materials with low to medium porosity”, *Engineering Fracture Mechanics*, 2018, <https://doi.org/10.1016/j.engfracmech.2018.06.041>
- D. Touliatou, M. A. Wheel, “Experimental and numerical analysis of size effects on stress intensity in anisotropic porous materials”, *Engineering Failure Analysis* (*in print*)
- D. Touliatou, M. A. Wheel, “On the effect of voids and inclusions in the vicinity of cracks in engineering materials” (*submitted*)

Part of the results of the thesis have also been demonstrated in an oral presentation by the author of this thesis in the 8th International Conference for Engineering Failure Analysis (ICEFA VIII) in Budapest, Hungary.

1.4 Thesis Overview

Chapter 2 comprises a comprehensive literature review on the main concepts that will be mentioned throughout the thesis. The gaps in the literature are clearly marked and the contribution of this PhD in the general field of study is highlighted.

Chapter 3 describes the numerical and experimental methods used throughout the content of this thesis. Although each subsequent chapter relies on different material mesostructures, the thread binding them all together is outlined here.

Chapter 4 acts as an initial proof of concept of the existence of a size effect on the fracture of porous materials. A numerical multi-parametric study of highly idealised materials is conducted and initial suggestions on the underlying cause of the observed size effect are conveyed. An empirical model is also first suggested in this chapter, which will be used as a guide for the rest of the thesis.

Chapter 5 provides experimental validation of the findings of the previous chapter. Due to several observed discrepancies in the geometry of the specimens (caused by manufacturing uncertainties) a numerical study is also employed to investigate how such effects could influence the material's behaviour.

Chapter 6 focuses on materials and structures of engineering interest. Specimens of random topology are studied and their behaviour is broken down to near-tip and boundary effects. In order to better comprehend the influence of a void in the near-tip area, a numerical designed experiment is conducted, highlighting effects of statistical significance on the material's strength. These results are extended to materials with two near-tip voids and their interaction is mapped by an approximated solution. Finally, size effects in materials with inclusions and stop holes are briefly investigated, as an extension of this study.

Chapter 7 concludes this thesis by briefly stating its findings collectively. It is appreciated that this research study covers novel concepts that are still unresolved. Here the next steps required to elevate these theoretical concepts to useful practices are also listed.

CHAPTER 2

Fracture mechanics of brittle heterogeneous materials

2.1 A brief historical perspective

All materials contain flaws in the form of impurities and voids.¹ These flaws act as stress concentration points, which weaken the material and can lead to its catastrophic failure. Fracture mechanics is the engineering field that integrates mathematics and physics in order to study the formation and propagation of these cracks in materials, and their eventual failure. Within the scope of fracture mechanics lies the investigation of the critical load, crack length, and environmental and loading conditions required for a structure to fail. Deep knowledge of these parameters can allow for damage tolerant design, which can prevent many catastrophic fracture events.

Fracture mechanics is a still developing field of science. However, proof of relevant scientific research dates back to the Renaissance. Leonardo Da Vinci and Galileo Galilei had conducted primitive experiments on the fracture of wires and beams, and made initial observations correlating their strength with their geometrical dimensions.

Yet, it wasn't until the 1920s when a theory correlating the fracture of solids with flaw size was officially formed by A.A. Griffith, thus pioneering the field of fracture mechanics. Griffith added on the work of Inglis, who had already formulated an analytical solution for the stress concentration around an ellipse. Inglis's work, however, contained a paradox: when the radius of the ellipse became zero (resembling a crack)

¹The first sections of this chapter contain basic information which can be found in most textbooks and thus references may be scarce. The main references used here were: [1–3]

stress became infinite, which meant that any material containing a crack would fracture even at a infinitesimal load. Griffith had the insight to additionally include the energy of the crack surface in the analysis, in order to account for that singularity. He claimed that, in accordance with the first law of thermodynamics, the crack would become unstable and propagate when the strain energy released from a small advancement of the crack exceeds the increase of the surface energy. He then validated his solution by conducting experiments with glass tubes; though, experiments with metals were unsuccessful.

Griffith's solution assumed that the surface energy of the material was the threshold energy over which the crack would advance, which is true for brittle materials. However, metals exhibit extensive local plastic phenomena around the crack tip, dissipating the work of fracture and increasing the energy required to advance the crack. In 1948, G.R. Irwin noticed that discrepancy and added the term of plastic deformation on the crack tip in Griffith's solution. A few years later, by re-writing Griffith's equation in a more practical form, Irwin introduced the concept of the energy release rate (see also Section 2.2.2). Based on this parameter, he then developed an equation to explicitly approximate the stress at the crack tip using only a single parameter related to the energy release rate, termed the stress intensity factor (see also Section 2.2.3). Due to his contribution in the field, Irwin was given the unofficial title "father of fracture mechanics".

The main focus of research conducted during the following couple of decades was crack tip plasticity. A number of researchers attempted to formulate universal criteria describing the behaviour of non-linear fracture. The most popular ones, was the introduction of the J-integral by Rice in the US and crack-tip opening displacement (CTOD) by Wells in the UK. Even today both criteria are still applied throughout the world to characterise a range of materials.

During that time, the concepts of fracture mechanics were beginning to become established in industrial circles. In 1982, the cost of fracture in the US for 1978 was estimated at \$119 billions, which approximated almost 4% of the gross national product. This economical pitfall pushed for more research in this domain. Meanwhile, the studies conducted then posed serious questions on the validity of a single-parameter criterion for fracture. With the increasing use of polymers, which are characterised by a viscous nature, time-dependent fracture was one of the main areas of interest. At the same time, prominent discrepancies between the behaviour of testing specimens and real structures stimulated a number of studies on geometry dependent fracture and size effects. This will be further addressed in Section 2.5.

More recently, the development of computers has allowed for improved models and

many scientists have turned to the study of fracture mechanics in the context of engineering applications. The study of interface and nanoscale fracture also became possible as a result of the increased computational resources available.

2.2 Basic fracture mechanics concepts

A very short, compressed description of central concepts of fracture mechanics is provided here as background.

2.2.1 Modes of fracture

A material containing a crack can be subjected to any of the following types of loading or combinations of them, referred to as mixed modes:

- Mode I: Opening mode. Failure results from the tensile stress, applied normal to the crack surface (Figure 2.1, left). This is the most commonly encountered and widely researched mode of fracture. This study will also exclusively focus on this type of fracture.
- Mode II: Sliding mode or in-plane shear. In this case, the stress is applied parallel to the crack surface and tends to slide one surface with respect to the other (Figure 2.1, center).
- Mode III: Tearing mode or out-of-plane shear. Both the crack surface and the crack front are parallel to the applied stress (Figure 2.1, right).

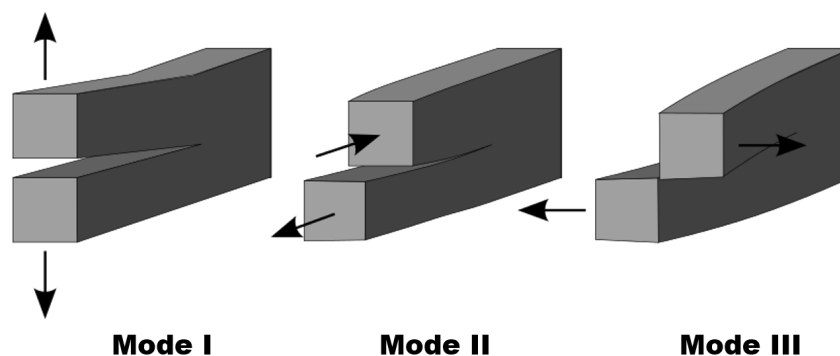


Figure 2.1: Different modes of fracture.

2.2.2 Energy release rate, G

Fracture occurs when the bond between two atoms breaks, resulting in a crack advancement equal to the interatomic distance (Figure 2.2). The increase in the area of the free surface is accompanied by two energetically competing processes: the first is a linear increase in the surface energy, corresponding to the energy required to break the atomic bonds, while the second is a quadratic decrease in energy, corresponding to the release of strain energy. The net change of the total energy with respect to an

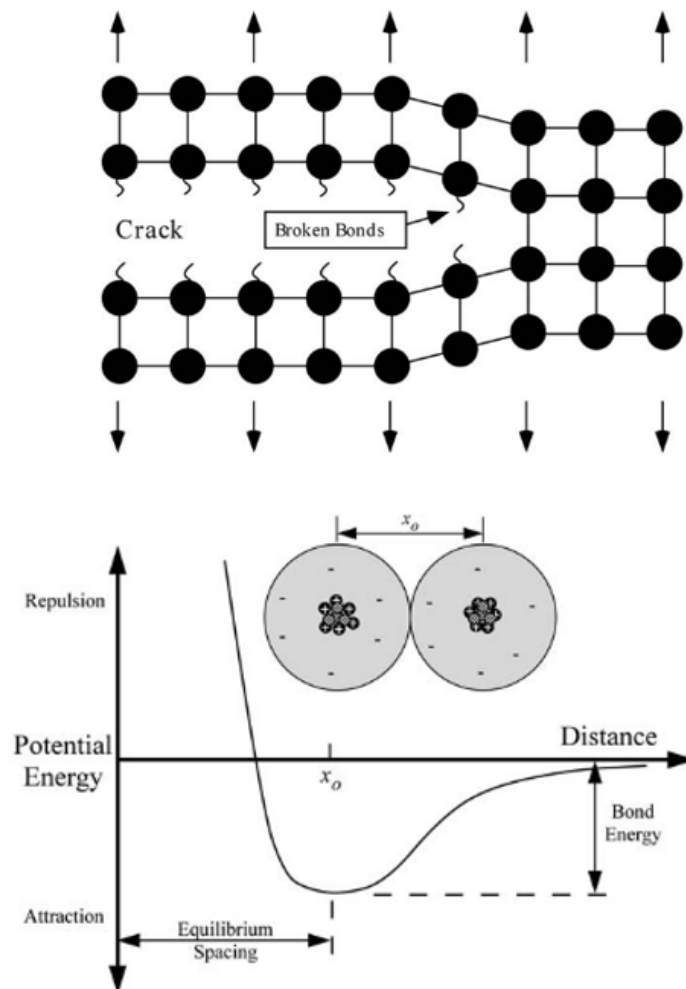


Figure 2.2: Top: Material representation in the atomic level. The crack is formed when the bond between two atoms is broken. Bottom: Lennard-Jones potential as a function of the interatomic distance. Reproduced from [1].

infinitesimal increment of the crack length is termed the energy release rate, G .

The energy release rate was used as the first fracture criterion, stating that when the energy release rate, G , exceeds a critical value, G_c , the crack advances spontaneously. This criterion constitutes a global approach to fracture, since the potential energy of the entire system is taken into account.

2.2.3 Stress intensity factor, K

An alternative, local failure criterion was introduced by Irwin in 1957. Irwin focused on the displacements and stresses in the vicinity of the crack-tip. and noticed that they can always be described as a function of the term (EG/π) , which he termed the stress intensity parameter. This parameter was later replaced by the stress intensity factor, K , which for linear elastic materials is correlated with G as:

$$K = \sqrt{GE'} \quad (2.1)$$

, where

$$E' = \begin{cases} E & , \text{for plane stress} \\ \frac{E}{1-\nu^2} & , \text{for plane strain} \end{cases} \quad (2.2)$$

In Equation 2.2, E represents the material's Young Modulus and ν is the Poisson ratio. Note that this study investigates specimens exclusively in plane strain, for reasons that will be clarified on section 2.2.4.

Fracture toughness is a material property which describes the ability of a material to resist fracture. In linear elastic materials, the stress intensity factor, K , is the most common measure of material's toughness and represents the amplitude of the singularity in the near-tip region. The value of the stress intensity factor for a given material is a function of the specimen's geometry, the applied load and mode of loading.

The mode that corresponds to the stress intensity factor is denoted by the appropriate subscript (e.g. K_I refers to the mode I type of fracture etc.). The critical value of the stress intensity factor, K_{Ic} for mode I, represents the stress value at the crack tip which results in crack propagation and fracture. K_{Ic} is thus considered a unique material property.

2.2.4 Crack tip plasticity

Equation 2.1 correlates the stresses and displacements at the crack tip directly with the resulting change in potential energy and implies that all of this energy focuses on the crack tip to break the bond between the crack tip's atoms. In real materials however, the work produced by the force applied on the specimen may instead be dissipated in a diffused zone ahead of the crack tip, leading to non-linear phenomena like crazing, shearing, micro-cracks and plasticity. This zone is referred to as the Plastic Zone in ductile materials or Fracture Process Zone (FPZ) in quasi-brittle materials.

The size of this non-linear zone is considered minimal in linear elastic, brittle materials. However, its size has been found to be correlated with the level of constraint of the material on the crack front. For example, in plane stress (the condition in which the only non-zero components of stress lie in a single plane [4], which is usually dominant in thin specimens, Figure 2.3, center), the material adjacent to the sides of the specimen can plastically deform laterally, since there is no constraint from surrounding material. This would result in shear lips, governed by ductile fracture, which are characterised by a varying value of stress intensity factor, dependent on non-linear phenomena. In plane strain, on the contrary, (the condition in which the only non-zero components of strain lie in a single plane [4], which is usually dominant in thick specimens, Figure 2.3, right), the region where the shear, plasticity governed, lips are formed only covers a small portion of the crack front due to the lack of constraint. This leads to a predominantly brittle fracture.

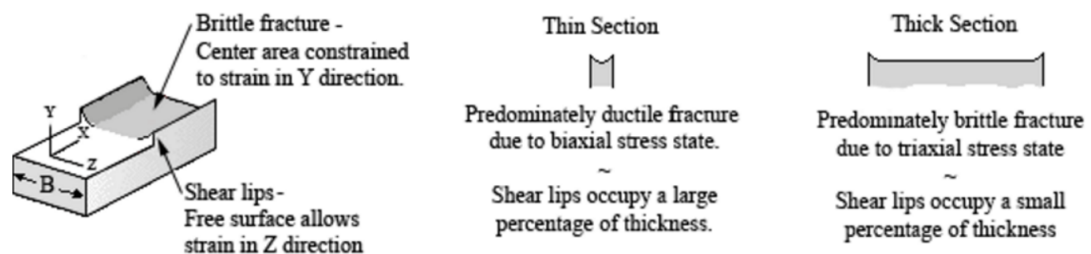


Figure 2.3: Differences in plane stress (thin section) and plane strain (thick section) due to the crack-front constraint. This alters the size of the plastic zone, giving rise to non-linear phenomena. Reproduced from [5].

2.3 Linear Elastic Fracture Mechanics

The present study focuses on purely brittle fracture. The conditions for brittle fracture can be encountered not only in linear elastic materials, but also ductile materials at low temperatures or high strain rates, or materials embrittled by fatigue. Brittle fracture is a low energy process compared to ductile or quasi-brittle fracture, since it does not involve non-linear energy dissipation phenomena like crazing, shearing and so forth.

Brittle fracture does not reveal any visible signs prior to propagation and once the crack begins to grow it advances rapidly, which can lead to catastrophic consequences. Thus, the study of brittle fracture, while considered simple, is arguably the most important for engineering materials. The domain investigating this type of failure is Linear Elastic Fracture Mechanics (LEFM).

2.3.1 K-dominance

Small Scale Yielding (SSY) is a central concept of LEFM. Based on the assumption of SSY, the fracture process zone exhibited in brittle materials is very small, implying that any non-linear phenomena are negligible [6]. In turn, it is assumed that there exists a relatively large zone, the K-dominant zone (Figure 2.4), inside which it is considered that the near-tip stress field can be accurately described by employing a

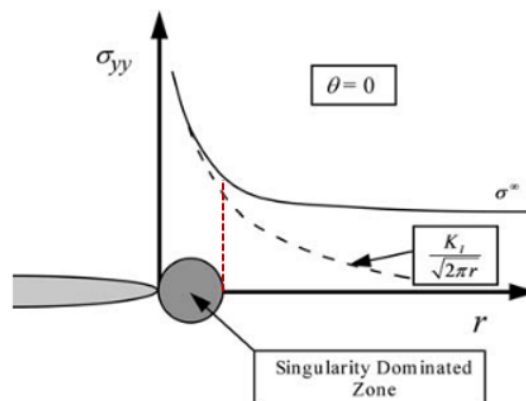


Figure 2.4: Illustration of K-dominant zone. The symbols r and θ refer to a polar coordinate system, with its origin at the crack tip. The black, solid line on the graph represents the total stress at the crack tip. The black, dashed line represents the singular term $K_I/\sqrt{2\pi r}$. Within the boundaries of the K-dominant zone (which are projected on the graph by the red, dashed line) the total stress at the crack tip can be adequately described solely by the singular term. Reproduced from [1]

single parameter, the Stress Intensity Factor (SIF).

2.3.2 Stress analysis

A number of investigators have attempted to mathematically express the stress field in the vicinity of a sharp crack, all yielding similar results [7–9]. However, this study focuses on the work of Williams [7], whose solution remains the most widely used due to its simplicity. Williams refrained from using complex variables and instead expressed the stress field as an asymptotic expansion of stress functions. His solution was the first to prove the stress singularity of $1/\sqrt{r}$ for generalised in plane-loading of elastic materials (see Figure 2.4).

For mode I fracture, the generalised in-plane stress field is given in a polar coordinate system (r, θ) as:

$$\begin{aligned} \begin{bmatrix} \sigma_{rr} \\ \sigma_{\theta\theta} \\ \tau_{r\theta} \end{bmatrix} &= \frac{K_I}{\sqrt{2\pi r}} \frac{1}{4} \begin{bmatrix} -\cos \frac{3\theta}{2} + 5 \cos \frac{\theta}{2} \\ \cos \frac{3\theta}{2} + 3 \cos \frac{\theta}{2} \\ \sin \frac{\theta}{2} + \sin \frac{3\theta}{2} \end{bmatrix} + 4A_0 \begin{bmatrix} \cos^2 \theta \\ \sin^2 \theta \\ -\sin \theta \cos \theta \end{bmatrix} \\ &+ \frac{3A_{1/2}r^{1/2}}{4} \begin{bmatrix} -\cos \frac{3\theta}{2} + 5 \cos \frac{\theta}{2} \\ \cos \frac{3\theta}{2} + 3 \cos \frac{\theta}{2} \\ \sin \frac{\theta}{2} + \sin \frac{3\theta}{2} \end{bmatrix} + \begin{matrix} \textit{Higher} \\ \textit{Order} \\ \textit{Terms} \end{matrix} \end{aligned} \quad (2.3)$$

The first term of Equation 2.3 is singular and is described by the SIF, K_I . The second and third terms are non-singular and are termed the T-stress (where $T = 4A_0$) and the $A_{1/2}$ -stress respectively. These terms depend on the geometry and finite boundaries near the crack tip. Further higher order terms are not considered in this study.

On approaching the crack tip ($r=0$), the first term tends to infinity while the higher order terms remain constant or tend to zero. Thus, there exists a region in which the fracture process is governed almost exclusively by the singular stress and is identified as the K-dominant zone. In LEFM it is a fundamental assumption that this singularity dominated zone is sufficiently large to imply that the SIF alone fully describes the stress field around the crack tip.

It must be noted that even in cases where LEFM is generally assumed to apply, as the length of the crack decreases (or, equivalently, the size of the specimen decreases) and it becomes comparable to the size of the fracture process zone, the fracture event may no longer be accurately described solely by the singular component of the stress. Even though this can be more easily seen in quasi-brittle materials [10, 11], it has also

been found, using Molecular Dynamics, for perfectly brittle materials (NaCl crystals) in cases where the crack is reduced to only a few Å[12].

2.4 Fracture of porous and cellular materials

Porous and cellular materials are materials that consist of a solid phase which contains a network of either isolated (closed-cell) or inter-connected (open-cell) pores. Materials that have porosities larger than 70% are usually termed as cellular materials or foams (Figure 2.5, bottom row), while materials of lower porosity are termed as porous materials (Figure 2.5, top row) [13].

Porous and cellular materials offer a plethora of useful attributes including unique specific properties, low density and high thermal and acoustic insulation. These properties make them attractive to various applications within the automotive, aerospace, aeronautical and ship building industries [13, 16], where they are mainly utilised as cores of composite sandwich structures.

In the fields of geoscience and geoengineering, the understanding of underground stress fields around single fractures and fracture networks in porous media are of utmost importance for the investigation of ways to achieve more efficient geothermal energy harvesting, water resource conservation, CO₂ sequestration, and ensuring safe resource exploitation in the oil and gas industry amongst other matters [17, 18].

Porosity, though, may also be introduced in materials due to their manufacturing

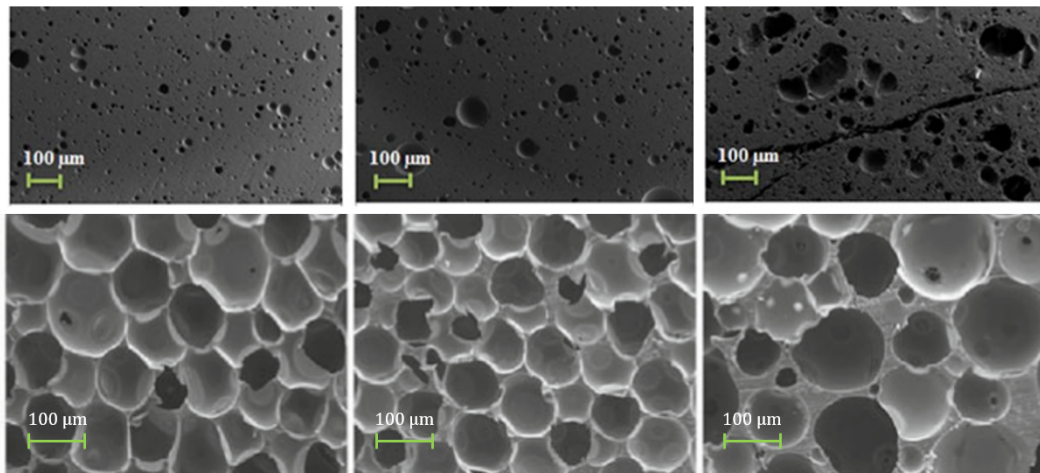


Figure 2.5: Scanning Electron Microscopy (SEM) pictures of materials with different porosities. Top row: Low and medium porosity materials manufactured by sintering (reproduced from [14]), bottom row: High porosity foams (reproduced from [15])

method (Figure 2.5, top row), and thus be unwanted and unaccounted for. Voids act as stress concentration points in a material, rendering themselves as origins for cracks. Thus this type of porosity, especially if it is not later identified, can cause catastrophic failures [19–22]. In recent years, a plethora of research studies focused on identifying, quantifying and attempting to account for this porosity have emerged [23–28].

The stiffness and strength of porous and cellular materials is a proportional function of the material’s porosity [13, 29]. In fact, in the presence of a propagating crack, the general tendency of porous materials’ behaviour can be distinguished in three categories, depending on their amount of porosity [30]. Materials with porosity less than 10% have been found to behave more like a solid material than a porous one, with only a few isolated pores whose interaction with the crack is often negligible. Thus, the behaviour of these materials is mainly governed by the behaviour of their solid phase. The second category refers to materials with a porosity ranging from 10% to 70% (the threshold above which the material is considered a foam). To the author’s knowledge, there currently exists no comprehensive study on the fracture behaviour of such materials, possibly due to the lack of natural materials with a porosity level of that range. However, there does exist a limited number of studies investigating the crack arresting capabilities of medium porosity materials (for example [31–34], see also Section 2.4.1).

The final category, materials with porosities higher than 70% (foams), behave quite differently, with the crack propagating by the failure of thin struts comprising the solid phase. Rigid polymer foams usually fail by brittle or quasi-brittle fracture, with the rapid propagation of a single crack, and their behaviour can be adequately described with LEFM. On the other hand, semi-rigid and flexible polymer foams fail by tearing, while metallic foams have been most commonly reported to fail in an elasto-plastic manner [35].

In contrast to low and medium porosity materials, there is a much larger number of studies on the fracture properties of foams and their sensitivity to intrinsic and external factors. Mass density is the most cited parameter influencing the fracture toughness of foams, with a generally monotonic increase of the latter as the former increases too. This has been demonstrated both experimentally [36–39] and numerically [40–42]. These findings only extend the effect of porosity to materials of higher values though, since porosity and density are directly correlated.

Though density and porosity are two important parameters, the brittle or ductile damage and failure of struts, was numerically found to be governed by the choice of material [40]. Even for the same material though, experiments on polymer foams showed that higher levels of cross-linking were linked to higher fracture toughness values. It was suggested that this may be attributed to the fact that lesser cross-linking was

translated to smaller cell sizes which then led to lower length-to-thickness slenderness ratios, making the material more prone to buckling [39]. However, the effect of the cell size on the material's toughness in a different set of experiments was inconclusive [37], while numerical findings linked it to a change on the material's internal length scale [40].

In foams of ultrahigh porosity, the topology of the cellular structure can have a tremendous impact on the material's behaviour, deciding whether its behaviour will be bending or stretching dominated. Such materials can be modelled with different lattices (e.g. kagome, square, etc. (Figure 2.6)), which offer different advantages and disadvantages, and their selection should be carefully considered. For example, while the kagome lattice has been reported to be capable of higher fracture toughness values [43, 44], it is also more sensitive to imperfections [45]. In fact, in a study comparing the fracture toughness of perfect hexagonal lattice with a random Voronoi lattice, it was found that the lack of periodicity decreased the fracture toughness up to 25%. A few analytical models predicting the fracture toughness of ultrahigh porosity materials have been formulated, taking into account the material's porosity value and unit cell dimensions [46–48]. These micromechanical models, however, only look at open-cell foams of idealised structure and are not applicable on varying geometries. Thus, these analytical models may provide a baseline for comparison with experimental or numerical analyses but are not usually seen as a standalone analytical tool. The investigation of the properties of lattice materials is out of the scope of this thesis, however, for more information the reader can refer to [49] and [50].

Apart from the material's intrinsic geometrical features, the experimental loading conditions also seem to affect the measured fracture toughness. More specifically, different loading configurations (three point bending versus four point bending) have been found to produce different fracture toughness values [37], and the effect of loading rate, while significant, produces inconclusive results on its correlation with the measured fracture toughness [38, 39]. Finally, a prominent size effect has also been observed [38,

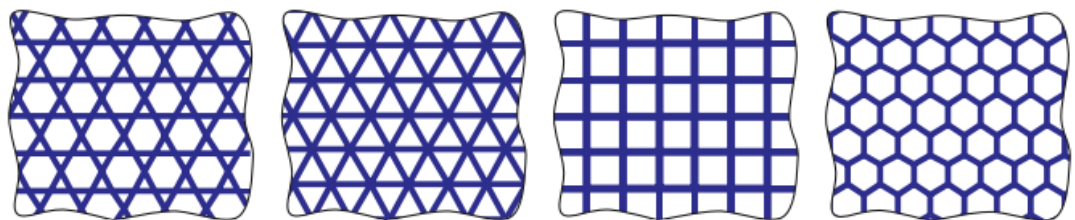


Figure 2.6: Different types of lattices. From left to right: kagome, triangular, square and hexagonal. Reproduced from [43].

39, 42] even for homothetic specimens, with smaller specimens exhibiting larger toughness values than their larger counterparts (this is more extensively covered in Section 2.5). These findings point to the significance of a standardised test procedure for cellular materials, which however, has not yet been established (see Chapter 3).

2.4.1 Interaction of crack with near-tip heterogeneities

During fracture, the behaviour of cracks is influenced by the presence of heterogeneities in the near-tip area. Since fracture is a local phenomenon, a large number of studies have focused on the interactions of a crack with a single near-tip void or cluster of voids. Here, literature on the interactions between both, pores and inclusions, is briefly cited, since they both affect the near-tip stress field by a sharp change of modulus and continuity.

Voids and inclusions in the vicinity of a crack have been found to alter the local stress field and change the measured stress intensity at the crack tip. Previous studies have found that the presence of a void or an inclusion can either amplify or lower the stress at the crack tip, depending on their relative angle [51–58]. In fact, the existence of a void has an opposing effect to the existence of an inclusion, with the former amplifying the stresses when the latter one is lowering them and vice versa. Nonetheless, it has become clear that the effect of the heterogeneity on the crack-tip stress field gradually wears off as their relative distance grows. These fluctuations of the material’s fracture toughness have been linked in previous studies to the loss of K-dominance [59] and the increased influence of the T-stresses [60], caused by the presence of the inhomogeneity. When additional voids are considered around the crack tip, the stress fluctuations become more pronounced, especially as the distance between the voids becomes smaller [53, 54, 61, 62].

One prominent study [51] derives an equation based on Eshelby’s inhomogeneity theory [63, 64] (that states that a stressed inhomogeneity in an otherwise homogeneous material can be considered a continuous part of the material with a transformation strain), which is then used to predict the fracture toughness of a material with a single void or inclusion in the vicinity of the crack tip. When compared to Finite Element Analysis (FEA) results for the aforementioned cases, the equation seems to predict the crack’s behaviour very well.

During crack growth, the presence of voids can change the direction of the crack, attracting it and drawing it in [65–70]. The attraction of cracks, is widely exploited as a inherent crack-arrest mechanism of materials. One area of application is for the self-assembly of nanowires and nanochannels on brittle thin films through controlled crack arrest [70, 71]. To achieve this, specifically designed void patterns of “arrestors” and

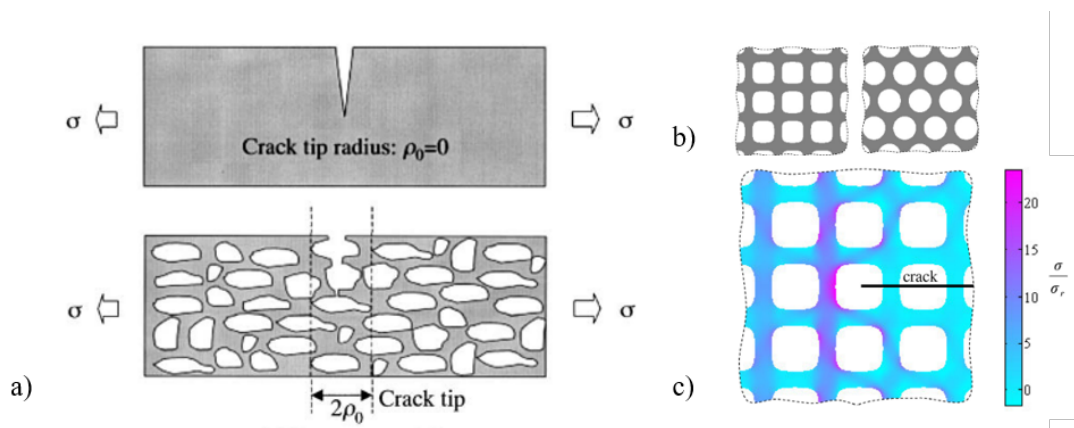


Figure 2.7: Crack arresting geometries. (a) Demonstration of the crack tip blunting of porous materials in contrast to solid ones. Reproduced from [34]. (b) Optimised crack arresting geometries for materials with four-fold and six-fold symmetry. (c) FE analysis showing the diffused stress distribution during a Mode I loading of the material with optimal four-fold symmetry. Reproduced from [74]

“initiators” are used to manipulate the crack path to a desired geometry.

Another example is the use of voids to stop expanding cracks in ceramics by taking advantage of the crack blunting effect [34]. When a crack enters a void, the periphery of the void, which has a larger radius than the crack tip, acts as the new crack tip (Figure 2.7(a),(c)). This increases the stress required to propagate the crack further and makes the material less susceptible to sudden, complete failure. Sometimes, when a crack is detected on a material, holes are drilled near the crack tip, termed as stop holes, to stop the crack from advancing further [58, 72, 73]

In materials of infinite dimensions, with a single stop-hole it has been found that the larger the size of the void, the higher the energy required to propagate the crack [62, 75]. However, when additional voids are present near the initial void (as would be in a porous material), this dependency is no longer monotonic [31, 33, 62]. This is a result of two competing effects on the stress in front of the crack tip. On the one hand, as the pore diameter increases, the crack blunting effect becomes more efficient, strengthening the material. On the other hand, as the ligament between the neighbouring voids becomes smaller, the stress level becomes larger, weakening the material.

Apart from void size though, void shape can also significantly change the stress field at the crack tip, either weakening or strengthening it. It has been shown that for a material with fourfold symmetry (square arrangement of voids, Figure 2.7(b),left), the optimal void shape resembles a square with rounded corners, while for a material with six-fold symmetry (hexagonal pattern, Figure 2.7(b),right), the optimal void shape was

circular. However, between the two, a hexagonal pattern with circular voids exhibited somewhat higher fracture toughness [74].

2.5 Size effects in fracture mechanics

Scaling is one of the most central parts of the understanding and application of any physical theory. The extrapolation of a material's stiffness and strength from a small specimen, suitable for laboratory testing, to a large, real-life structure does not always follow a predictable path [39, 76–82].

The earliest reports of a size effect were made by Leonardo Da Vinci [83], who noticed a size effect while testing the strength of metal wires of different lengths. Even though he was the first to report that smaller metal wires appear tougher than larger ones, several decades later, Galileo [84] made similar observations for bones of differently sized animals. Almost 50 years later (1686), Mariotte [85], after conducting experiments on various materials, claimed that different sizes of specimens of the same material will break at the same strength, unless there is a flaw in the material. Larger specimens are more likely to include flaws, thus they are most likely to break sooner than the smaller specimens. This observation was the stepping stone for the statistical size effect law.

In the next centuries, size effects were considered to be dependent on the stochastic distribution of material strength and were mainly studied by statisticians. In 1939, Weibull published a power law with a threshold for the material's yield strength, known as Weibull's distribution [87]. This distribution deviates from the LEFM scaling and was better suited to predict the scaling of specimens with randomly distributed flaws in them (Figure 2.8(a)).

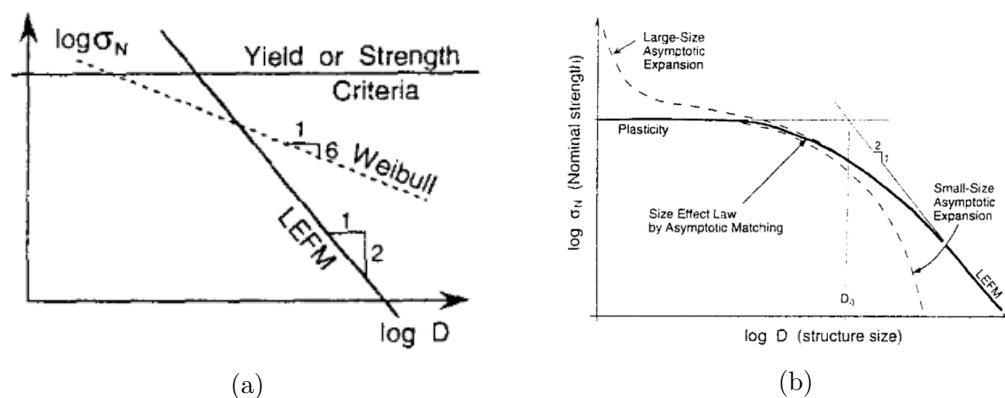


Figure 2.8: Size effect transition laws: (a) Weibull distribution and (b) Bazant's SEL. The scaling predicted by LEFM is depicted on both graphs to highlight the deviations predicted by the size effect laws for smaller specimens. Reproduced from [86].

It wasn't until 1969 that Leicester published the first deterministic study of size effects [88]. During his research, he had observed that a specimen's strength is not only dependent on this stochastic distribution of cracks and flaws, but also depends on the heterogeneous nature of the specimens. His research showed that a detrimental component of a specimen's behaviour in fracture is largely affected by the local, near-tip region.

Since approximately the 1980s, researchers studying size effects have focused their studies on the deformation mechanisms and characteristics of this near-tip region. Quasi-brittle materials, are characterised by a large FPZ and often exhibit size effects. A number of size effect laws and criteria have emerged that attempt to describe how the FPZ alters the near-tip behaviour of an otherwise linear elastic material [89–92].

Perhaps the most popular is the Size Effect Law (SEL), formulated by Bazant [10, 86, 93]. Quasi-brittle materials have a characteristic length, which is linked to their microstructural characteristics. For example, in concrete (which was the material under study) the characteristic length is equal to the size of the aggregate, while in polymer foams it is the size of a unit cell [94]. Bazant demonstrated that for smaller specimens, where the size of the specimen becomes comparable to the size of this characteristic length, the specimen transitions to plasticity. This behaviour was attributed to the localization of strain-softening damage into bands and the subsequent stress redistribution in the material. On the other hand, larger specimens are found to comply with LEFM, thus producing a transitional area of scaling for intermediate specimen sizes (Figure 2.8(b)).

A number of experiments have demonstrated the validity of the SEL, by comparing the fracture toughness of homothetic specimens (Figure 2.9). Although the SEL was

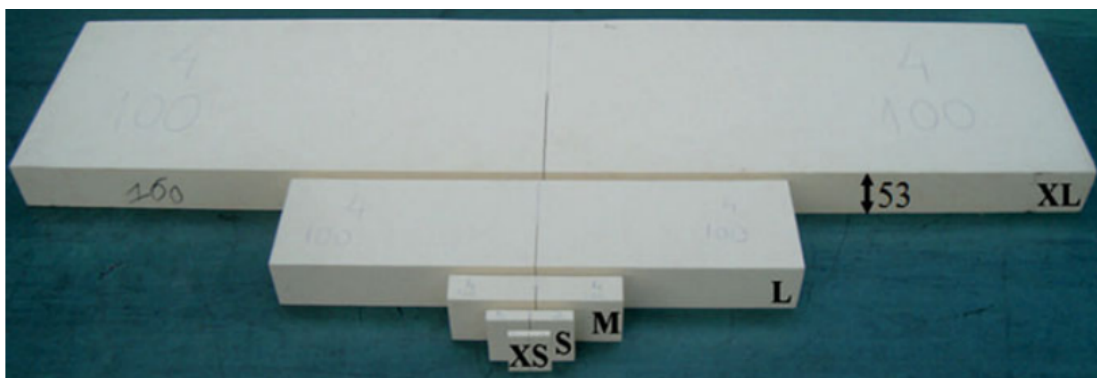


Figure 2.9: Scaled, homothetic specimens of foam used to demonstrate the size effect. Reproduced from [15].

derived by observations in concrete, it has been applied in a plethora of other quasi-brittle materials as well, including rocks, sea ice, ceramics [95] polymer foams [11, 39, 96, 97] and composites [98, 99].

2.5.1 Models accounting for non-singular stresses

Most criteria that attempt to explain size effects, consider that there exists a physical parameter, inherent to the material, that is independent of the specimen's size. For example, in the SEL described above, it is assumed that there exists a crack band whose width remains constant for all different specimen sizes of a specific material. However, a prominent set of theories has emerged, which accounts for size effects in quasi-brittle materials, like concrete and limestone, while considering the variation of FPZ with specimen size [100]. In order to explain discrepancies emanating from differently sized specimens, investigators are rejecting the notion of an indisputably large K-dominant zone and are investigating two parameter models, including non-singular terms of the Williams expansion series in addition to the SIF, to more accurately and consistently predict the fracture toughness of different specimens [101–105].

Two-parameter models that include the second, constant, non-singular term of the William's equation (Equation 2.3), the T-stress, are the most widely investigated [100, 105–110]. The T-stress by definition is only observed at the crack tip in the transverse, x-direction (parallel to the crack) and is not directly relevant to the opening stresses of mode I (in the y-direction). Yet, a number of researchers have correlated the fluctuations of the T-stress component with changes in the crack tip constraint and have reported that non-zero values of the T-stress are accompanied by a larger plastic zone (or FPZ) size. Models taking into account both the SIF and the T-stress have been formulated to predict with higher accuracy the behaviour of cracks in quasi-brittle materials. Apart from size effects, the influence of T-stresses on the crack path has been extensively investigated (for a more thorough review of investigations around T-stresses the author recommends [111]).

Some studies on the mode I behaviour of brittle materials have alternatively included the third term of the William's equation, $A_{1/2}$, which is also non-singular. In contrast to the T-stress, this term exists in all directions on the crack tip and is directly additive on the opening stress, according to Equation 2.3. The benefit of this approach is that it facilitates focus on brittle materials, by overriding the influence of the T-stress on the FPZ size, since it is assumed that such a zone no longer exists. Instead, these studies focused on the effect of the specimen's geometry and boundary conditions on the size of the K-dominant zone. They claimed that instead of a growing plastic zone which engulfs the K-dominant zone, deviations from LEFM are attributed

to the shrinking K-dominant zone which limits the universality of a single-parameter criterion to accurately describe the near-tip stress field. The accuracy of their solution was demonstrated in both, homogeneous specimens of varying geometries [103, 112] and heterogeneous materials, and more specifically composites [113].

The importance of the higher order terms in the estimation of stresses in brittle materials can also be visually identified by observing the near-tip stress field by means of photoelasticity (Figure 2.10) [114–118]. For homogeneous specimens, the photoelastic fringe pattern under mode I loading follows a concentric ellipsoidal pattern, originating at the crack tip. This fringe pattern can then be numerically reconstructed and compared with the experimentally obtained images in order to identify the number of terms needed to accurately numerically approximate the experimental results. In all studies, the inclusion of non-singular terms in the reconstruction of the near-tip field increased the accuracy of the estimations, while often multiple additional terms were needed to precisely capture the experimental results.

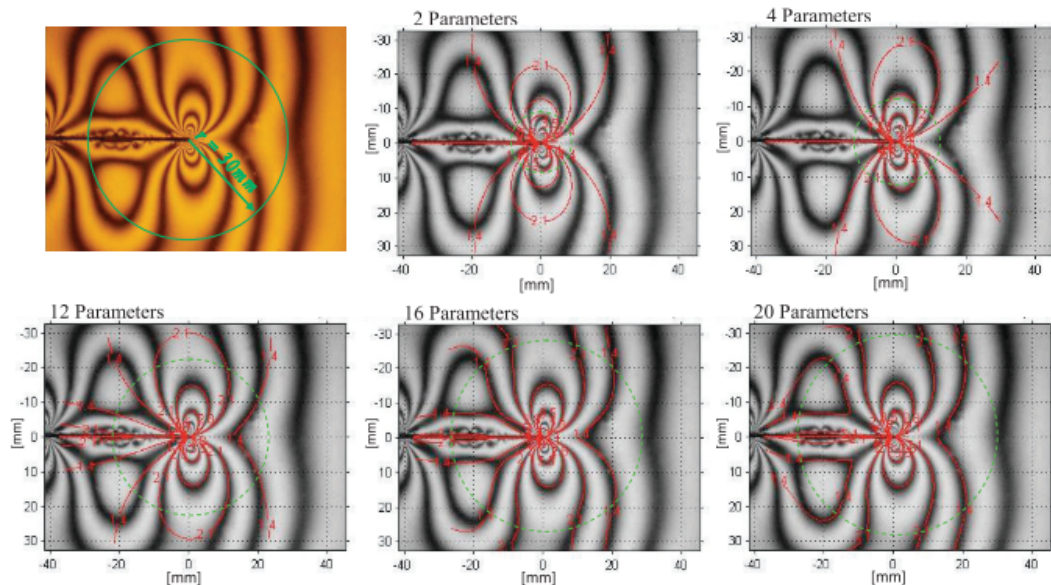


Figure 2.10: Photoelastic fringes observed in a homogeneous center-cracked compressed disk. The analytical estimation of the fringe pattern with a different number of higher order terms is superposed on the pictures in red. Reproduced from [117].

2.6 Concluding remarks

This chapter briefly describes the state of the art in considering fracture of porous materials. Literature suggests that understanding the properties of such materials is

highly significant, especially as they find increased applications throughout the engineering spectrum. This can be validated by the increasing number of publications on that subject in the most recent years. The chapter then focuses on the investigation of the effect of specimen size on a material's stress intensity factor. This size effect is found to be a detrimental factor in the behaviour and understanding of porous materials.

Following this review, the main focus of this study was turned on low to medium porosity materials, since there is only a limited amount of studies addressing their behaviour. More specifically, attention focused on the size effect exhibited for homothetic heterogeneous specimens and attempted to investigate the underlying causes of this size effect. To this end, it was decided to work with two parameter models, taking into account the second non-singular term of the William's expansion, since it has been shown to be successfully applied to brittle materials.

This work is potentially of high academic value due to its significant contribution to the understanding of the behaviour of a currently emerging set of materials. Apart from the creation of a large database of numerical and experimental results, this study further attempts to investigate in detail the physical phenomena that govern the observed behaviour. At the same time, it is believed that the findings of this study set the groundwork for designed materials with tailored fracture properties, that could be of great industrial potential.

CHAPTER 3

Experimental and numerical methods for the evaluation of the stress intensity at the crack tip

This study aims to investigate the behaviour of low to medium porosity materials in the presence of a crack and investigate the underlying cause of any observed size effects. It is important to clarify the specifics of this work, around which decisions on the methods to be used were made:

- **Critical values are not to be studied.** This study focuses on the linear progression to fracture for a constant applied moment and investigates how the stresses are distributed in the near-tip area for specimens of different mesostructures and sizes. Crack propagation is not reached.
- **Specific values of stress intensities are not the subject of study.** Our goal is that the results are transferable to any brittle material, regardless of its properties. All properties presented are normalised to the respective homogeneous values, thus making the specific material properties and applied loads of lesser importance.

To achieve the research objectives, an extensive numerical evaluation of the fracture behaviour of brittle porous materials in mode I fracture, followed by an experimental validation were conducted. Both of these processes present challenges for different reasons: Numerical modelling of porous materials is quite computationally expensive, while there is currently no standardised testing method for the Mode I fracture experiments of porous specimens.

This chapter is divided in two parts; one addressing the experimental challenges and the approach followed, and one part for the respective numerical part.

3.1 Experimental approach

Material testing standards provide engineers with a universal way to test materials, aiming to improve the confidence and comparability of materials' properties. However, due to this globalisation, testing standards sometimes fail to account for the specificities of each study, especially when it comes to innovative concepts often pursued in research.

It is interesting to note that until today there is no specific standard for the investigation of the fracture properties of porous materials. Most studies that address this issue are based on ASTM D5045 ("Standard Test Methods for Plane-Strain Fracture Toughness and Strain Energy Release Rate of Plastic Materials") [11, 15, 36, 38, 39, 103]. However, this standard refers to non-porous polymers and is only adapted by researchers to fit their needs.

Some testing standards, that could be relevant to the fracture of porous and cellular polymer materials have been identified and are listed below:

1. ASTM D5045: "Standard Test Method for Plane-Strain Fracture Toughness and Strain Energy Release Rate of Plastic Materials"
2. ASTM D5528: "Standard test method for Mode I interlaminar fracture toughness of unidirectional fibre-reinforced polymer matrix composites"
3. ASTM D3574: "Standard test methods for flexible cellular materials-slab, bonded, and molded urethane foams"
4. ASTM D3575: "Standard test methods for flexible cellular materials made from olefin polymers"
5. BS EN ISO 8067-89: "Flexible cellular polymeric materials - Determination of tear strength"

The goals of the present study cannot be adequately met with any single one of the aforementioned standards. Thus, a compilation of the ASTM D5045 and ASTM D5528 standards has been attempted, as described in the following subsections.

3.1.1 Specimen design

Testing standard D5045 requires the use of either Compact Tension (CT) or Single-End-Notch Bending (SENB) specimens. In this study, the linear elastic progression

towards fracture is studied, rather than the fracture toughness value which is usually the value of interest. Thus, precise measurements are required during the specimens' loading. Double Cantilever Beam (DCB) specimens were preferred, since these can achieve larger displacements at the loaded end for smaller applied loads. The material selected was poly(methyl methacrylate) (PMMA), as it is both brittle and transparent, allowing for the visualisation of the near-tip stress field using photoelasticity. Cast PMMA was preferred over extruded sheets to ensure a greater degree of isotropy in the specimens' behaviour.

A number of previous studies have also used DCB specimens to study the fracture behaviour of non-composite materials [94, 119–121]. Here, special notice will be given to the studies of Kumar et al. [103] and Chao et al. [104] who, similarly to this study, used PMMA DCB specimens to investigate size effects and the effect of non-singular stresses in mode I fracture. However, in both cases, homogeneous materials were studied.

The specimen design and testing outlined below is mainly based on ASTM D5528 (that uses DCB specimens), while ASTM D5045 was consulted for insights on polymer material testing specifics.

The design of the specimen is based on the following criteria:

- **ASTM D5045, (7.1.1):** *The crack length α for CT and SENB specimen should be selected such that $0.45 < \alpha/W < 0.55$, where W is the specimen length (see Figure 3.1).*

ASTM D5528, (8.4.1): *Specimens shall be at least 125mm long [...] with an initial delamination length of 50mm (i.e. $\alpha/W = 0.4$).*

Literature: Kumar et al. [103] used a value of 0.45 for DCB specimen, while Chao et al. [104] used a range from 0.04 to 0.7.

Current study: For all cases of this study it was selected: $\alpha/W = 0.5$.

- **ASTM D5045, (7.1.2):** *The criteria require that the specimen thickness B must be sufficient to ensure plane strain and that $(W - \alpha)$ be sufficient to avoid excessive plasticity in the ligament. If $(W - \alpha)$ is too small and non-linearity in loading occurs, then increasing the W/B ratio to a maximum of 4 is permitted for SENB specimens.*

ASTM D5528, (8.4.1): *Specimens shall be nominally from 20 to 25 mm [...] Note: Round-robin testing on narrow and wide specimens yielded similar results,*

indicating that the DCB specimen width is not a critical parameter.

Literature: Kumar et al. [103] used a PMMA sheet of 11.58 mm thickness, while Chao et al. [104] used a 5.84 mm thick sheet.

Current study: A 10 mm thickness was selected for this study.

- **ASTM D5528:** *For materials with low-flexural modulus or high interlaminar fracture toughness, it may be necessary to increase the number of plies, that is, increase the laminate thickness or decrease the delamination length to avoid large deflections of the specimen arms. The specimen width h and initial delamination length α_0 shall be designed to satisfy the following criteria:*

$$\alpha_0 \leq 0.042 \sqrt{\left(\frac{h^3 E_{11}}{G_{Ic}}\right)} \quad (3.1)$$

,and

$$h \leq 8.28 \frac{G_{Ic} \alpha_0^{2/3}}{E_{11}} \quad (3.2)$$

Current study: Although, the material is considered both thick and stiff enough to avoid large deflections, the above criteria have been met. For the calculations, the following material parameters were assumed:

$$G_{Ic} = 78.6 - 620 \text{ J/m}^2, \quad E_{11} = 1800 - 3300 \text{ MPa}.$$

- **ASTM D5528:** *The distance from the loading block pin to the center line of the top specimen arm shall be as small as possible to minimize errors as a result of the applied moment arm. These effects will be reduced significantly by choosing a distance, t (where t is the vertical distance between the midplane of the specimen's arm and the loading point), such that:*

$$t \leq h/4 + 0.01 \sqrt{\frac{0.0434 h^3 E_{11}}{G_{Ic}} + \alpha^2} \quad (3.3)$$

If this criterion cannot be met, then corrections for loading block effects should be used to reduce the data.

Current study: Since the loading blocks are deliberately designed into the specimen and are not glued on its surfaces, this criterion has been easily met. In the case that load blocks are used to introduce the load, ASTM D5528 advises to not use values of $\alpha/h < 10$, which could cause inaccuracies on the data reduction procedures. However, in this study, since the above criterion for t is met, aspect ratios of $\alpha/h = 6$ are used in order to save material. FEA predicts almost identical results for the energy release rate.

Porosity was then designed in the specimens in the form of circular pores in a rectangular array (Figure 3.1). The inter-void distances in the x and y direction are $Size_x = 3.5mm$ and $Size_y = \sqrt{3}Size_x/2$ respectively. These values were selected with the numerical model in mind, where the void topology is that of an equilateral triangular instead of a rectangle (this will be described in more detail in Chapter 4). The given relationship between the two sides of each unit cell ensures that all inter-void distances are equal for the triangular void arrangement, which translates to a quasi-isotropic material [78]. However, for the experimental study a rectangular arrangement was preferred instead, in order to simplify the specimens manufacturing (as the means of manufacturing was not yet specified). This topology difference is not expected to produce large deviations in the estimated properties under study (also see Figure 5.4).

The width of the specimen, h , and the voids' diameter, d , are variables for this study and will be further described in the respective chapter.

At least three specimens of each different specimen configuration were manufactured (see Figure 5.1b), to ensure the repeatability of the results. A set of homogeneous specimens was also manufactured and tested, as a reference value for the porous specimens. Laser-cutting was used for the manufacturing of all specimens, as described in more detail in Chapter 5.

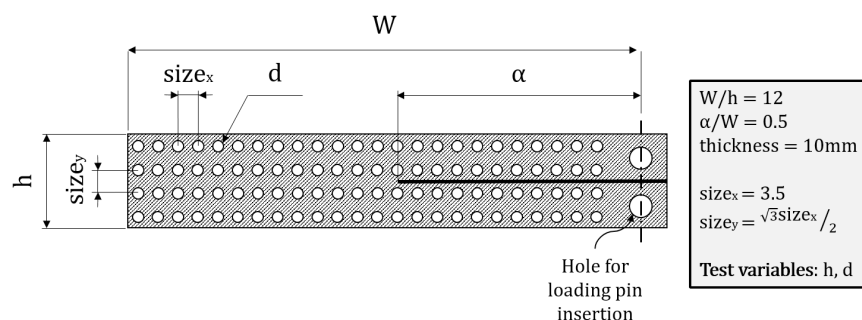


Figure 3.1: Schematic and summary of the specimen design specifications.

Quality assurance

Before testing, the manufactured specimens were subjected to a quality control procedure to ensure their geometrical consistency.

In order to assess the fidelity of the manufactured specimens to the design specifications, each specimen's surface was scanned and the image was then processed in an in-house MATLAB code to extract all values relevant to the designed void pattern (Figure 3.2). Prior to scanning the specimen's surface, the area of the specimen to be examined was painted black to increase the visibility of the voids. Note that the near-tip area was not painted, in order to maintain the ability to visualise the near-tip area by means of photoelasticity. However, it was assumed that any laser-cutting inaccuracies per specimen would be consistent throughout the entire void pattern and

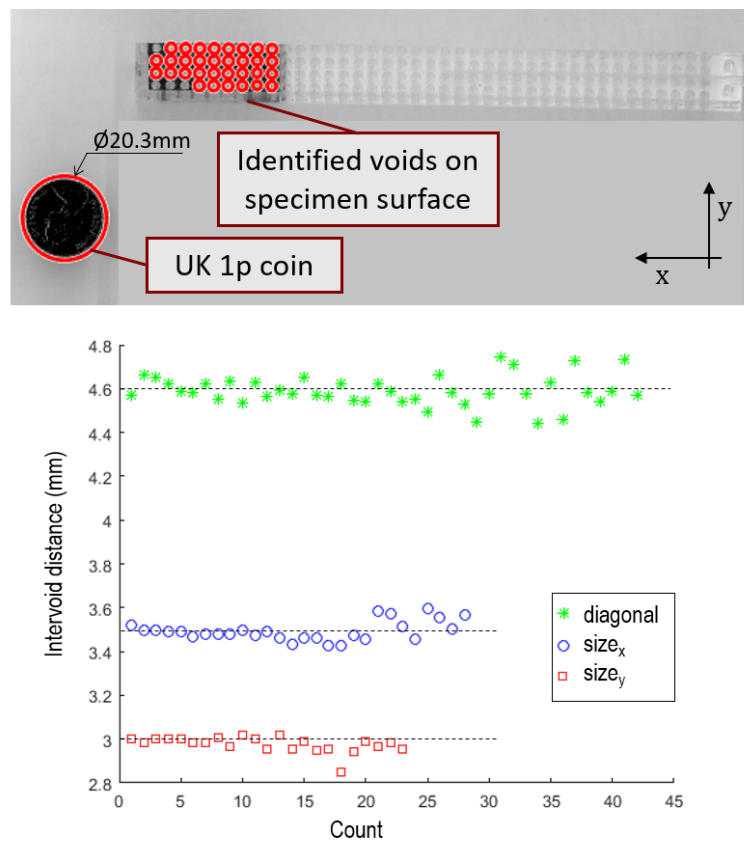


Figure 3.2: Top: MATLAB recognition of void pattern. A GB one pence coin was used in all pictures as a reference for calibration. Bottom: Graph produced by MATLAB with all inter-void distances estimated. When large deviations were shown, the specimens were also inspected both visually and with the use of a caliper.

thus even an examination of a small part of the specimen would reveal them. In each scanned image, a UK one pence coin was included, whose radius was used as a reference of length to calibrate the code’s measuring capabilities. MATLAB was then programmed to identify all circular shapes of a certain size range in the image (i.e. the voids), estimate their void radius and inter-void distances, and evaluate the circularity and eccentricity of each identified void.

A ruler and caliper were also used both to measure the external dimensions of the specimens, and to validate the MATLAB results by randomly measuring a few relevant dimensions for each set of specimens. Self-similarity between all different types of specimens was validated by means of weighing each specimen.

3.1.2 Testing procedure

Mode I test

The tests were conducted on a constant displacement rate device, as described in both testing standards considered here. In order to mount the specimens on the machine, a specifically designed clevis was manufactured (Figure 3.3), based on the specifications of ASTM D5045 (detailed drawing can be found in Appendix A). After mounting the specimens, ASTM D5528, in paragraph 11.5, states that “*the end of the specimen opposite the grips should be supported before loading*”. This was taken into account before each test was conducted (see Figure 5.2).

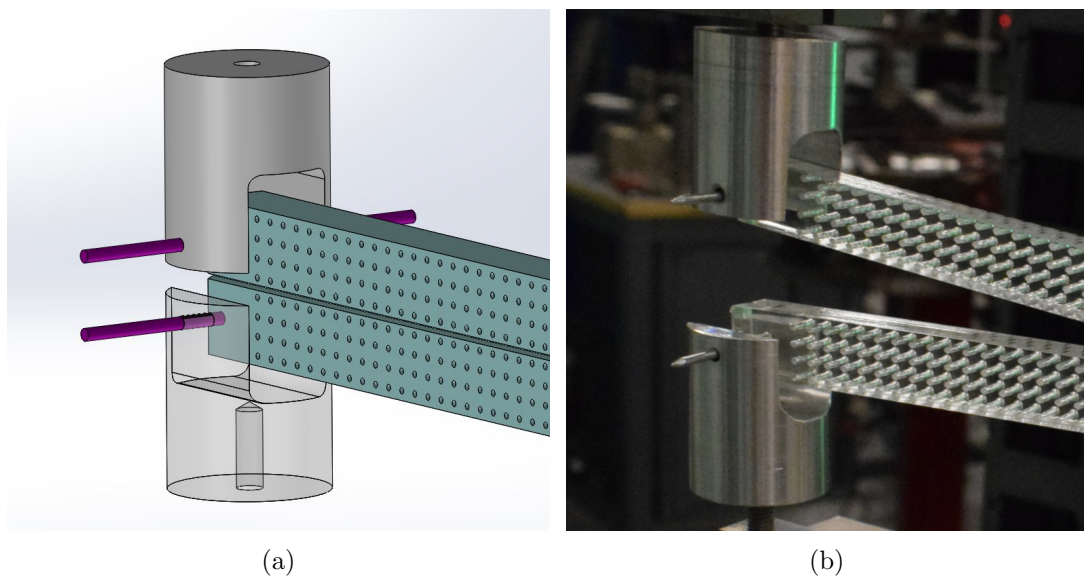


Figure 3.3: Designed (a) and manufactured (b) clevis. In (a) the transparency of the bottom clevis has been adjusted to show hidden details.

The specimens were loaded at a constant rate, as stated in both ASTM D5045 and ASTM D5528. However, the following conflicting suggestions are made in the two testing standards:

- **ASTM D5528 (11.7.1):** *Load the specimen at a constant crosshead rate between 1 and 5 mm/min.*
- **ASTM D5045 (8.3.1):** *Since plastics are viscoelastic materials [...] it is recommended that a crosshead rate of 10 mm/min be used.*

In DCB specimens, the moment at the crack tip is much higher than in CT or SENB specimens (as described in ASTM D5045). Thus, a crosshead rate of 10 mm/min is considered to be inappropriate as it will very quickly increase the stress at the crack tip and impede the capturing of the photoelastic fringe pattern by decreasing the time available to take suitable photos (see also Section 5.1.1). Since the material remains in the linear elastic region it is not expected that the loading rate will severely impact the estimated stress intensity. For consistency reasons, the highest suggested level from ASTM D5528 (i.e. 5mm/min) was selected as a compromise between the two standards, in order to avoid viscoelastic effects while maintaining a pseudo-static loading.

This study does not focus on the critical value of the fracture toughness. Instead, it focuses on the variations of the stress intensity at the crack tip for a constant value of the applied moment, for specimens of different sizes and porosity values. Consequently, the specimens were not loaded until fracture. They were loaded up to a certain value, below the critical point, and then unloaded at a constant rate. During each test, the goal was to ensure that the specimen remain in the linear elastic region.

Photoelasticity

Part of this study is to investigate the underlying reason for the observed variations in the values of the stress intensity at the crack tip for differently sized specimens in brittle porous materials, and the focus was set on the increased significance of non-singular stresses. As it was shown in Chapter 2, there exists a plethora of studies that use photoelasticity in order to experimentally visualise the stress field at the tip of a crack and identify the influence of the non-singular components on it [114–118].

Photoelasticity is based on the principal stresses observed in a loaded material. A brief, intuitive description of the principal stresses is given here for reference. The stress tensor provides detailed information on the stresses applied at a point on the material (Figure 3.4a). The component τ_{ij} is the component of the stress in the i direction, acting on a surface perpendicular to the j direction (the tensor is symmetric so $\tau_{ij} = \tau_{ji}$). The indices i and j take the values of the coordinate axes, in this case x and y . The stress

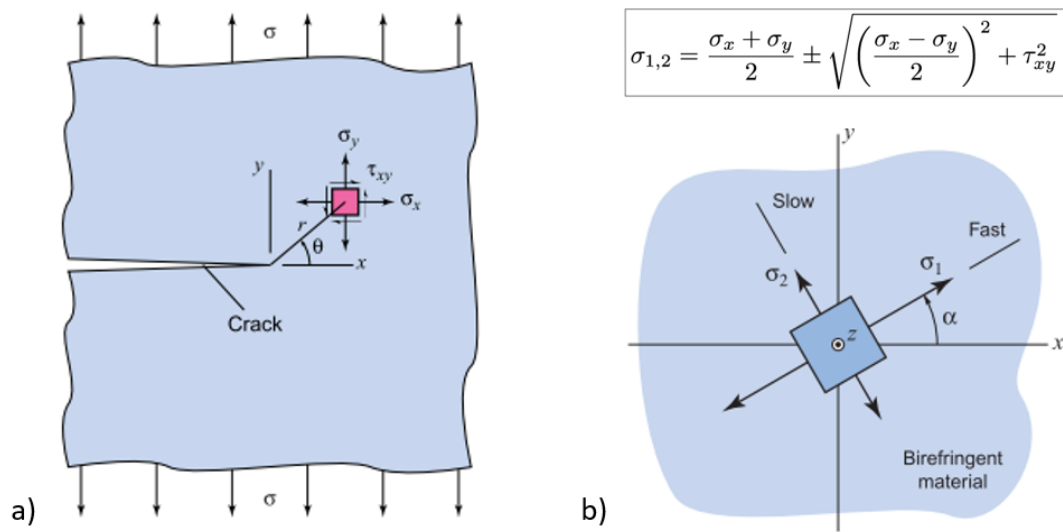


Figure 3.4: Schematic representation of (a) a general stress tensor and (b) a stress tensor diagonalised by its principal stresses (eigenvalues). Figures adapted from [122].

tensor is diagonalised (i.e. vanishing shear stresses) by its eigenvalues, which are called principal stresses (σ_1, σ_2 for the 2D plane); diagonalising the tensor corresponds to a rotation of the coordinate system, to a basis aligned with the eigenvectors of the stress tensor (Figure 3.4b).

Photoelasticity can reveal two, over-lapping patterns in the specimen: isochromatics and isoclinics. Isochromatics are the loci where the difference of the two principal stresses ($\sigma_1 - \sigma_2$) is constant. The number of these bands increases in proportion to the external forces. Isoclinics, on the other hand, are related to the direction of the principal stresses. These usually obscure a large part of the specimen and may be unwanted. In order to avoid them, circular polarisers may be used. For the experimental part of this study, during loading, the near-tip stress field was monitored with the use of a circular polariscope in order to isolate the isochromatic patterns and obtain qualitative results on the influence of porosity on the near-tip stress field.

Any light wave has an amplitude vector that is always normal to its propagating direction. In ordinary light, the direction of this amplitude vector, while remaining normal to the velocity, is completely random. In photoelasticity, wave plates and polarisers are used to manipulate the direction of the waves. Polarisers are characterised by a polarising direction. When ordinary light goes through a polariser, it is resolved in two components: one parallel to the polarising direction and one perpendicular to it. The first one is allowed to go through the polariser, while the latter one is rejected. Wave plates are similar to polarisers in that they break the incident light in

two perpendicular components. Instead of rejecting one of the two components, the wave plate imposes on them a relative phase difference, δ_{phase} .

In a circular polariscope (Figure 3.5) each element performs a certain function :

- **Light source:** In this study, both white light and green light sources were used. While white light gives a colourful spectrum, monochromatic light can highlight the details and facilitate the observation of the maxima and minima in the light intensity.
- **Polariser:** Plane polarises the ordinary light. The polariser was rotated at 45° with respect to the loading direction.
- **First quarter wave plate:** In circular polariscope, wave plates are oriented at a 45° angle to the polariser. This results in two components of equal amplitude and a phase difference of $\delta_{phase} = \lambda/4$, where λ is the wavelength of the light wave. This retardation causes the resulting vector to rotate in a circular pattern.
- **Model:** Some transparent, polymer materials, when stressed can act as temporary wave plates, resolving the incident light in two perpendicular vibration planes, which are always parallel to the directions of the principal stresses in the material. The two wave components transverse the material at different velocities, which causes a relative phase difference between them. This phenomenon is called birefringence and is the same as that observed in some crystals.
- **Second quarter wave plate:** Quarter wave plates are considered imperfect, since they are usually calibrated to produce a phase change of $\delta_{phase} = \lambda/4$ for a specific wavelength. In order to correct any inaccuracies caused by the first quarter wave plate, a second one is used, crossed to the first one (the fast and slow planes are reversed).
- **Analyser:** The analyser is essentially a second polariser, that plane polarises the incident waves coming from the second quarter wave plate. In this study, the analyser and the polariser were crossed (had a relative angle of 90°), producing a dark field (in which the unstressed specimen appears black).

Note that in this study, the polariser and quarter wave plate were merged in one optical element. Two circular polariscope, including a quarter wave plate, of dimensions 50x50x0.8mm were used, which were procured from Knight Optical.

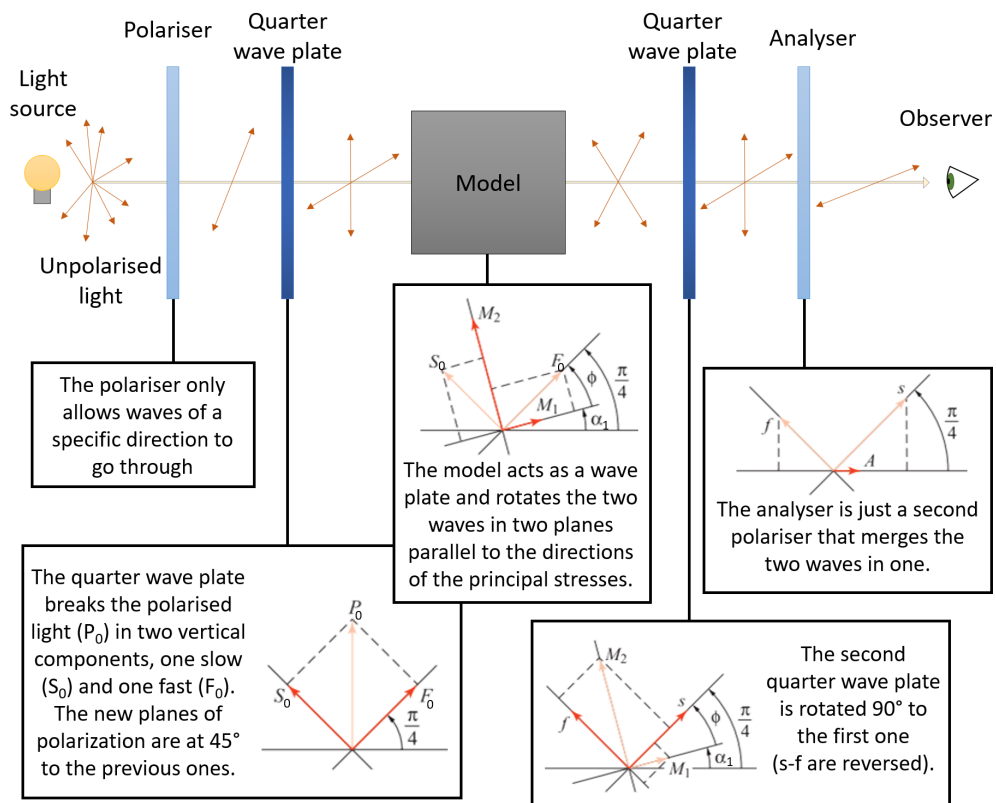


Figure 3.5: Illustration of a circular polariscope and its elements. The brown arrows represent the normal amplitude vector with respect to the wave propagation. Vector diagrams have been adapted from [122].

Results post-processing

During the mode I testing of each specimen, a load-displacement graph was generated. From the recorded data, each specimen's linear progression to fracture was evaluated and the effect of specimen size and porosity was observed.

The Beam Theory (BT) expression for the DCB specimens, which is also suggested in ASTM D5528, estimates the energy release rate G_I from a load-displacement graph as:

$$G_I = \frac{3F\delta}{2B\alpha} \quad (3.4)$$

, where F here is the load and δ is the total opening displacement between the two specimen arms.

This equation is considered valid when the specimen is perfectly “built-in”, meaning that the specimen is clamped at the delamination front and no rotation may occur beyond it. If this is not the case, several correction methods are proposed in ASTM D5528 to account for the effects caused by the crack front rotation (e.g. modified beam theory (MBT), compliance calibration (CC), etc.). However, in this study, since the specimens did not reach crack propagation, these methods are not applicable and thus, Equation 3.4 was used to estimate the energy release rate, G_I .

Since the material is assumed to remain in the linear elastic region, the stress intensity K_I was then estimated from the energy release rate G_I using Equations 2.1 and 2.2, which for plane strain become:

$$K_I = \sqrt{\frac{G_I E}{1 - \nu^2}} \quad (3.5)$$

Note that for both, porous and homogeneous specimens, the Young’s modulus, E , and Poisson ratio, ν , of the homogeneous material were used for the estimation of K_I with Equation 3.5. This means that for the estimation of the experimental results the specimens were considered as different configurations of the same, homogeneous material, and the arm’s stiffness weakening from the existence of porosity was not considered.

3.2 Numerical approach

Numerical modelling of porous materials is a computationally intensive process. Unlike homogeneous solids, the internal structure of porous materials, if discretely modelled, requires an increased level of detail. As a result, larger specimens, which contain an increased number of unit cells, are not easily modelled.

Four finite element modelling strategies are usually employed to simulate porous materials [35]:

- Homogenised specimen: The specimen is modelled as a homogeneous pseudo-material, with “smeared” properties throughout its volume. While this technique is computationally inexpensive, it does not account for local phenomena. Thus, such a model would be inappropriate for the study of fracture events.
- Periodic unit cell or agglomerate: In this technique, a single unit cell, or an agglomerate of unit cells is discretely modelled and periodic boundary conditions are assumed to fill a larger space. This technique is more suitable for the representation of infinite domains. Due to the periodic boundary conditions, these models are characterised by more idealised geometries.

- Discrete models: The entire specimen and its porous structure are modelled. The results are directly comparable to experimental results. However, due to the high complexity of the models and the increased computational cost, this technique is only used for smaller, finite specimens.
- Embedded-cell models: This is a hybrid between the discrete and homogenised models. This technique features an accurately modelled region around an area of interest (usually employed to investigate cracks), surrounded by a homogenised medium that covers the rest of the specimen's area.

This study focuses on finite size specimens. Consequently, discrete models were selected in order to approach the real-life behaviour of those materials as close as possible.

3.2.1 Finite Element model

For the numerical part of the study, two-dimensional plane strain models of DCB specimens were created using the commercial FEA software ANSYS. The models were generated through self-developed scripts written in Ansys Parametric Design Language (APDL).

Each model was created by repeatedly regenerating a rectangular unit cell with a centrally located heterogeneity (Figure 3.6d) across the length and depth of the specimen, the geometry of which can be seen in Figure 3.6a. The dimensions of the unit cell in the x and y direction are $Size_x = 3.5mm$ and $Size_y = \sqrt{3}Size_x/2$ respectively. As in the experiments, the porosity of the specimen, P , is one of the study variables and was controlled by changing the void diameter. Thus, the porosity was estimated as a function of the area (which be equivalent to the volume in a 3D model) of the porous specimen with respect to the area of a similarly sized homogeneous specimen. It must be noted that the cell density and inter-void distances remain constant in all cases. While a material's porosity can also be controlled by keeping the void diameter constant and changing the void arrangement and density, such cases have not been considered here. Again, a homogeneous model was created for reference and validation using the same mesh configuration and material properties as used for the porous models.

Each unit cell was paved with a structured mesh, using element Plane 183, an 8-node two-dimensional structural element, under plane strain configuration. The boundaries of each unit cell were meshed with equal sized elements using 14 and 16 element divisions in the horizontal, x , and vertical, y , directions respectively (right cell of Figure 3.6d). Near the crack tip, the horizontal boundaries of the immediately adjacent cells are refined $4x$ times, giving a total of 56 and 16 elements in the horizontal and vertical

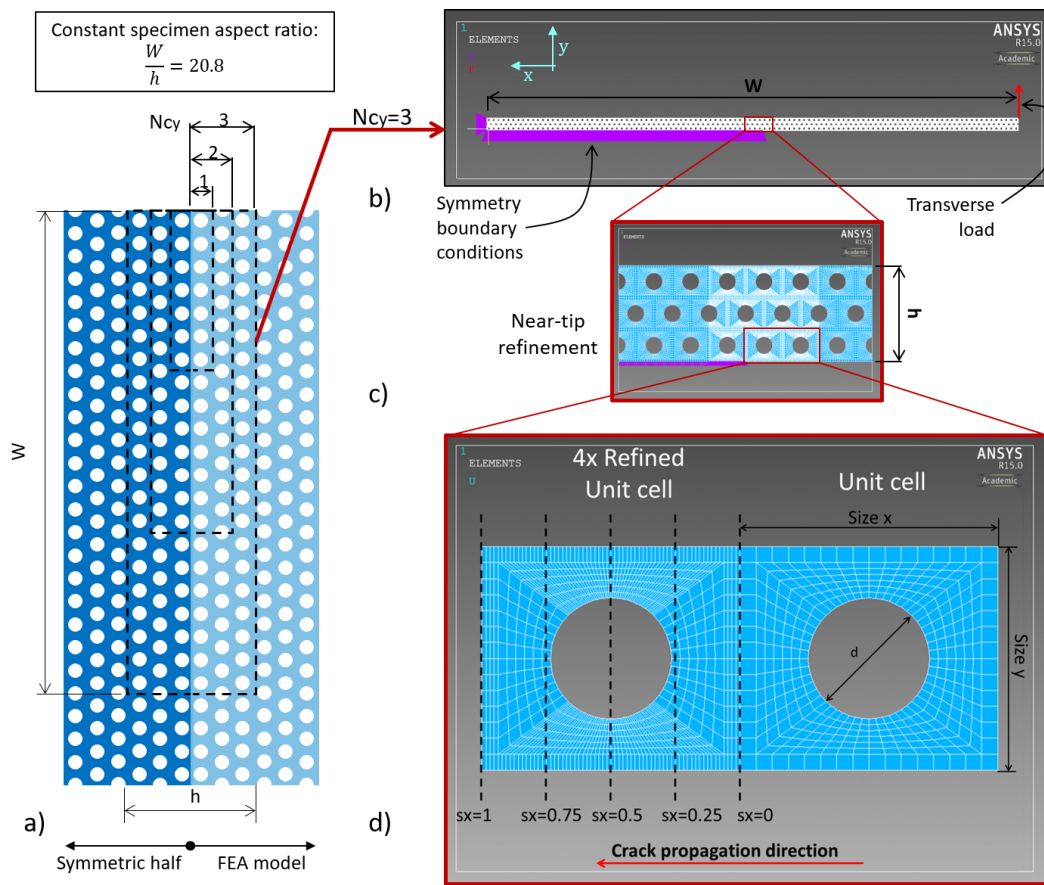


Figure 3.6: (a) Illustration of the different specimen sizes (dashed lines) cut from an infinite sheet of material, b) Boundary conditions and loading for a model with $N_{cy} = 3$, c) Near-tip refined mesh for a model with $N_{cy} = 3$, d) Refined and non-refined unit cell. The crack tip locations relative to the void sx are depicted on the image. The crack is assumed to propagate with a direction from $sx = 0$ to $sx = 1$.

direction respectively (left cell of Figure 3.6d). Five different locations relative to the nearest void have been considered for the crack tip position, starting at the edge of the unit cell ($sx = 0$) and advancing the crack tip by one quarter of its length up to the other end of the unit cell ($sx = 1$) (Figure 3.6d).

A mesh sensitivity study was conducted (Figure 3.7) to assess numerical uncertainties especially in regions where singularities appear. In order to keep the aspect ratio of the elements within acceptable limits, large changes in the refinement of the near-tip area in the horizontal direction mandated proportional changes in the refinement of the far-field mesh which controls the y-direction mesh distribution (see Figure 3.6d). Below an element size of just above 0.05mm , the solution seems to converge with minimal

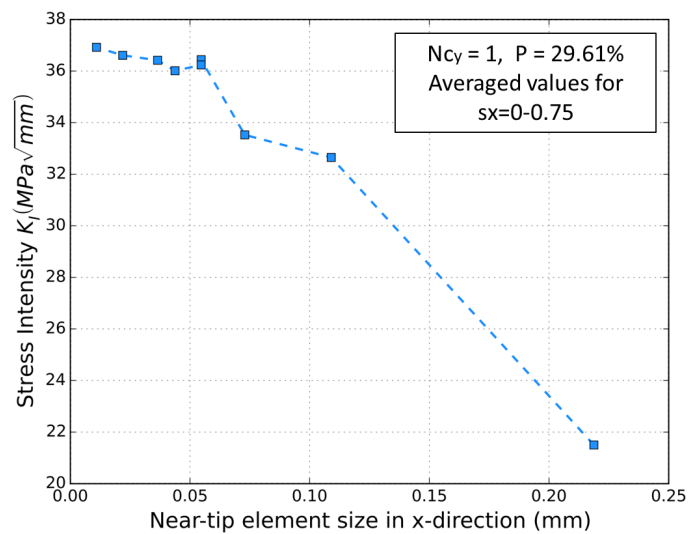


Figure 3.7: Mesh convergence study conducted on the specimens described of Chapter 4. At an element size just above 0.05mm two overlapping points are seen which represent two different levels of far-field refinement. The non-refined far-field mesh with a near-tip element size of approximately 0.05mm was selected for the simulations presented in the following chapters.

fluctuations. At this level of refinement, two models with different far-field refinements were run to examine the impact of the element's aspect ratio on the FEA solution. Both the refined and non-refined far-field mesh gave almost identical results. Thus, the non-refined far-field mesh with 0.05mm near-tip element size, as described in the previous paragraph, was selected for the simulations.

Geometrically similar models of different sizes were created for each case, by varying the rows of unit cells arranged symmetrically about the crack, which are described by the parameter N_{c_y} (Figure 3.6a). Importantly, geometrical similarity of the specimen was maintained by keeping the specimen aspect ratio constant to $W/h = 20.8$ (Figure 3.6a). In order to reduce computational expense and due to the symmetrical nature of a Mode I test only half of the model was generated (Figure 3.6b). It should be noted that due to the symmetric nature of the model, the porosity around the crack is also by definition symmetric in all of the studied topologies (Figure 3.6c). The crack length α is similarly scaled and is approximately $\alpha = 10h$, where h is the total height of the symmetric beam. This is different from the value used for the experimental case, however it complies with the suggested value of ASTM D5528.

A transverse tensile point load is applied at the free edge of the specimen (Figure 3.6b). The load is varied so that the moment at the crack tip remains constant for all different specimen sizes and crack lengths.

All models are considered different structural configurations of the same, perfectly brittle material and thus a matrix Young's modulus of $E = 3GPa$ and Poisson ratio $\nu = 0.35$ is used for all models. However, as said in the introduction the specific values used are not important, as all results will be normalised.

3.2.2 Analysis of numerical results

As seen in Section 2.3.2, the near-tip stress field of a sharp crack in a perfectly brittle material in Mode I loading can be described with William's asymptotic expansion. The equation is repeated below for convenience. Considering a polar coordinate system (r, θ) with its origin at the crack tip the stress components are given by:

$$\begin{aligned} \begin{bmatrix} \sigma_{rr} \\ \sigma_{\theta\theta} \\ \tau_{r\theta} \end{bmatrix} &= \frac{K_I}{\sqrt{2\pi r}} \frac{1}{4} \begin{bmatrix} -\cos \frac{3\theta}{2} + 5 \cos \frac{\theta}{2} \\ \cos \frac{3\theta}{2} + 3 \cos \frac{\theta}{2} \\ \sin \frac{\theta}{2} + \sin \frac{3\theta}{2} \end{bmatrix} + 4A_0 \begin{bmatrix} \cos^2 \theta \\ \sin^2 \theta \\ -\sin \theta \cos \theta \end{bmatrix} \\ &+ \frac{3A_{1/2}r^{1/2}}{4} \begin{bmatrix} -\cos \frac{3\theta}{2} + 5 \cos \frac{\theta}{2} \\ \cos \frac{3\theta}{2} + 3 \cos \frac{\theta}{2} \\ \sin \frac{\theta}{2} + \sin \frac{3\theta}{2} \end{bmatrix} + \begin{matrix} \text{Higher} \\ \text{Order} \\ \text{Terms} \end{matrix} \end{aligned} \quad (3.6)$$

In order to estimate K_I from the numerical results the projection method as presented in [123] was used and is briefly described below. Considering the y -direction normal stress distribution ($\sigma_{\theta\theta}$) ahead of the crack tip ($\theta = 0$) only, Equation 3.6 can be transformed as:

$$\sigma_{yy}(x) = \frac{K_I}{\sqrt{2\pi x}} + 3A_{1/2}\sqrt{x} \implies \sigma_{yy}(x)\sqrt{2\pi x} = K_I + (3\sqrt{2\pi}A_{1/2})x \quad (3.7)$$

where x is equivalent to r in (r, θ) when $\theta = 0$.

In Figure 3.8(a), the stress intensity variation is plotted against the distance ahead of the crack tip, normalized by the crack length for different crack tip positions in specimens comprised of four rows of unit cells and a constant porosity of 44.8%. For homogeneous materials this variation is linear with an equal gradient at all size scales. In this study, the gradient of the variation is referred to as the normalized amplitude of $A_{1/2}$ -stresses and can be quantified as $C = (3\sqrt{2\pi}A_{1/2})\alpha$. To estimate C for the porous materials investigated, only the linear part of the variation, immediately ahead of the crack tip, is considered. Due to numerical limitations in accurately calculating stresses in the vicinity of the crack tip singularity, a straight line is fitted onto the linear part of each stress variation and extrapolated back to zero radius (i.e. dotted lines in Figure 3.8(a)). At infinitesimal distances from the crack tip, non-singular terms

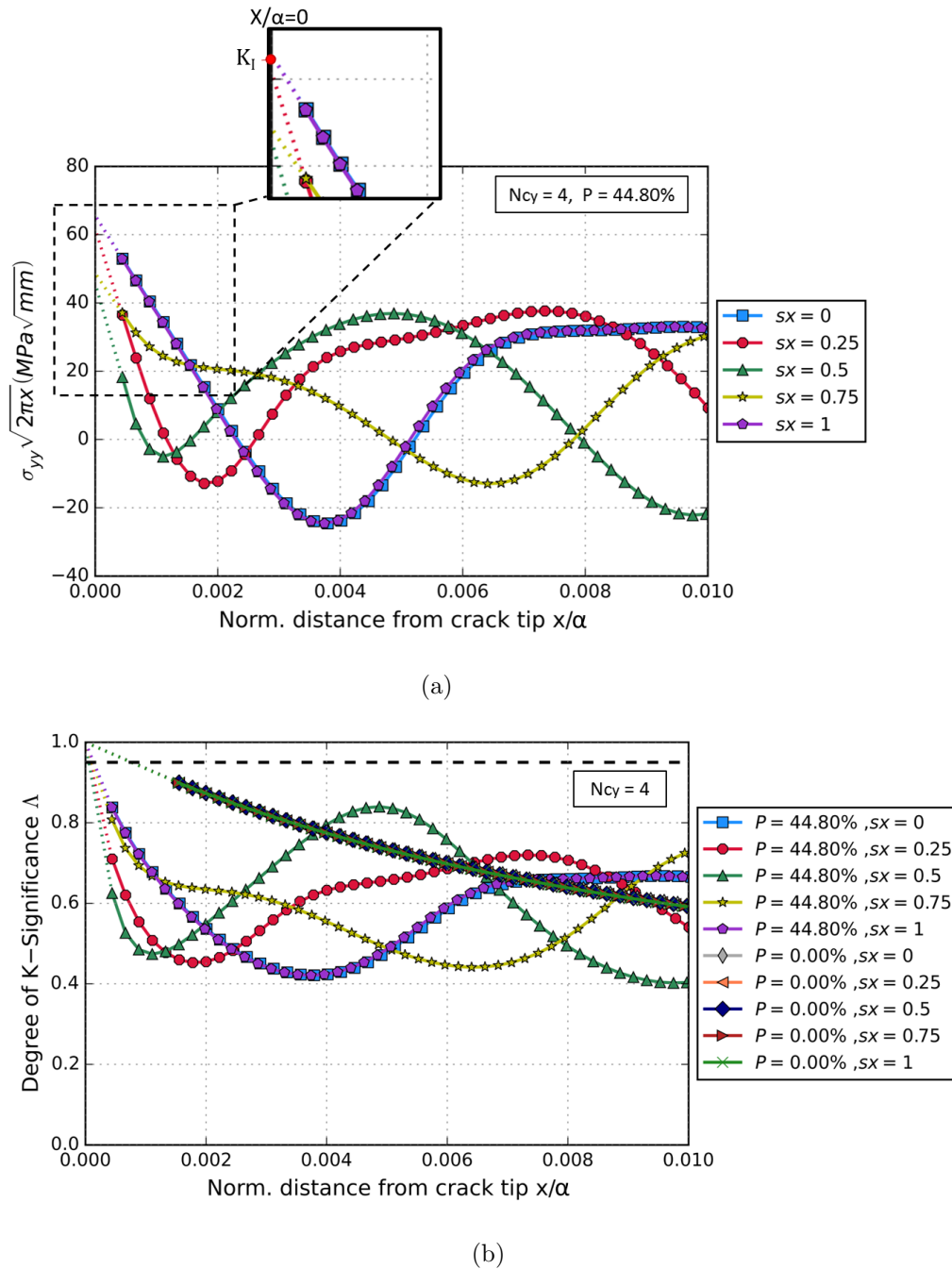


Figure 3.8: a) Projection method to estimate the magnitude of the stress intensity at the crack tip. A inset is also shown on the figure to clearly show how K_I is estimated using the projection method. b) Linear extrapolation of the degree of K-significance Δ to estimate the size of the K-dominant zone. The dashed line represents $\Delta = 95\%$. The values plotted here are taken from the models described in Chapter 4.

become negligible compared to the first term of Equation 3.7, which in turn takes the form:

$$\lim_{x \rightarrow 0} \sqrt{2\pi x} \sigma_{yy}(x) = K_I \quad (3.8)$$

Thus, the stress intensity was estimated as the value of quantity $\sqrt{2\pi x} \sigma_{yy}(x)$ for $x/\alpha = 0$ [103, 112, 113, 123], as can be seen in the inset of Figure 3.8(a). The values of the stress intensity estimated by this method are in good agreement with those estimated from ANSYS directly using the Interaction Integral Formulation, while, for the homogeneous case, the value estimated with the projection method has a closer correlation to the analytical estimation of the apparent stress intensity for DCB specimen (Table 3.1).

It can be seen in Figure 3.8(a) that the extrapolated stress at the crack tip used for the calculation of the stress intensity depends on the slope of each curve, and is therefore indirectly affected by the near-tip stress distribution. While the $A_{1/2}$ -stresses are negligible right at the crack tip, they may nonetheless be significant in the near-tip region, thereby indirectly affecting the value of the apparent stress intensity. In order to normalise the results, the K_I estimated by extrapolation for the porous materials was normalized with respect to the K_I of the homogeneous case, which is a constant value $K_I^H (MPa\sqrt{mm})$. From the definition of Equation 3.8 on x approaching zero, this normalising is equivalent to the ratio of the opening stress at the crack tip in the porous material to the opening stress at the crack tip in the homogeneous material, henceforth referred to here as the normalised stress intensity SI_N , where:

$$SI_N = \frac{K_I^P}{K_I^H} = \frac{\sigma_{yy}^P}{\sigma_{yy}^H} \quad (3.9)$$

It is important to remember that the values of stress intensity and opening stress refer to models with loading scaled in such a way that they remain constant for all specimen sizes with zero porosity. Thus, it merely reflects the magnitude of the open-

Table 3.1: Comparison of K_I values of the homogeneous case estimated analytically, using the interaction integral formulation in ANSYS and using the projection method described in [123].

	Analytical	Interaction Integral	Projection method
Apparent stress intensity $K_I (MPa\sqrt{mm})$	31.84	32.86	31.81
Discrepancy from analytical	-	3.15%	0.09%

ing stress at the crack tip for a given load and not the critical value of stress that the material could actually withstand before initiating the crack (K_{Ic}), which is not considered in this study. The K-dominant region was considered as the zone around the crack tip where K_I contributes to more than 95% of the opening stress at the crack tip (see horizontal dashed line in Figure 3.8(b)). The degree of K-dominance Λ [103, 113] is therefore estimated as:

$$\Lambda = \frac{\sigma_y^{\text{sing}}}{\sigma_y^{\text{sing}} + |\sigma_y^{\text{non-sing}}|} \quad (3.10)$$

, where the singular (σ_y^{sing}) and non-singular ($\sigma_y^{\text{non-sing}}$) components of the stress are estimated as:

$$\sigma_y^{\text{sing}}(x) = \frac{K_I}{\sqrt{2\pi x}} \quad \text{and} \quad \sigma_y^{\text{non-sing}}(x) = \sigma_{yy}(x) - \sigma_y^{\text{sing}}(x) \quad (3.11)$$

CHAPTER 4

Size effects in idealised brittle specimens of low to medium porosity

This chapter studies how the existence of porosity can affect the stress field in brittle specimens of different sizes¹. The effect of the crack-pore interaction on the stress intensity at the crack tip is observed in two levels: mesoscopically (at the level of the unit cell) and macroscopically (considering the material as a homogenised medium).

As discussed in Chapter 2, in heterogeneous materials, local discontinuities in the matrix material can influence the stress field in the vicinity of the heterogeneity, leading to the appearance of local SIFs at different locations with respect to the void [58, 60, 124]. Han and Chen [60], while studying the influence of a microvoid on the SIF of a brittle material, attributed its oscillation to the relaxation of T-stress, which occurs near the void and results in either an amplification or a shielding effect. These studies refer to individual pores in infinite media, which implies that the size of the heterogeneity is insignificant compared to the total size of the specimen.

However, when the size of the heterogeneity becomes comparable to that of the specimen, heterogeneous materials have been observed to exhibit crack tip stresses contradicting the usual size scaling predicted by LEFM. These size effects can cause severe discrepancies and unexpected fracture events if they are not taken into account. For quasi-brittle heterogeneous materials such as polymer foams [11, 38, 39, 97], composites [98, 99], and concrete [125–127], this behaviour is normally attributed to the

¹The findings of this chapter have been published and can be found online using the following citation: *D. Touliaou, M. A. Wheel, "K-dominance and size effect in mode I fracture of brittle materials with low to medium porosity", Engineering Fracture Mechanics, 2018, <https://doi.org/10.1016/j.engfracmech.2018.06.041>*

material's transition to plasticity in very small scales.

Here, the focus is shifted to perfectly brittle, low to medium porosity materials. Key parameters including the exact porosity level, specimen size and crack location with respect to the voids have been considered and their effect on the stress intensity at the crack tip and K-dominant zone size within these materials are examined. The full near-tip stress field is investigated and both, the singular and non-singular stresses, for specified loads that stress the crack-tip below the critical stress intensity factor are estimated. The adopted approach focuses on the local stress field around the crack tip, but does not include any assumptions regarding softening, as adopted in quasi-brittle materials.

4.1 Finite Element model

For this chapter, the case of a highly idealised material was considered, and respective models were created by arraying a unit cell, as described in Chapter 3. Each unit cell contained a single, circular void, whose centre was located at the centroid of the unit cell (Figure 4.1). These voids were placed in an equilateral triangular arrangement (given that $Size_x = 3.5mm$ and $Size_y = \sqrt{3}Size_x/2$, as seen in Chapter 3), implying approximately isotropic behaviour of the macroscopic material [78].

The design variables of this study are the specimens' porosity (controlled by the void's diameter, d) and size (controlled by the rows of unit cells in the y-direction in each specimen arm, N_{c_y}). Geometrically similar models of six sizes were created for each case, containing from 1 to 6 rows of unit cells in the y-direction arranged symmetrically about the crack, N_{c_y} , (Figure 4.1). Note that, since only half the model is generated, the void formation in the first row adjacent to the crack does not follow the triangular topology seen in the rest of the beam, but instead forms a rectangular pattern, symmetric about the crack plane. This symmetry is exploited in the numerical model and loading is pure mode I. The porosity of the specimen was varied from approximately 5 - 45% by changing the void diameter as detailed in Table 4.1.

After the model was created, it was loaded with a single transverse load at its free end, which was scaled so that in all cases the moment at the crack tip remained constant. A symmetric boundary condition was set (see Figure 3.6b), which was modified to

Table 4.1: Specimen porosity for each given void radius.

Void radius (mm)	0.82	1.16	1.64	2	2.32	2.46
Sample porosity P (%)	4.98	9.96	19.96	29.61	39.85	44.80

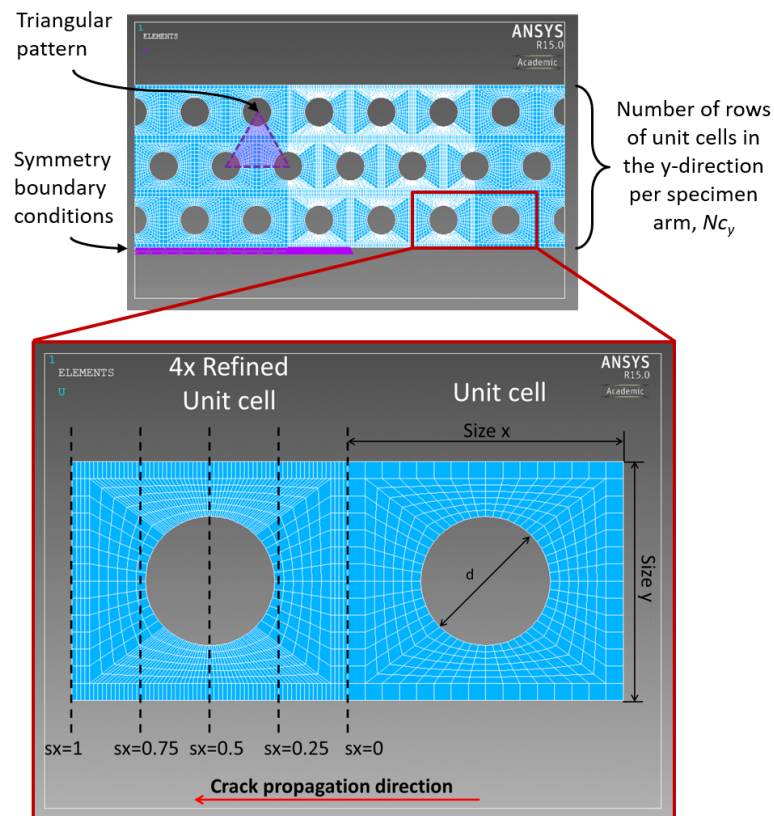


Figure 4.1: Top: Void topology on idealised specimens. Note that in this picture $N_{c_y} = 3$ and $sx = 1$. Bottom: Unrefined and near-tip, refined unit cells. The locations sx were the crack tip was assumed are marked on the figure.

simulate five different crack tip locations, sx (as can be seen in Figure 4.1). The analysis focused on the stress field in the crack-tip and the linear extension in front of the crack-tip, in order to evaluate the existence of a size effect and estimate the size of the K-dominant zone for each different model generated.

As a reference for the computational cost of each simulation, note that the homogeneous models of $N_{c_y} = 1$ included 31230 elements and took approximately 5 seconds to complete a simulation (including creating the geometry, meshing and performing loops to estimate the stress intensity for all 5 sx values), while a homogeneous model of $N_{c_y} = 4$ included 991440 elements and run a full simulation, as described before, in approximately 1000 seconds.

4.2 Results and Discussion

In the results presented below, it is important to note that even though the specific values of stresses are influenced by the applied load, the value of the degree of K-dominance, Λ , and the size of the K-dominant zone are uniquely controlled by the specimen's geometry and the specifications of its internal mesostructure, independently of the material and load. The normalized amplitude of $A_{1/2}$ stresses, C , is affected by variations in the load F in a similar manner to the local stresses. Thus, the ratio C/K_I remains unaffected by externally applied variations and only depends on the material's geometrical features. That makes the absolute values of the applied load inconsequential in the interpretation of the results presented below.

Due to the scaling of the load to reflect changes in size, all different sizes are considered non-dimensional in the sense that their absolute size is not as significant as the configuration (i.e. number of rows) they represent. This can be validated by the fact that for the homogeneous case, all different sizes would give identical values of stress intensity. In other words, when shrinking the unit cell to one quarter of the size described in the paper and creating a specimen with two numbers of rows, (whose size in absolute values would be identical to the specimens with the original unit cell size described in the paper with an $N_{cy} = 1$), the resulting stress intensity, both mesoscopically and macroscopically, would be identical to that of the specimen with

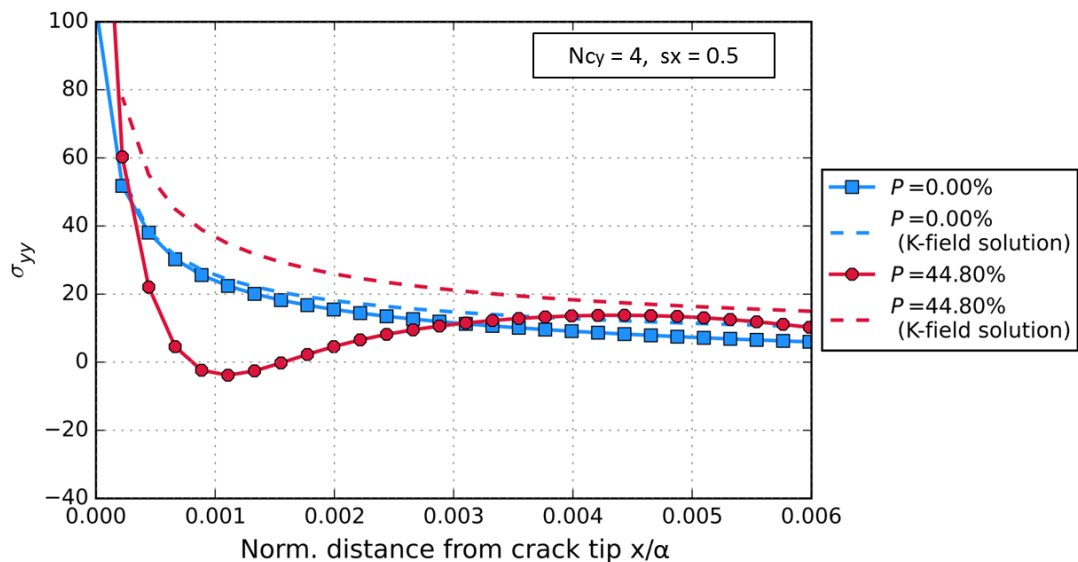


Figure 4.2: FEA solutions (solid lines) vs analytically determined K-field solution based solely on the on the influence of the SIF (dashed lines).

the 4x larger unit cell and $N_{c_y} = 2$, regardless of their difference in absolute size. Thus, it seems that the number of voids in the near-tip area influences the stress intensity at the crack tip and cannot be omitted by homogenisation of the materials geometry.

The significance of the non-singular stresses on the value of K_I of a porous material can be identified from the FEA results. Figure 4.2 shows the discrepancy between the FEA solution for the stress intensity ahead of the crack tip and the analytical K-field solution which only considers the singular stress term in estimating the stress field. In the homogenous case, singular stresses seem to be the significant term in fracture, with the analytically estimated stress field being almost in total agreement with the FEA solution. However, for porous materials, considering the singular stresses alone gives an inaccurate analytical prediction of the near-tip stress field.

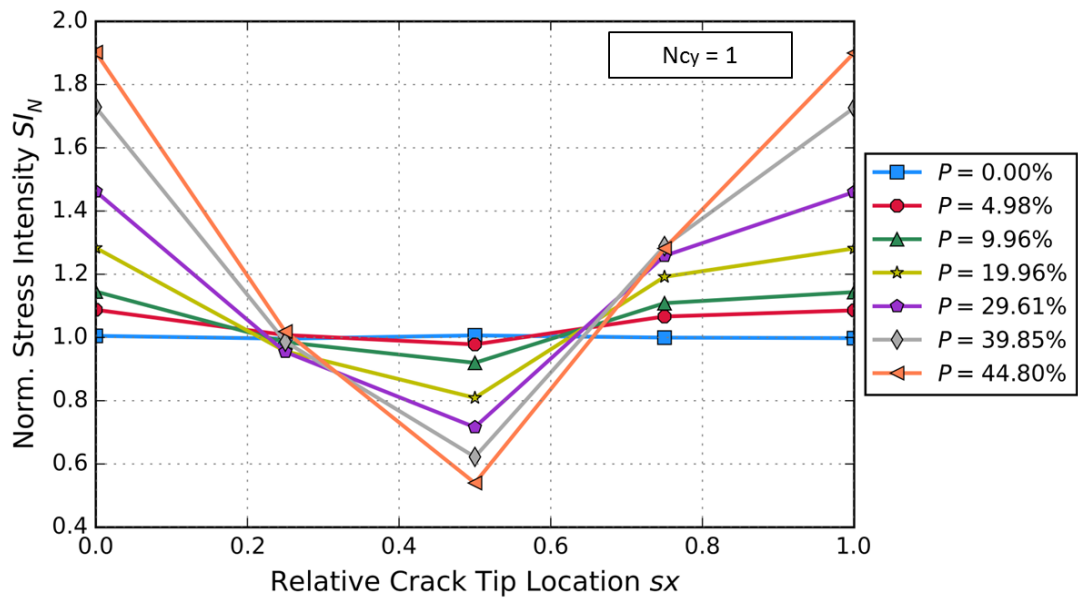
In the following sections, the influence of the non-singular stresses on the results derived will be presented at two focus levels: a) The porous structure level, referred to here as the meso-scale, and b) The homogenized material level, referred to as the macro-scale.

4.2.1 Mesoscale: Porous structure

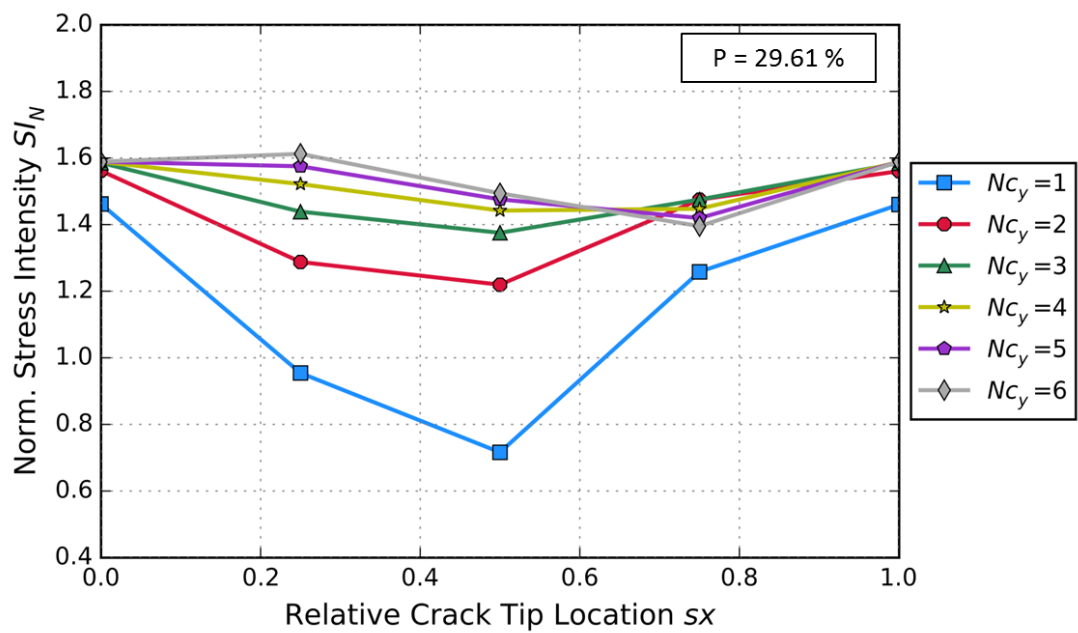
Porous materials exhibit local K_I values which are controlled by the material's mesostructure directly in the vicinity of the crack tip. In this section, FEA results show that for all specimens the normalised stress intensity SI_N follows an oscillating pattern for different crack tip locations relative to the void, which is periodically repeated for consecutive cells (Figure 4.3a, 4.3b). This periodicity is linked to the nature of the prescribed mesostructure, which is non-random, with voids following a regular pattern, this being symmetric about the crack plane.

It is found that the amplitude of the oscillation of SI_N , diminishes when the size of the heterogeneity in the near tip field becomes less significant compared to the specimen's dimensions; at both fixed specimen size (Figure 4.3a) (also seen in [58]) and fixed void size (Figure 4.3b). Apart from the amplitude of the oscillation, the mean value about which SI_N oscillates increases with size, appearing to converge to a plateau for large specimens. Interestingly, the regions around the void, where either amplification or shielding is observed, appear to invert as the size of the specimen decreases (Figure 4.3b). Specifically, for progressively smaller specimens the stress variation inverts, reaching a maximum at the edges of the cell (i.e. $sx = 0$ and $sx = 1$) and a minimum exactly under the void ($sx = 0.5$). However, as the size of the specimen increases, the locations of the maxima and minima of the oscillation are repositioned to locations before ($sx = 0.25$) and after ($sx = 0.75$) the void respectively.

For comparison, a full specimen model was created with a triangular but non-



(a)



(b)

Figure 4.3: Fluctuations of $S/_{IN}$ for different crack initiation locations relative to the void a) Size $N_{c1} = 1$ for porosities=5-45%, b) Sizes $N_{cy} = 1 - 6$ for 30% porosity. Graphs for other specimen sizes and porosities can be found in Appendix B.

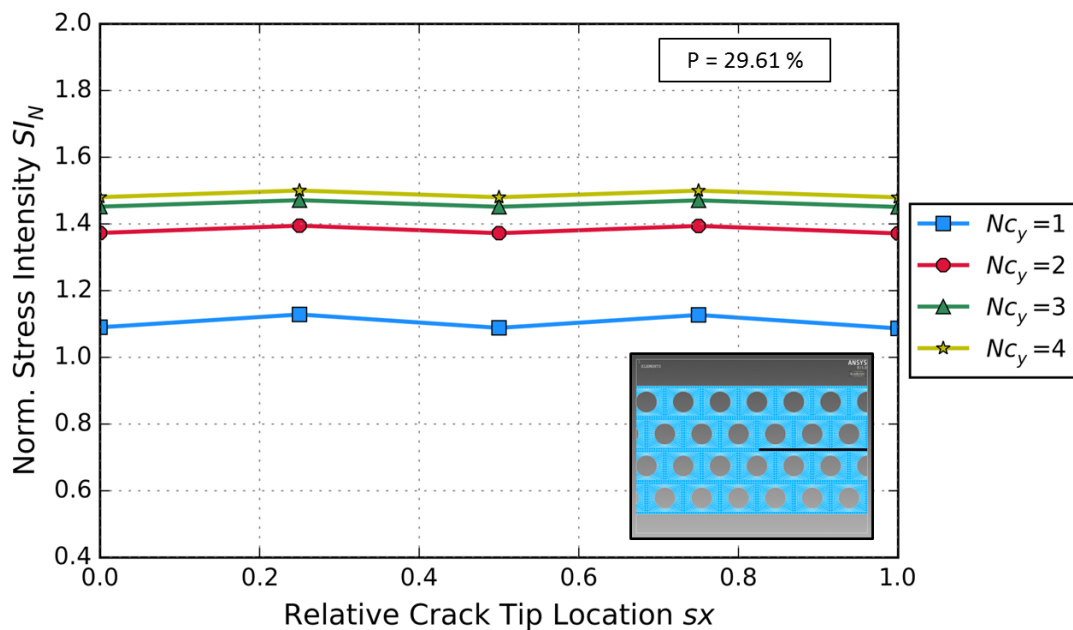


Figure 4.4: Sizes $N_{c_y} = 1 - 6$ for 30% porosity model with triangularly arranged voids equilaterally to the crack.

symmetric void pattern adjacent to the crack plane (see inset of Figure 4.4), consistent with the pattern throughout each beam. The model was created with a 30% porosity and was run for $N_{c_y} = 1 - 4$. The asymmetry of the voids around the crack tip introduces a mode II component in the near-tip stress field. However, the magnitude of the mode II component contributes to only approximately 7.5% of the effective mixed mode stress intensity ($K_I = 38.53MPa\sqrt{mm}$ and $K_{II} = 2.90MPa\sqrt{mm}$ for $s_x=0.75$ where their percentile difference is the smallest, effective mixed mode stress intensity is estimated as $K_{eff} = \sqrt{K_I^2 + K_{II}^2}$) for the smallest specimen, where the contribution of Mode II stresses is most apparent since the void size dimensions are significant compared to the specimens dimensions. Thus, predominantly mode I behaviour is assumed. The local stress intensity of these models exhibits significantly diminished oscillation throughout the unit cell, as seen in Figure 4.4. This is attributed to the averaging of the two almost contrasting, overlapping stress fields on either side of the crack plane, caused by the non-symmetric equidistant voids near the crack-tip.

The oscillatory behaviour seen in Figure 4.3 is consistent with that found during previous investigations on the variance of local SIFs at various distances and angles around a single circular void [58, 60] nearby the crack tip in infinite media. Any discrepancies with the fluctuations found here are attributed to the existence of neighbouring voids which further alter the stress distribution. Han et al. [60], while studying the effect

of microvoids near a bi-material interface crack of quasi-brittle behaviour, attributed these fluctuations to the T-effect. Even though mode I loading was studied, the non-symmetric, bi-material interface crack studied gave rise to stress components in the x-direction additionally to the expected stress in the y-direction. It was then suggested that the x-direction, non-singular T-stress is relaxed inside the voids, consequently having a direct impact on the SIF of the material, instead of indirectly affecting the SIF by altering the size of the fracture process zone, as it is usually assumed. Thus, a combination of the relative location of the crack tip with the T-stress sign was found to either amplify or shield the material's SIF.

Though, initially the variations of the mesoscopic stress field were thought to be attributed to this relaxation of the T-stresses in the presence of a void [128], in retrospect it is believed that this is not the case for the materials under focus in this thesis. In the idealised models studied here, due to symmetric boundary conditions, pure mode I behaviour is exhibited. Since, the stress intensity SI_N is only estimated from the y-direction stress, σ_{yy} , and the fracture process zone is considered minimal, there is no indication as to how the T-stresses might be significant. However, it can be deduced

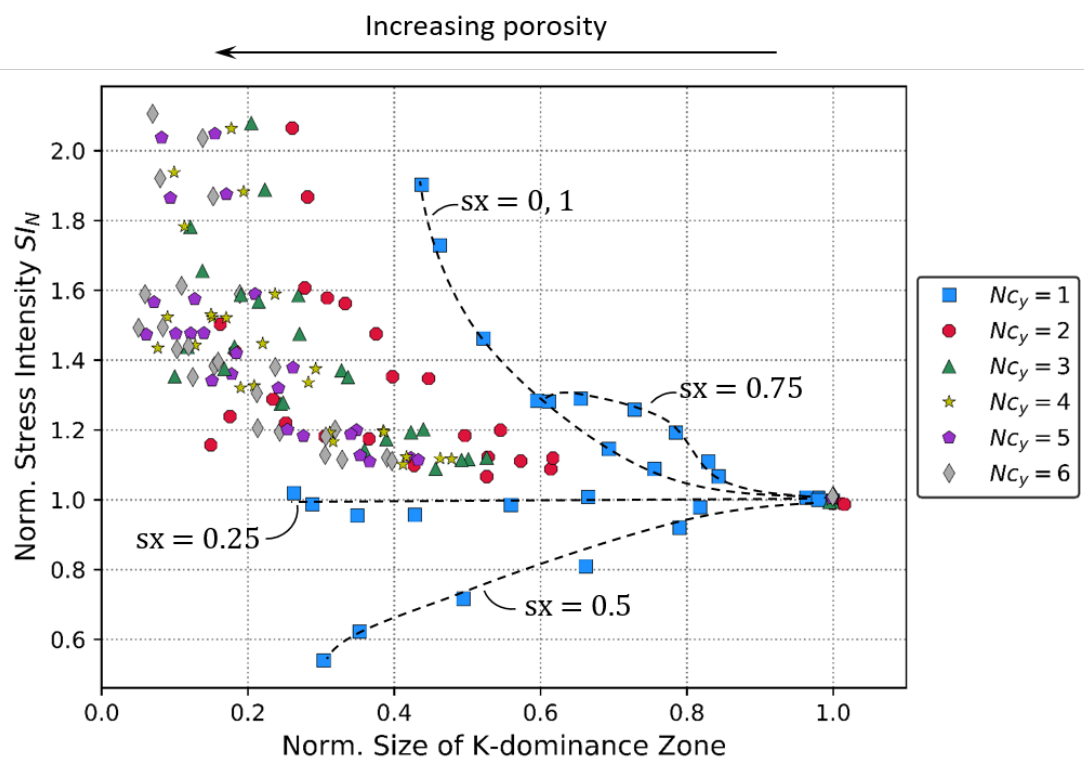


Figure 4.5: Variation of SI_N with size of K-dominant zone. In all graphs porosity increases from the right to the left side of the graph.

from [60] that, since non-singular stresses can directly affect the exhibited stress at the crack tip, the size of the K-dominant zone may be immediately influenced by the mesostructure of the material in the near-tip field and could lead to large discrepancies in the local stresses around the crack tip depending on the void's relative location.

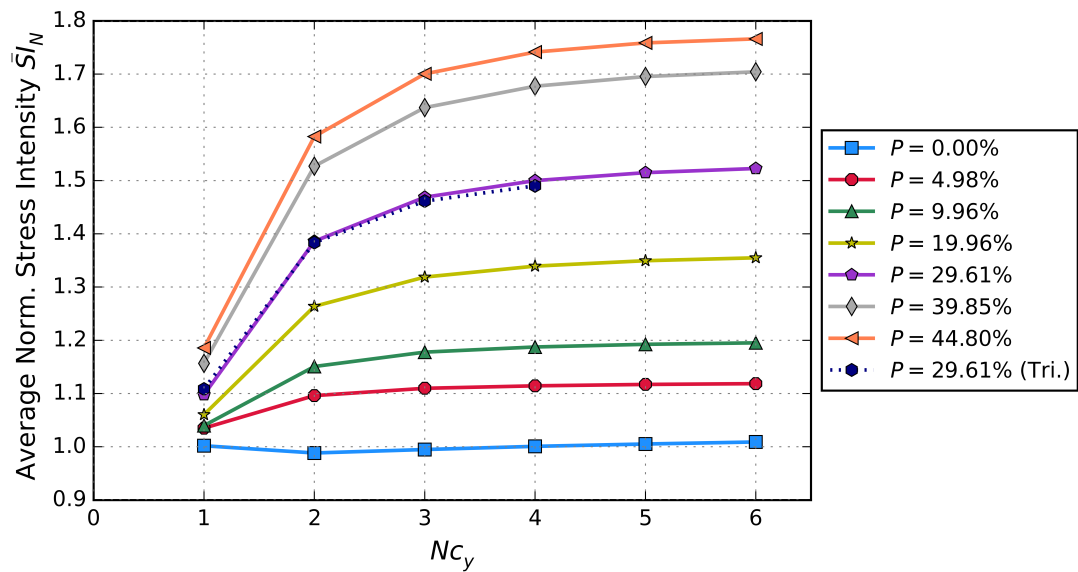
A similar conclusion can be drawn from the results of this study by plotting the size of the K-dominant zone, normalised with the respective value of the homogenous case for each specimen size, with the normalised stress intensity, SI_N (Figure 4.5). As the size of the K-dominant zone becomes smaller, the stress intensity variations exhibit larger deviations from the value of the homogeneous case ($SI_N = 1$). In fact, it is observed that as the specimen get larger, the region of the diaspora of the points for each specimen size becomes thinner and seemingly converges to a hyperbolic path for specimens with $N_{c_y} = 6$. This diaspora is dependent on the relative crack tip location sx . On Figure 4.5, the different "paths" of the relationship between the normalised size of the K-dominant zone and SI_N formed by different values of sx are indicated for the smallest specimen size.

4.2.2 Macroscale: Homogenized material

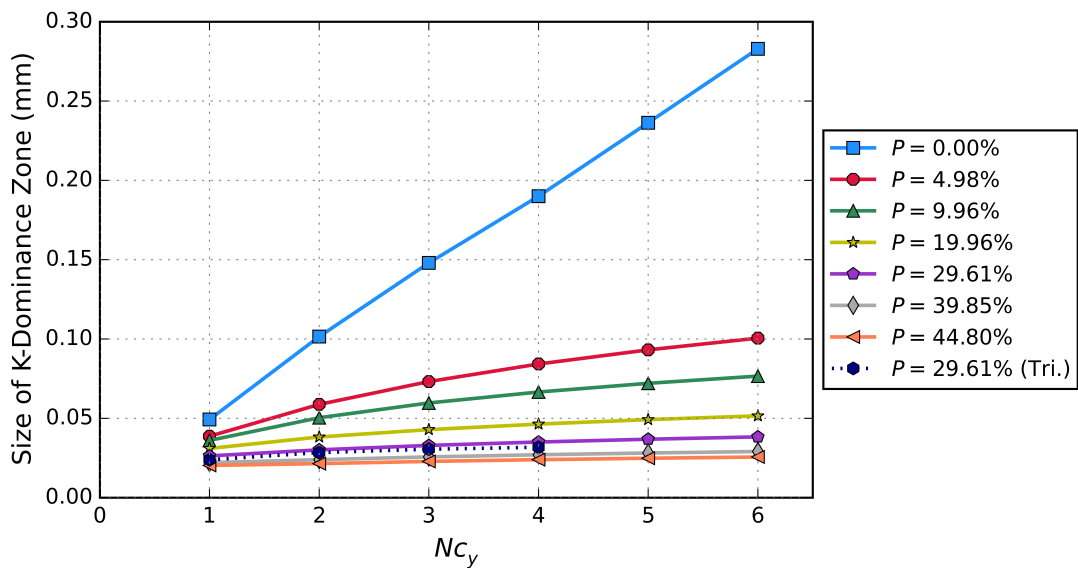
The topology-dependent stress variation can be circumvented by introducing an average normalised stress intensity \overline{SI}_N per model, which results from averaging the local SI_N values derived for relative crack tip locations $sx = 0 - 0.75$ ($sx = 1$ is not considered due to periodicity of the solution). Thus, each specimen can be considered to be a homogenized medium of given porosity and size, without focusing on the specifics of its mesostructure.

The estimated average values are plotted in Figure 4.6a. Previous research on the fracture properties of porous materials has mainly focused on infinite media, assuming that any specimens cut from the same brittle material, characterized by the same porosity and microstructural features, will in fact exhibit the same fracture behaviour [29, 62, 129]. However, this study suggests that, for constant porosity, smaller specimens will appear tougher than their larger counterparts since they exhibit lower stress intensities for the same loading. In fact, 1-row specimens have significantly different behaviour than larger specimens, which seem to converge asymptotically to an approximately constant value above four rows of unit cells. This size effect becomes more pronounced with increasing porosity (Figure 4.6a).

Figure 4.6a also shows that stress at the crack tip is proportional to the porosity of the specimen, with all porous materials exhibiting higher stress intensity at the crack tip than the homogeneous case. The averaged stress intensity for the model with the non-symmetric pattern around the crack (inset of Figure 4.4) is also depicted (dark



(a)



(b)

Figure 4.6: Size effect in fracture of porous materials. a) Smaller specimen exhibit lower stresses for a given load, implying an apparently tougher material. The larger the porosity the more prominent the size effect. b) Dependence of K-dominant zone size with specimen size.

blue, dashed line in Figure 4.6a and 4.6b). Even though its mesoscopic behaviour is distinctively different to its symmetric counterpart, macroscopically their behaviour is almost identical.

LEFM predicts that when the size of the K-dominant zone is large enough to fully engulf the fracture process zone, the value of the stress in the vicinity of the crack tip is purely dependent on the value of the SIF and should remain constant. For porous materials, the size of the K-dominant zone is largely affected by the existence of discontinuities in the material. The difference between the size of the K-dominant zone in the homogeneous case and the porous specimen is monotonically rising with increasing sample size (Figure 4.6b). Even a porosity of 5% can shrink the size of the K-dominance zone to almost half its original size for just 2 rows of unit cells. In that case it is not immediately evident that the K-dominant zone is large enough to assume that the near-tip stress field can be fully described by a single parameter, and thus, it cannot be concluded that the $A_{1/2}$ stresses can be safely neglected.

Indeed, plotting the average normalised stress intensity at the crack tip as a function of the averaged normalized amplitude of $A_{1/2}$ stresses, \tilde{C} , an almost linear relationship as \tilde{C} approaches zero can be seen (Figure 4.7a). With the exception of the smallest specimen, the magnitude of the slope of this line increases with decreasing specimen size. As \tilde{C} reaches the value of the homogenous case, all series converge to the stress value for this case. It is suggested that the average normalised stress intensity at the crack tip and the normalized amplitude of the $A_{1/2}$ stresses \tilde{C} are related by:

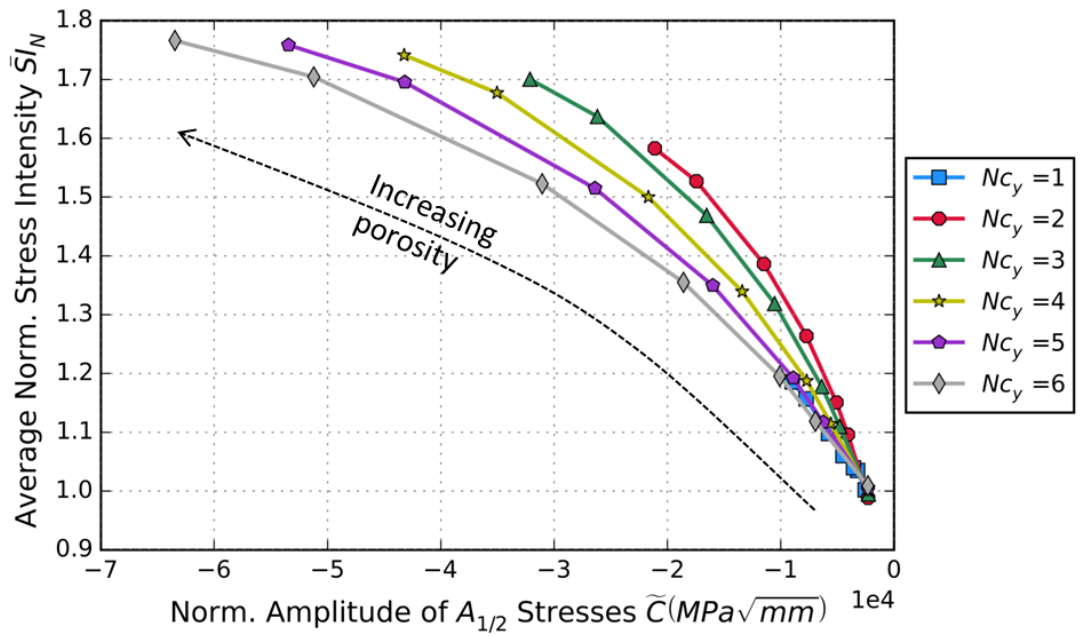
$$\overline{SI}_N = f(\tilde{C}) \sqrt{\frac{P}{Nc_y}} \quad (4.1)$$

where Nc_y = Number of cells in y-direction (-)

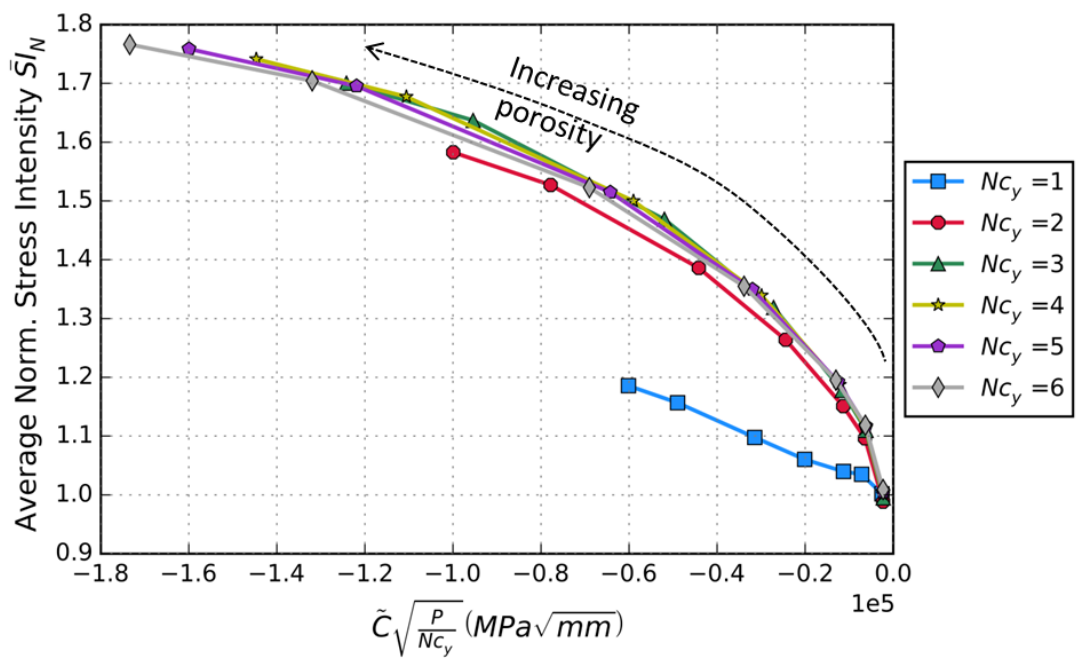
P = Specimen porosity (-)

The data of Figure 4.7a have been re-plotted in Figure 4.7b taking into account equation 4.1. It is now apparent that specimens with just one row of unit cells (blue curve in Figure 4.7b) exhibit a behaviour inconsistent with their larger counterparts.

The averaged normalized amplitude of $A_{1/2}$ stress \tilde{C} seems to be closely related to the geometrical features of the specimen (Figure 4.8). As porosity and specimen size decrease, \tilde{C} tends asymptotically to the value of the homogeneous case, which is the dotted line in Figure 4.8, used as a reference. This indicates that for the given loads, \tilde{C} varies as:



(a)



(b)

Figure 4.7: a) Average normalised stress intensity \bar{S}_{I_N} variation with averaged normalised amplitude of $A_{1/2}$ stresses \tilde{C} , b) Inclusion of correction factor $\sqrt{P/N_{c_y}}$ in graph (a)

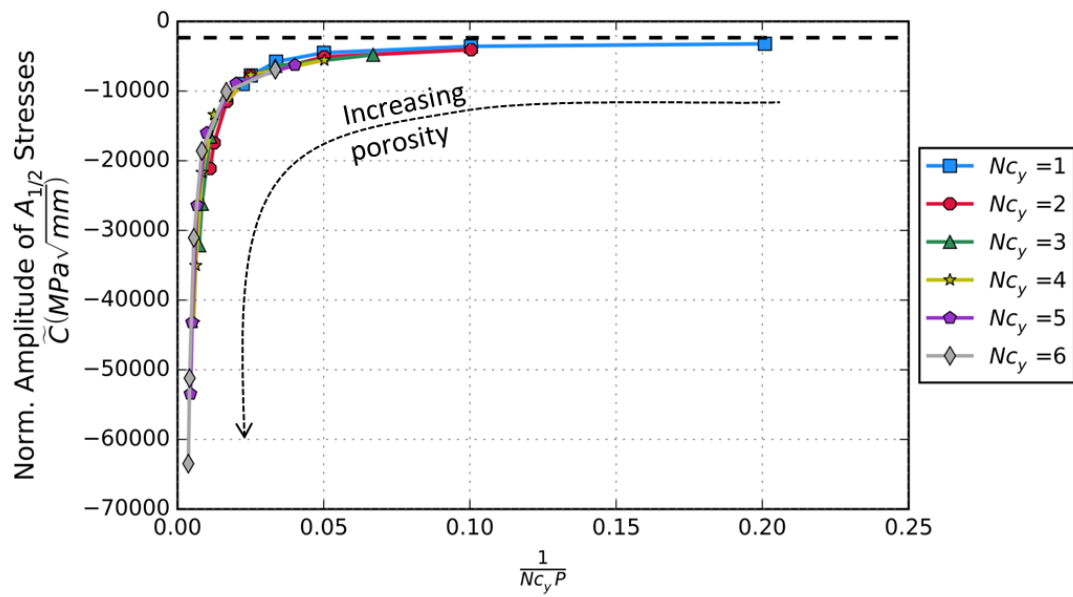


Figure 4.8: Dependence of normalised amplitude of $A_{1/2}$ stresses \tilde{C} with number of cells in y -direction, N_{c_y} , and specimen porosity, P . The horizontal dashed line represents the value of \tilde{C} for the homogeneous case.

$$\tilde{C} = f\left(\sqrt{\frac{1}{N_{c_y}P}}\right) \quad (4.2)$$

Dividing the dimensional factor found in 4.2 with the one found in 4.1, the geometrical dependency coefficient D_c is derived:

$$D_c = 1/\sqrt{(N_{c_y}P^3)} \quad (4.3)$$

The average normalised stress intensity at the crack tip \overline{SI}_N can thus be accurately plotted as a function of the dependency coefficient (Figure 4.9). Through parameter fitting the following relation is estimated:

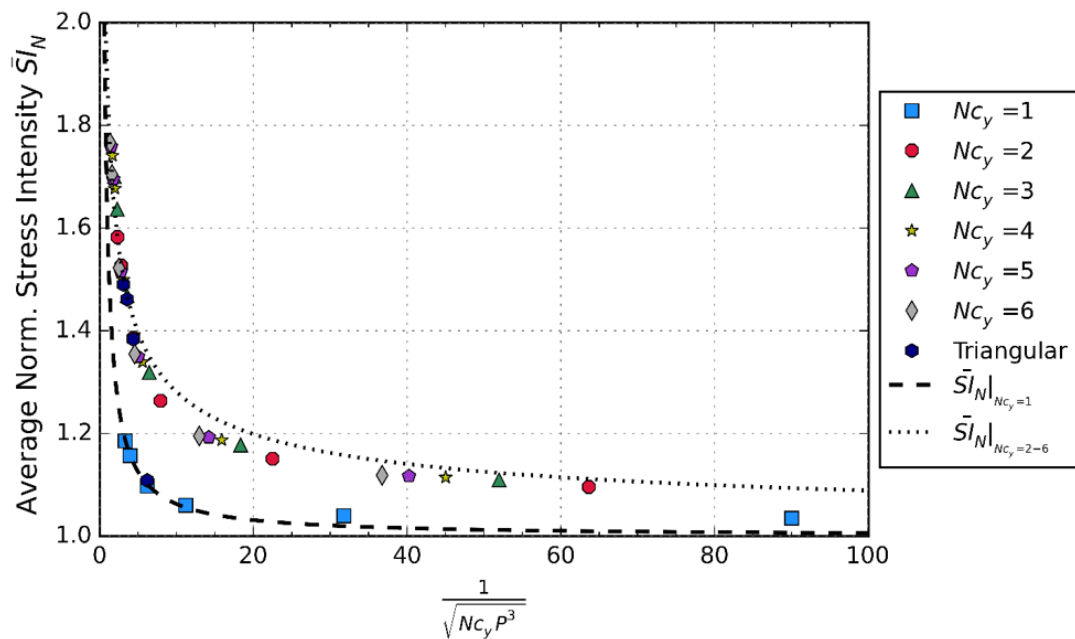


Figure 4.9: Correlation of scaling factor with the geometrical dependency coefficient. The fitted equations 11 is also plotted on the graph.

$$\bar{S}_{N|Nc_y=i} = \begin{cases} \frac{0.89}{D_c\sqrt{2}} + 1 & , if \ i = 1 \\ \frac{0.89}{\sqrt{D_c}} + 1 & , if \ i > 1 \end{cases} \quad (4.4)$$

, where the standard error of estimate s_{est} for specimen with 1 row of unit cells is $s_{est} = 0.014$, while for larger specimen ($i > 1$) $s_{est} = 0.035$.

The exact value of the average stress intensity at the crack tip of the porous material K_I^P for a given load can then be estimated according to Equation 3.9 as:

$$K_I^P = \bar{S}_{N|Nc_y=i} * K_I^H \quad (4.5)$$

It is interesting to note that even the values of the model with the triangular non-symmetric void arrangement about the crack also comply with this formula.

4.3 Conclusions

This chapter investigates the influence of specimen size and porosity on the stress at the crack tip both mesoscopically (at the pore level) and macroscopically (at the homogenized material level), before the critical stress intensity value. The results indicate that it is inadequate to refer to one unique stress intensity for porous materials, as the inclusion of only singular stresses would suggest. The presence of the pores, as well as the size of the specimen, have a direct impact on the size of the K-dominance zone on each model, which is subsequently reflected on the stress intensity at the crack tip of the materials studied. Furthermore, it is observed that when the size of the specimen is reduced to just one row of unit cells, the fracture behaviour exhibited is not consistent with the behaviour of larger specimen.

In summary, the following conclusions can be drawn:

- At the mesoscopic level, the existence of local stress intensities for porous materials has been confirmed in this study. Here, it is attributed to the shrinking of the size of the K-dominant zone by the presence of voids. Specifically, it has been found that the largest variations of the stress intensity are exhibited for the cases with the smallest K-dominant zone sizes. The exact relationship between the size of the K-dominant zone and the stress intensity is rather complex though, and seems to be size-related.
- Looking at the material macroscopically a prominent size effect can be observed. As the specimen size increases, the material may appear to become less tough, until it converges to a specific value, assumed to be that of the infinite medium. As expected, an apparent weakening effect is also exhibited with increasing porosity. Both behaviours are closely related to the amplification of the $A_{1/2}$ stresses, which become significant when compared to singular stresses, rendering the consideration of higher-order terms necessary in predicting the fracture behaviour of heterogeneous specimens.
- An empirical relation has been derived to predict the average stress intensity at the crack tip of porous materials with low to medium porosity. The model was created based on FEA data obtained for DCB specimens where the porosity was introduced in the form of circular unit cells in a periodic array.

CHAPTER 5

Experimental validation and sensitivity to mesostructural changes

In the previous chapter, the significance of non-singular stresses on the size effect observed in porous materials was investigated in idealised topologies. The results showed that the existence of porosity can significantly reduce the size of the K-dominant zone, causing variations in the estimated stress distribution at the crack tip for different specimen sizes and porosity levels.

This chapter attempts to experimentally validate these findings¹. During the review of the literature (Chapter 2) the experimental observation of size effects in porous materials was established. However, the discussed literature referred to materials of a quasi-brittle nature and attributed the observed size effects to plastic phenomena becoming more prevalent at small scales [11, 95, 130]. A number of studies linked this behaviour with a reported increased significance of non-singular stresses [105–107]. In fact, the visualisation of the near-tip stress field with the use of photoelasticity in homogeneous materials, has highlighted the need for more terms, in addition to the singular one, in the stress expansion [114, 117].

Here, mode I experiments were performed on DCB specimens manufactured from PMMA and perforated with arrays of holes. During loading, the specimens remained in the linear elastic region (fracture and crack propagation was not reached), hence no plastic effects are considered. The stress at the crack tip for a given load was estimated, in order to confirm the existence of a size effect in brittle porous materials, while the

¹The findings of this chapter have been accepted for publication and are currently in print in the journal of Engineering Failure Analysis.

specimens were observed by means of photoelasticity to provide proof of the influence of the pores on the near-tip stress field. A parametric investigation was subsequently carried out to investigate the impact of manufacturing inaccuracies in the pores' shape on the measured properties.

5.1 Methodology

5.1.1 Experimental setup

The specimens were manufactured by laser-cutting a 10 mm thick PMMA sheet, procured by Stockline plastics. The laser-cutting was done on the Speedy 400 machine by Trotec, using a program job control with the following parameters: Power = 100*Watts*, Speed = 0.1*inch/sec*, Frequency = 5000*hz*. The lens used was a Silicon REFLECTOR with a 24.4*mm* diameter and a thickness of 6*mm*.

In order to address the size effect, specimens of three different sizes were examined (Figure 5.1b), each one being four times larger than its smaller counterpart (specimens of 1, 2 and 4 rows of voids per arm, N_{c_v} , were manufactured). As described in Section 3.1.1, the aspect ratio of the specimens was kept constant at $W/h = 12$ for all sizes, where W and h are the specimen's length and height respectively as depicted in Figure 5.1a. Using laser-cutting, a horizontal crack was created in the mid-plane of each specimen, with a crack length to total specimen length ratio approaching $\alpha/W = 0.5$, where α is the crack length. It was shown in the previous chapter that the local stress intensity oscillates greatly for varying locations of the crack tip with respect to the nearest void. In order to produce comparable results, in all cases the crack tip was designed to be directly below the void, thus producing small variations in the value of the α/W ratio.

Note that the crack was laser cut and was not sharpened further with the use of a sharp razor, as described in ASTM D5045. Due to the different specimen configuration (here, DCB is used instead of SENB or CT, which are suggested in ASTM D5045), the insertion of a razor in the crack tip is a lot more challenging and would require a very thin razor. However, when a razor of 100 μm was used, it was not stiff enough to further sharpen the crack tip. Figure 5.1c shows the near-tip area of the manufactured specimens with the laser-cut crack, magnified using an optical microscope. The crack-tip radius was measured to be 150 μm (Figure 5.1c). Previous studies have shown that the pre-conditioning of the crack tip can impact the measured fracture toughness [131, 132] and fracture mechanics dictates that the stress intensity would be lower for blunt notches. However, in this study the focus is on the relative stress intensity differences between specimens of different sizes and porosity levels. As such, all values obtained

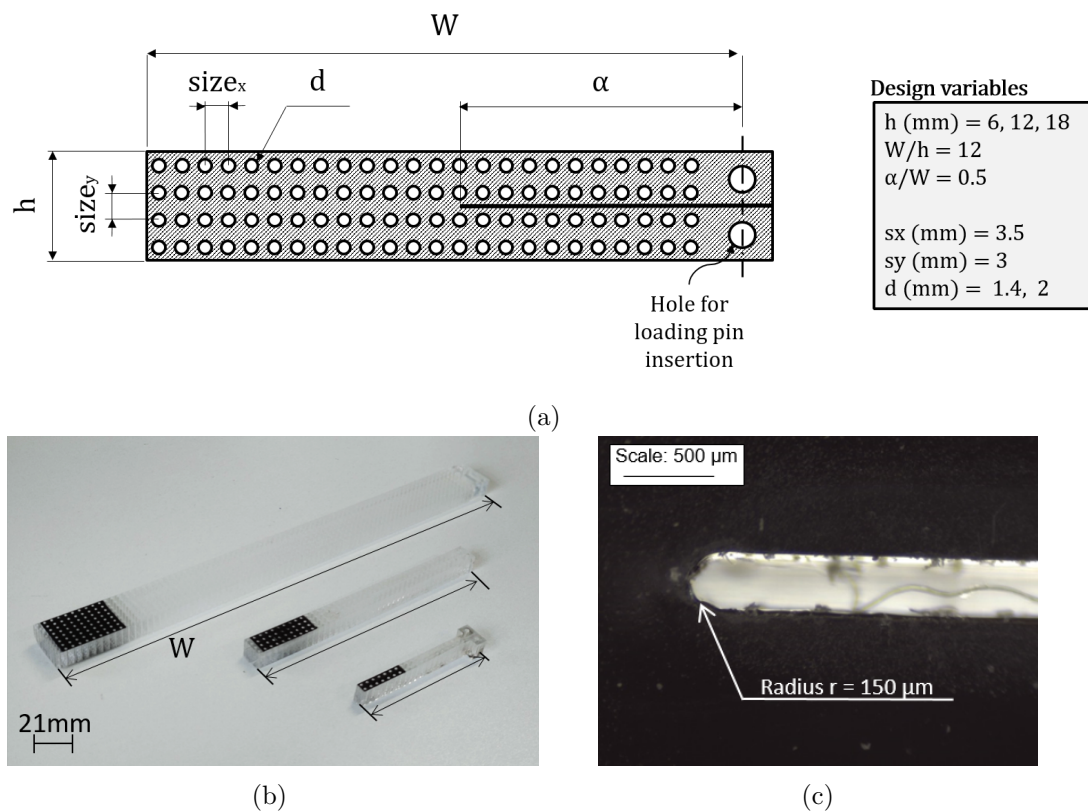


Figure 5.1: Designed and manufactured specimens. (a) Updated schematic of Figure 3.1, showing a more complete picture of the design variables. The definition of the axes x and y are shown on the figure, with x being in the direction of the crack propagation. The same orientation of all pictures of the specimens is kept throughout the chapter. (b) Manufactured specimens of all three different sizes, (c) Crack tip as seen in an optical microscope. The crack tip radius was found to be 150 μm .

from the porous specimens will be normalised by the values of the respective homogeneous specimens, which are manufactured by the same way and are characterised by the same crack tip imprecision. Thus, it is expected that this crack tip imprecision will be normalised out.

Porosity in the specimens was introduced in the form of circular voids, arranged on a rectangular array. Two different levels of porosity were examined, namely 15 and 30 %, that correspond to a void diameter of approximately 1.4 and 2 mm respectively. The distance between consecutive voids was designed as $Size_x = 3.5\text{mm}$ and $Size_y = 3\text{mm}$ in the x - and y - direction respectively (see Figure 5.1a). A series of homogeneous specimens was also manufactured and tested in order to provide a baseline for normalisation. Three specimens were tested for each configuration, leading to a total of 27 specimens (3 specimens, 3 values of $N_{c_y} = 1, 2, 4$ and 3 porosities $P = 0\%, 15\%$ and 30%).

As described in Subsection 3.1.1, the manufactured specimen (Figure 5.1b) were subjected to a quality control procedure before they were considered suitable for testing. Each three specimens selected for testing were considered self-similar, and the dimensions of the specimens' array were adequately accurate. However, due to the polymer stretching caused by the high temperature of the laser, the voids' circularity

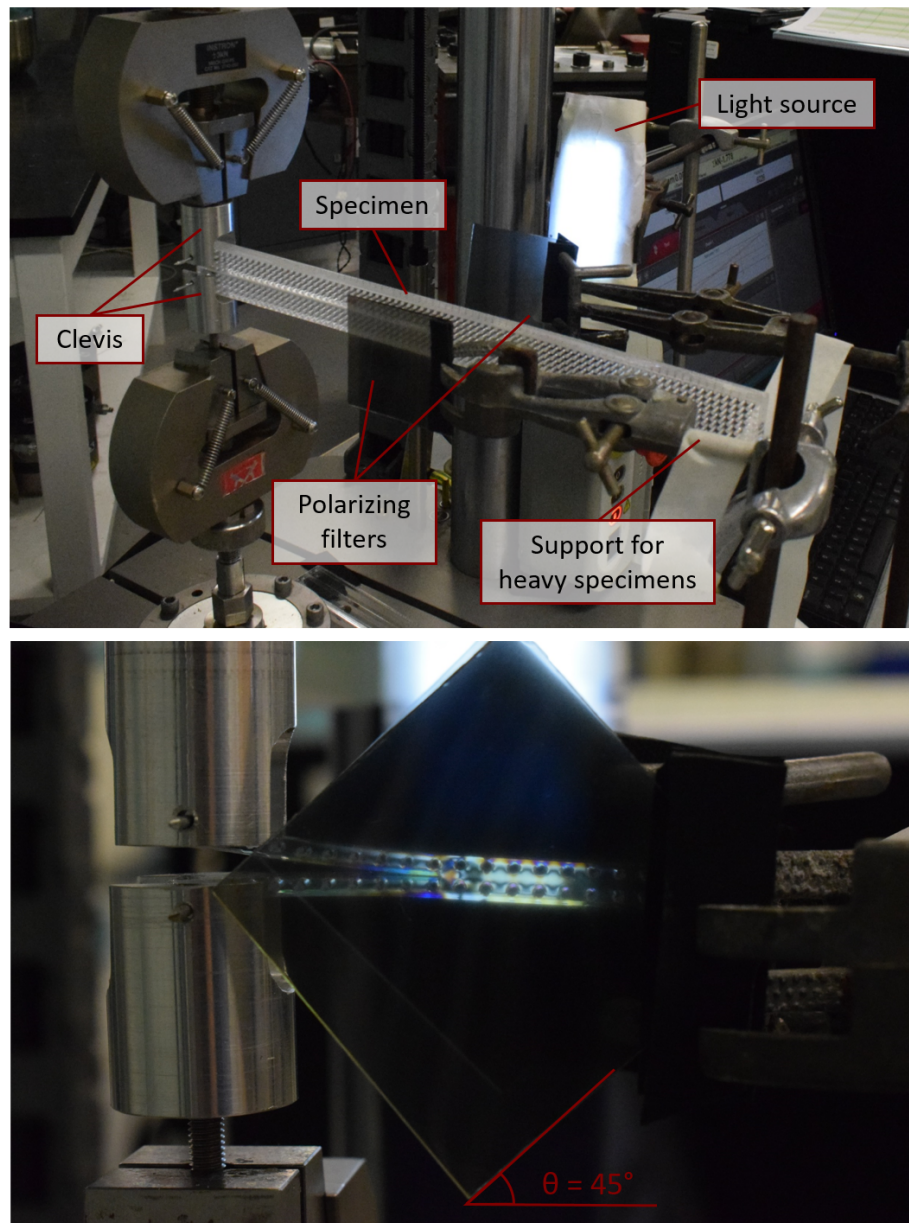


Figure 5.2: Top: Experimental setup, Bottom: Close-up of the polarising filters and their positioning.

and ellipticity was sometimes compromised. These will be more specifically described during the discussion of the results. A complete table with the resulting observations on the quality of the tested specimens can be found in Appendix C.1.

The tests were conducted on an Instron Electroplus E3000, which is an all-electric dynamic testing machine, with a ± 5 kN load cell, and a load weighing accuracy of $\pm 0.5\%$ of indicated load or $\pm 0.005\%$ of load cell capacity, whichever is greater (Figure 5.2). Note that crack propagation is not considered and each specimen testing was stopped before fracture.

During loading, the near-tip stress field was monitored with the use of a circular polariscope to obtain qualitative results on the influence of porosity on the near-tip stress field. When the specimens were loaded with the maximum load, a photo was taken to capture the fringe pattern at that stress state and compare it with that of the numerical results. However, note that the dynamic nature of the experiment introduced a certain level of uncertainty and the precise load at which the photos were taken might deviate to a small extent, up to 15%, from the intended value. Yet, while such small deviations are expected to somewhat affect the intensity of the patterns, the qualitative patterns, which are the focus of photoelasticity in this study, should remain the same.

5.1.2 Numerical approach

In order to validate the experimental results, two-dimensional Finite Element (FE) models of the specimens were created, using the commercial software ANSYS. The void diameters ($d = 1.4$ mm and 2 mm), specimen sizes ($N_{c_y} = 1, 2$ and 4) and aspect ratio ($AR = 12$) of the specimen are designed in accordance with the manufactured specimens. The unit cell size ($Size_x = 3.5$ mm and $Size_y = \sqrt{3}Size_x/2$) and design, meshing, boundary and loading conditions are consistent with the ones presented previ-

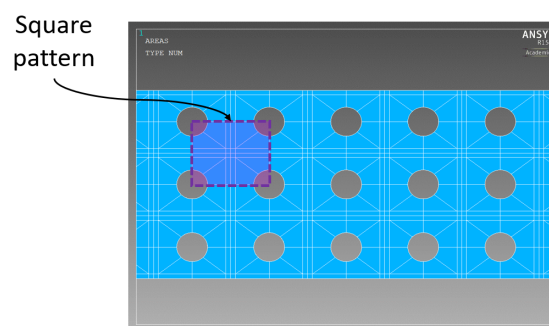


Figure 5.3: Finite Element (FE) model with rectangular array, reflecting the topology of the manufactured specimens.

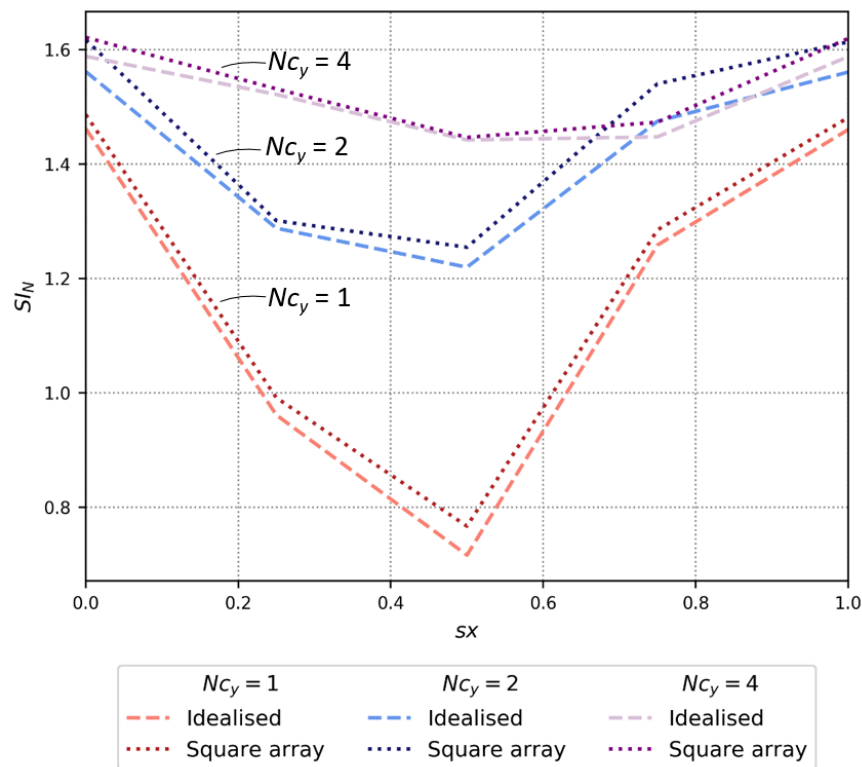


Figure 5.4: Difference of normalised stress intensity between the models with the triangular (idealised) and the rectangular void topology, for porosities of $P = 29.61\%$ ($d = 2mm$). Note that the estimated differences may be due to the different aspect ratios of the two studied cases.

ously in Chapters 3 and 4. However, here, the voids are instead placed in a rectangular array, as in the manufactured specimens (Figure 5.3).

The differences between the models with the triangular and rectangular arrays are estimated to be minimal, yet distinguishable (Figure 5.4). Note that the models with $N_{c_y} = 1$ have the same topology in both cases and are only differentiated by the specimens' aspect ratio ($AR = 20.8$ for the idealised case, while $AR = 12$ for the specimens with a rectangular array). However, specimens of both topologies present very similar trends, which may also be highlighted due to the difference in the specimens' aspect ratio and crack length. However, the existence of the size effect is obvious in both cases and no qualitative differences are expected in the results due to their differences.

As discussed in Section 3.2.2, the stress intensity from the numerical results was estimated using the projection method, as it directly estimates the stress intensity by focusing on the nodal stresses ahead of the crack tip. However, due to technical limitations, during the experimental study the BT expression (Equation 3.4) was used

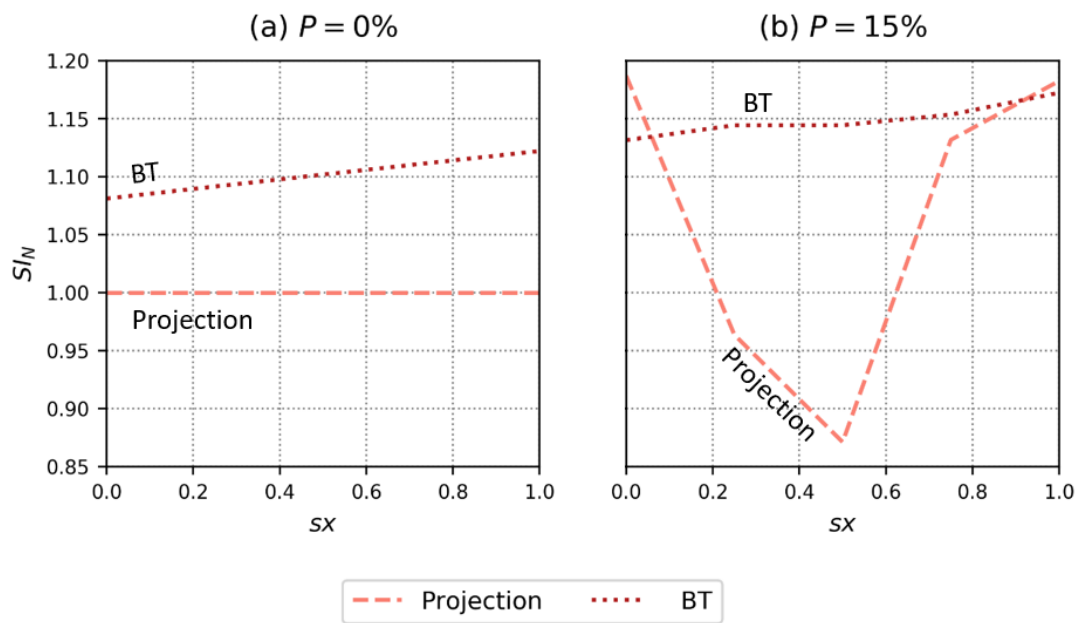


Figure 5.5: Difference between the values of normalised stress intensity as estimated by the projection method (see Section 3.2.2) and the Beam Theory (BT) expression (Equations 3.4 and 3.5) for homogeneous and porous specimens of $Nc_y = 1$.

to estimate the stress intensity instead, which is a more indirect way of measurement. In order to quantify the uncertainty caused by the difference between the methods, the stress intensity was estimated using both methods for FE models of homogeneous and porous specimens (Figure 5.5). A maximum discrepancy of approximately 11.5% was observed for the homogeneous case (for models of $Nc_y = 1$). Additionally, the stress intensity estimated using the BT expression was found to be a lot more sensitive to the variation of the crack length (varied by the change in sx), which can also be attributed to the fact that in the experimental models the crack was shorter than that suggested by the relevant testing standards. However, in the case of a porous material, the BT is a lot less precise, failing to capture the local variations in the stress intensity caused by the near-tip void. This will also be shown more explicitly in the results discussion. Despite the BT expression's inaccuracies, it is considered more appropriate to focus on the comparison of both, experimental and numerical, results estimated with this method, to ensure consistency.

5.2 Experimental results

The isochromatic fringes for all cases are presented in Figure 5.6, along with the ones predicted from FEA. As discussed in Chapter 3, the isochromatics consists of bands of the same colour and represent the loci in the material where the differences of the two principal stresses ($(\sigma_1 - \sigma_2)$) is constant. Qualitatively, the experimental results appear to generally agree with the numerically computed results in all different cases. This acts as a preliminary validation of the numerical results. As described in the methodology section of this chapter (Section 5.1.1), the load at which the experimental photos were taken might differ up to 15% from the load at which the numerical fringe pattern was estimated. It is emphasised here that the photoelasticity study is highly qualitative and aims to identify disturbances within the stress field caused by the presence of voids in the near-tip area, rather than produce quantitatively accurate conclusions.

For the homogeneous case (see Figures 5.6c 5.6d, 5.6g and 5.6h) it is shown, both experimentally and numerically, that the isochromatics follow a smooth pattern, with ellipsoidal hoops expanding behind the crack-tip for a certain length, as is expected for Mode I loading [116, 118]. The photoelastic fringe for all sizes of the homogeneous case exhibit the same trends in shape, with the zone in which these stresses appear seeming to scale proportionally with size.

The isochromatics presented in porous materials show a quite different picture (Figures 5.6a, 5.6b, 5.6e and 5.6f). The perforations in the material seem to act as a disturbance in the expansion of the stress field in the near-tip area, altering the general shape and size of the stress distribution. In fact, for specimens with just one row of unit cells per arm (Figures 5.6a, 5.6b), the isochromatic fringe is mildly changed through the existence of the voids, though retaining its similarities to the homogeneous case. However, in larger specimen (Figures 5.6e, 5.6f) a more chaotic pattern is exhibited, with seemingly little correlation to the original, ellipsoidal hoops. The FE models capture the size and general shape of these stress fields satisfactorily.

The photoelastic fringe pattern has been used in previous research to experimentally estimate the stress intensity factor and indicate the need of the inclusion of non-singular terms in the estimation of the stress intensity factor in homogeneous specimens of varying sizes and configurations [114–117]. In porous materials, due to the widely irregular nature of the fringe pattern, the coefficients of the Williams series cannot be extracted. However, a visual inspection clearly shows that the existence of pores acts as a disturbance in the expansion of the stress field in the near-tip area, which could justify the need to include non-singular terms, in addition to the singular term, to accurately reconstruct the isochromatics pattern.

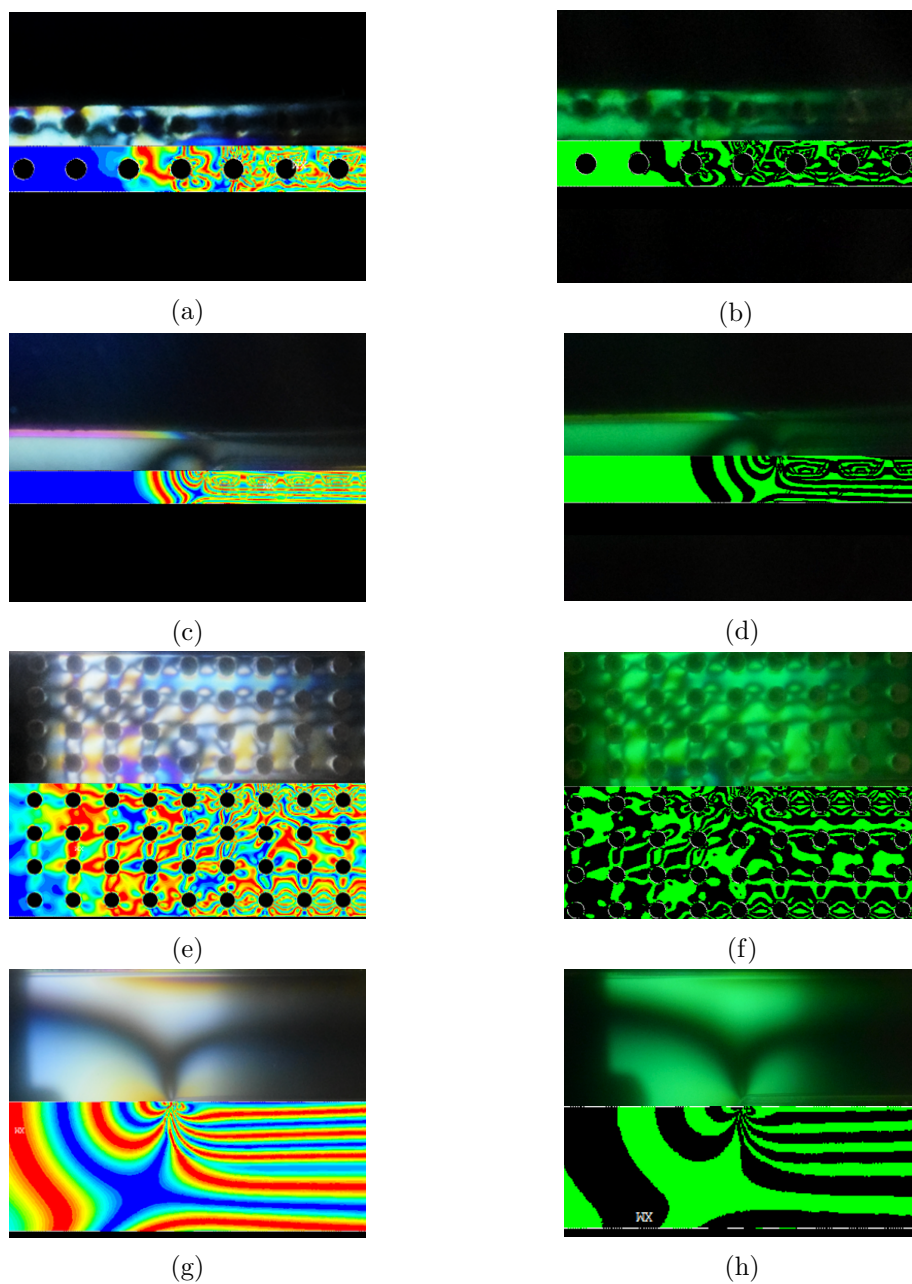


Figure 5.6: Isochromatic fringes in specimens during mode I loading. Left side: Fringe patterns (top) and respective FEA results (bottom). Right side: Dark field isochromatics (top) and respective FEA results (bottom). (a) & (b): Porous specimen with $N_{c_y}=1$, (c) & (d): Homogeneous specimen with $N_{c_y}=1$, (e) & (f): Porous specimen with $N_{c_y}=4$, (g) & (h): Homogeneous specimen with $N_{c_y}=4$

Quantitatively, testing revealed consistent behaviour between all specimens of different types, with minimal standard deviations (Figure 5.7), ensuring the repeatability of the presented results (the force displacement graphs for all tested specimens can be found in Appendix C.2). It is important to note that the experimental results only refer to one location of the crack tip with respect to the void. As described in the methodology section, the specimens were designed so that the crack tip location with respect to the voids is located below their centre (or $sx = 0.5$ as seen in Figure 3.6). However, due to manufacturing constraints, the total crack length had a variation of $0.5mm$, which, given the small size of each unit cell, results in crack tip locations in the range of approximately $sx = 0.4 - 0.65$.

Figures 5.7a, b, c show the numerically predicted variation of the normalised stress intensity within a unit cell estimated using both the projection method (dashed lines) and the BT expression (solid lines), plotted along with the results of the experiments (which were estimated as described in Subsection 3.1.2). The experimental data points are placed in the x axis at the approximate location where the crack tip was found to be located from the quality control procedure for each specimen size. For all different sizes and porosities, the experimental results are found to be in good agreement with the numerical results, especially those estimated using the BT expression in accordance to the experimental methodology.

Still, the numerical results estimated using the BT expression, slightly overestimate the experimental results. These deviations might be attributed to limitations during manufacturing. During the quality control of the specimen it was found that even though the topology of the voids was accurately manufactured, the voids' diameters exceeded the designed value by a factor of approximately 10% (i.e. $0.14mm$) which is attributed to laser stretching. Additionally, the circularity of the voids was found to deviate by an averaged factor of 0.15, while the average eccentricity of the voids was estimated to be 0.35. In the specimen with the $2mm$ void diameter, due to the close tolerances, the crack was sometimes found to be located slightly off from the mid-plane, which could give rise to mode II phenomena as well. As discussed in Section 5.1.1, the bluntness of the crack tip might also be the cause of deviations between the experimental (where the crack tip radius is finite) and numerical results (where the crack tip radius tends to zero), as the presence of a finite crack tip radius would more likely reduce the stress at the crack tip.

With the exception of the specimen with $N_{c_y} = 1$, the numerically predicted variation of the stress intensity estimated using the projection method around the void is limited (Figures 5.7a, b, c). On the contrary, the numerically predicted stress intensity estimated using the BT expression for each specimen size and porosity is almost

constant for all cases studied. At the same time, the crack tip for each manufactured specimen type might have minimal variations in its crack tip location s_x , as described previously. Therefore, in order to investigate the size effect, an averaged value of the numerical results, estimated using both methods, for $s_x = 0 - 0.75$ ($s_x = 1$ is excluded due to periodicity) is used as a baseline for the experimental results. The experimental results are compared to the averaged baselines in Figure 5.7d.

As expected, porous materials appear weaker than the homogeneous material ($SI_N = 1$ for all s_x values of the homogeneous case), with the stress intensity at the crack tip increasing for increasing porosity. Experimental findings also show a strong size effect, with smaller specimen exhibiting lower normalised stress concentration at the crack tip than their larger counterparts, which are then seemingly converging to a constant

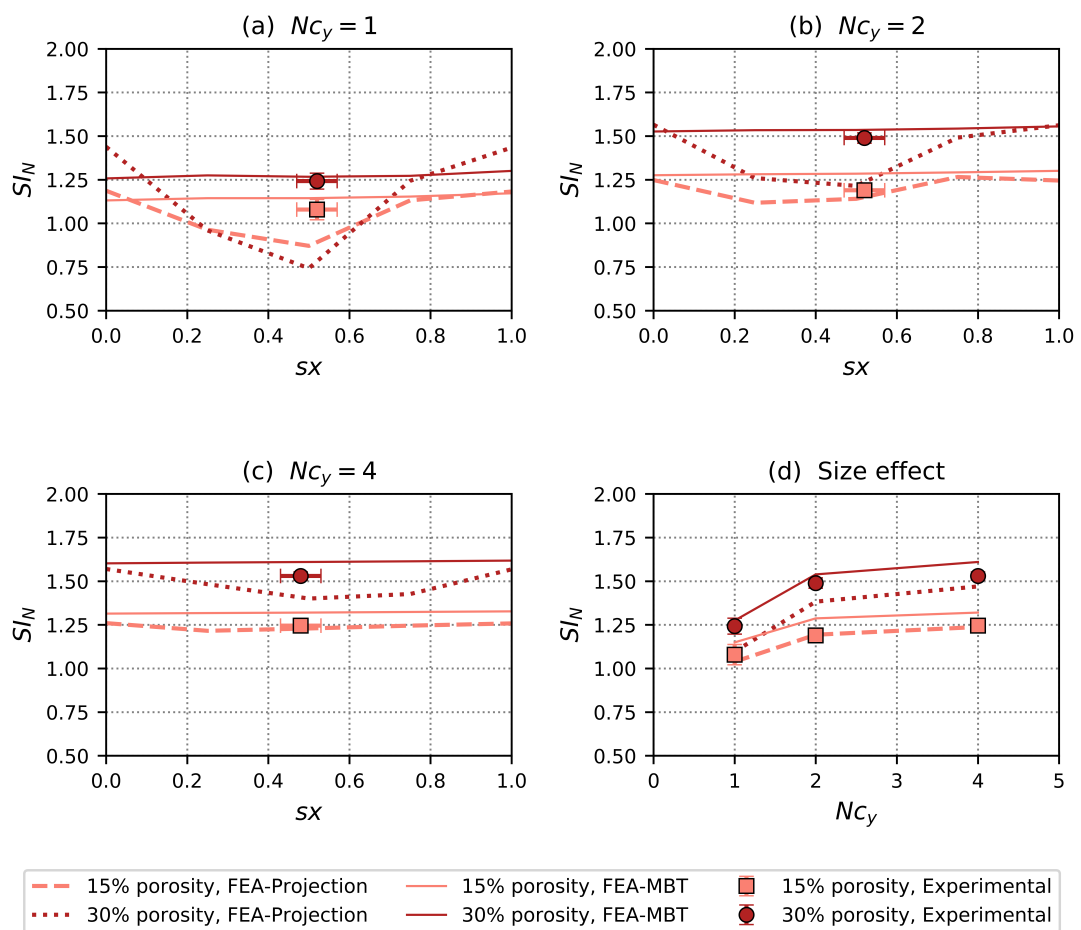


Figure 5.7: Numerical variation in SI_N within unit cell with experimental data points appended for each different size: (a) $N_{cy} = 1$, (b) $N_{cy} = 2$, (c) $N_{cy} = 4$. (d) Experimental size effect with numerical results averaged for s_x ($\overline{SI_N}$).

value for increasing size. This behaviour is consistent with the numerically predicted results for both, the exact representation of the tested specimens, and the idealised case presented in Chapter 4, where the voids were placed in a triangular array and the specimen's aspect ratio was large enough to assume the existence of a long crack.

In the previous chapter, this size effect was linked to the significance of the $A_{1/2}$ non-singular stresses, and an empirical model including the geometrical dependency coefficient, D_c , (where $D_c = 1/\sqrt{Nc_y P^3}$, see Equations 4.3 and 4.4) was derived to predict the stress intensity. The experimental results again appear to be strongly correlated with the parameter D_c (Figure 5.8). The experimental results validate the numerically observed trend, with specimens of lower D_c values, exhibiting a sharp increase in their stress intensity. Furthermore, specimens with $Nc_y = 1$ exhibit lower stress intensity values, that appear to comply with numerical results, which also predict a distinct curve for models with just one row of unit cells per specimen arm. Hence, the experimental results provide further evidence that the suggested geometrical coefficient D_c is linked with the stress intensity at the crack tip of a porous material.

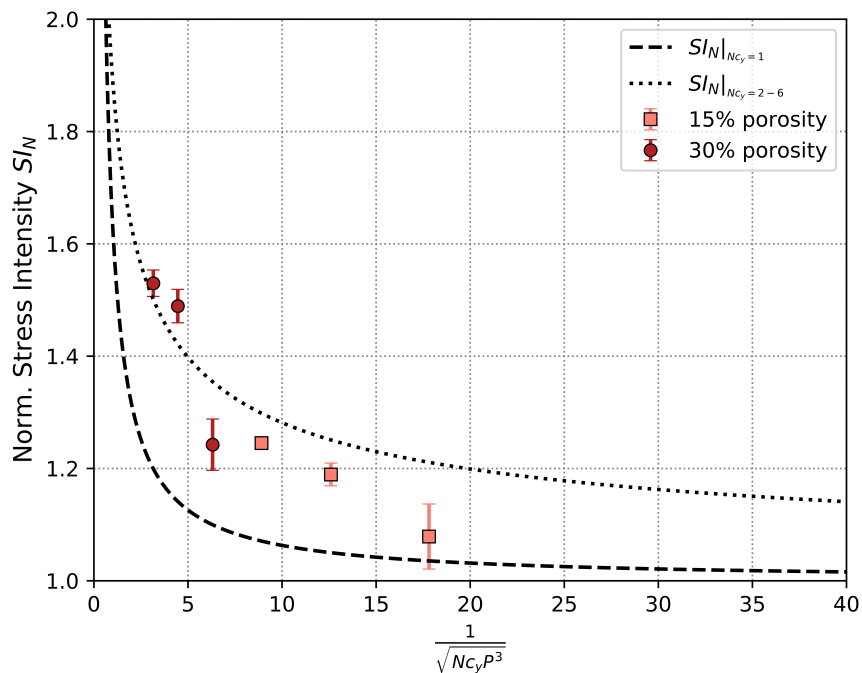


Figure 5.8: Comparison of experimental results with fitted model from Chapter 4. The numerical model for $SI_N|_{Nc_y=1}$ represents specimens with one row of per voids per specimen arm, while the one labelled $SI_N|_{Nc_y=2-6}$ represents larger specimens.

5.3 Effects of manufacturing inaccuracies on the stress intensity at the crack tip

The above experimental study validates the size effect and further supports the significance of non-singular stresses in specimens with arrays of voids. However, during manufacturing of such structures, the voids deviate from the ideally designed shape and can have different eccentricity or circularity values. In fact, porous materials occurring from more stochastic procedures than a pre-designed laser cutting (e.g. water blown free rise polyurethane foams) can have highly anisotropic void shapes. The ellipsoidal shape of the voids formed during foaming has been found to greatly influence the material's stiffness during various loading types like tensile [133, 134], compression [135, 136], and impact loading [137]. With respect to mode I fracture, the influence of void anisotropy has been investigated for ductile materials [138] and cases where the crack tip is located in the void, for infinite materials [74]. To the author's knowledge, the effect of the shape of a void in the near tip area on the stress intensity and the size of the K-dominance zone in brittle, finite size specimens, has not yet been addressed.

In order to investigate the impact of the voids' shape on the stress concentration at the crack tip, a parametric study was conducted. Models with elliptic voids (to account for differences in eccentricity) and square voids with rounded edges (to account for differences in circularity) were considered (Figure 5.9). The elliptic voids have a closer resemblance to the natural cell shape that is formed in free-rise foams as the gas trapped in the liquid foam rises to the surface before it solidifies. The shape anisotropy ratio, SR , of the elliptic voids is considered as the ratio of the void size in the x direction over the void size in the y direction. For this study two different shape anisotropy ratios were considered, one where the x -direction void size is double that of the y -direction ($SR = 2$, Figure 5.9a) and one where it is half of it ($SR = 0.5$, Figure 5.9b). Cases more

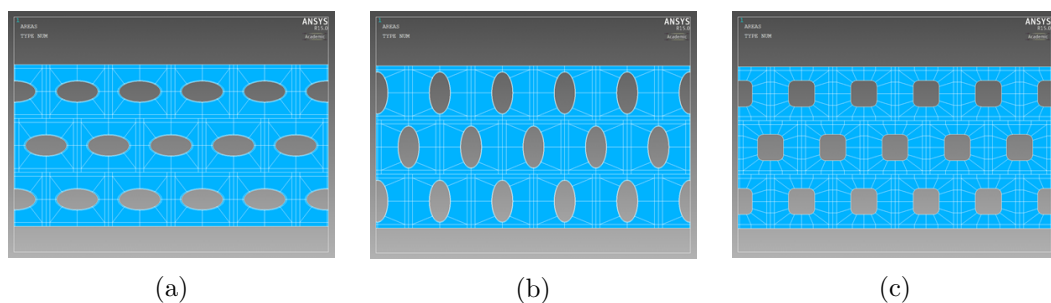


Figure 5.9: Models with different void shapes investigated in parametric analysis. (a) Voids elongated in x direction, OV , $SR = 2$, (b) voids elongated in y direction, OV , $SR = 0.5$, (c) voids with rounded rectangle shape, SQ

exaggerated than those that occurred from manufacturing inaccuracies were considered to highlight the differences.

For most cases, models of three porosities were created, approximating 5, 20 and 30%. Note that for the case of the elliptic voids elongated in the y -direction ($SR = 0.5$), the void diameter corresponding to 30% porosity intersected the unit cell's horizontal boundaries and thus was not considered. During this parametric study, the voids in all models are distributed in an equilateral triangle topology, to approximate isotropy, as previously described in Chapter 4.

Figure 5.10a plots the normalised stress intensity of all models against their size. Results show that the orientation of the elliptic voids significantly changes the material's behaviour. More specifically, when the voids major axis is parallel to the crack, the stress intensity at the crack tip diminishes, tending towards the behaviour of the homogeneous specimens and implying apparently tougher behaviour than their perfectly circular equivalent. On the contrary, when the void is rotated 90° so that the major axis of the void is perpendicular to the direction of the crack, the stress intensity at the crack tip rapidly increases. Models with rounded rectangle voids exhibited a very similar behaviour to the idealised case of circular voids, although for higher porosities the stress intensity at the crack tip was slightly diminished. Despite the large differences exhibited by the stress intensity, the size of the K-dominant zone remains almost constant for all cases (Figure 5.10b) and any variations in it are not enough to justify the large differences in the stress intensity estimation. Thus, non-singular effects might not be uniquely responsible for changes in the observed stress intensity at the crack tip.

Figure 5.11a plots the amplitude of the $A_{1/2}$ stresses, \tilde{C} , against the geometrical parameter $1/Nc_yP$, which was shown in the previous chapter (Equation 4.2) to uniquely describe the variation of $A_{1/2}$ stresses with the material's geometrical features. Indeed, even for the case of porous materials with different void shapes, the amplitude of $A_{1/2}$ stresses seems to agree with the value of the idealised case of circular voids, represented in Figure 5.11a by the black dotted lines. Different dotted lines represent different specimen sizes, though their exact labelling is not important in this case.

Conversely, when plotting the normalised stress intensity SI_N against the geometrical parameter $\sqrt{P/Nc_y}$ (Equation 4.1), multiplied by the normalised amplitude of $A_{1/2}$ stresses (Figure 5.11b), the parametric models deviate from the idealised case of circular voids (again, the black, dotted lines on the graph), forming distinct curves for each different void shape. Yet, the trends between these two plotted values remains the same, even if there is not a unique correlation for all material topologies.

This deviation from the idealised case is also reflected when plotting the results as a function of the geometrical parameter D_c (Figure 5.12). Even though the previously es-

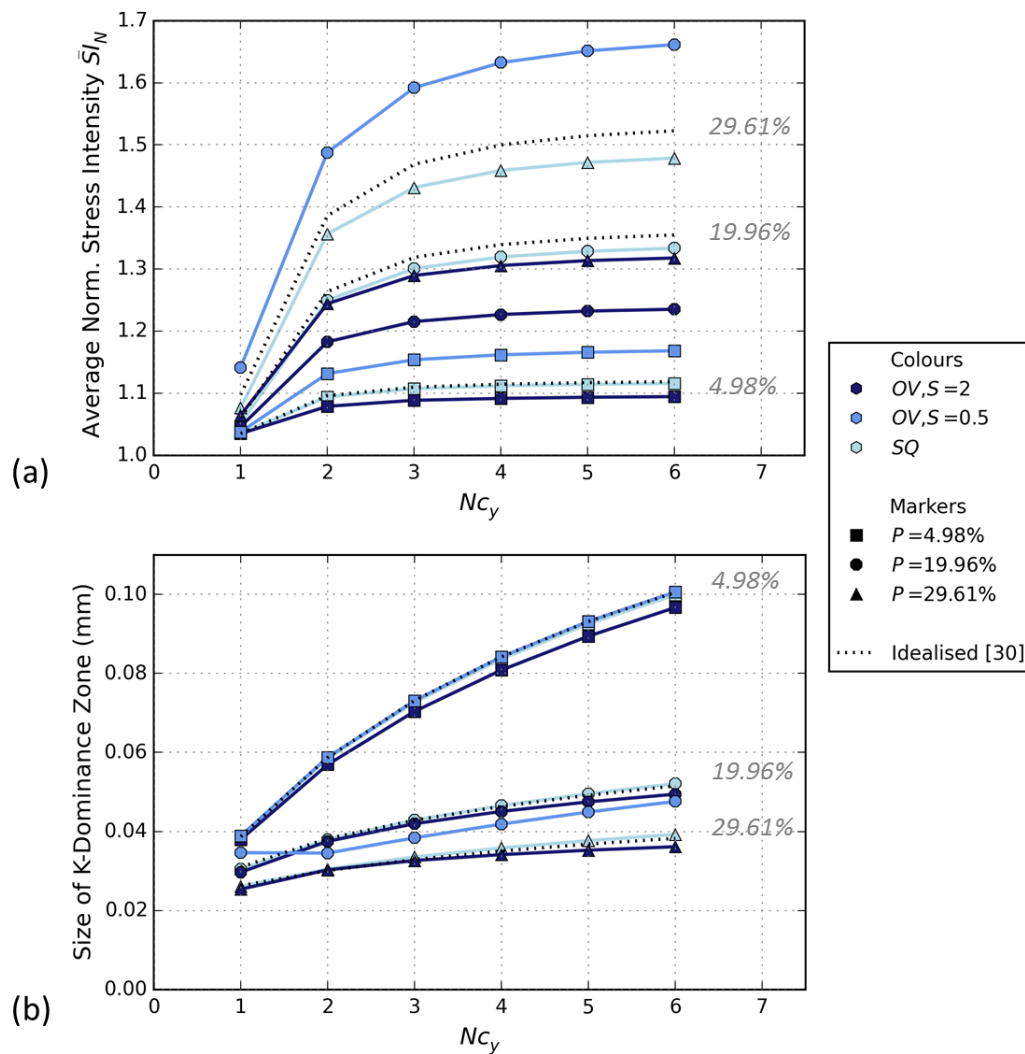


Figure 5.10: Influence of void shape on size effect of porous materials. Dotted lines represent the idealised case of a perfectly circular void, as presented in the previous chapter. (a) Normalised stress intensity at the crack tip for different void shapes, (b) Size of K-dominance zone versus the size of the specimen. The annotated percentages on both graphs refer to the idealised case.

timated empirical model (dotted lines) can provide an approximate, average estimation of the expected stress intensity for all different models, it is not an accurate representation. Nevertheless, each model of a different void shape follows a similar pattern, despite the difference in their exact values. This provides further evidence that the geometrical dependency coefficient D_c has a strong influence on the stress intensity at the crack tip of porous materials. The experimental results are also plotted on Figure 5.12 for comparison.

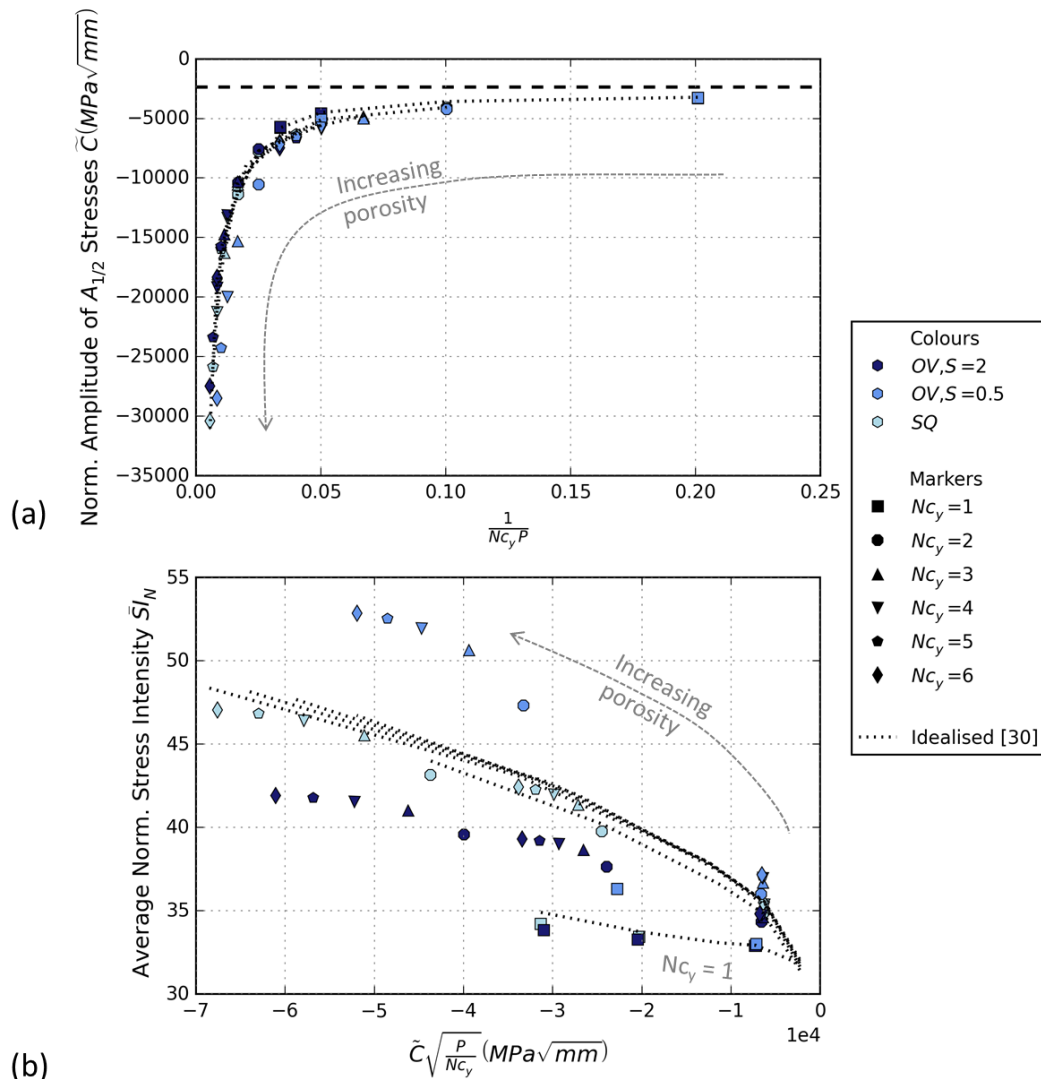


Figure 5.11: (a) Normalised amplitude of $A_{1/2}$ stresses versus the geometrical factor $1/Nc_y P$ that has been found to uniquely describe them for perfectly circular voids (dashed line represents the homogeneous case), (b) Average normalised stress intensity at the crack tip versus the amplitude of the $A_{1/2}$ stresses, multiplied by the geometrical factor $\sqrt{P/Nc_y}$

The presented results show that during mode I fracture, the void shape of porous materials significantly affects the stress at the crack-tip. While non-singular stresses, $A_{1/2}$, still appear to have a direct impact on the scaling of the normalised stress intensity for different sizes and porosity levels, the exact relationship linking them together might be more complicated than the one that was previously presented for the idealised case. This means that the relationship between the stress intensity at the crack tip and

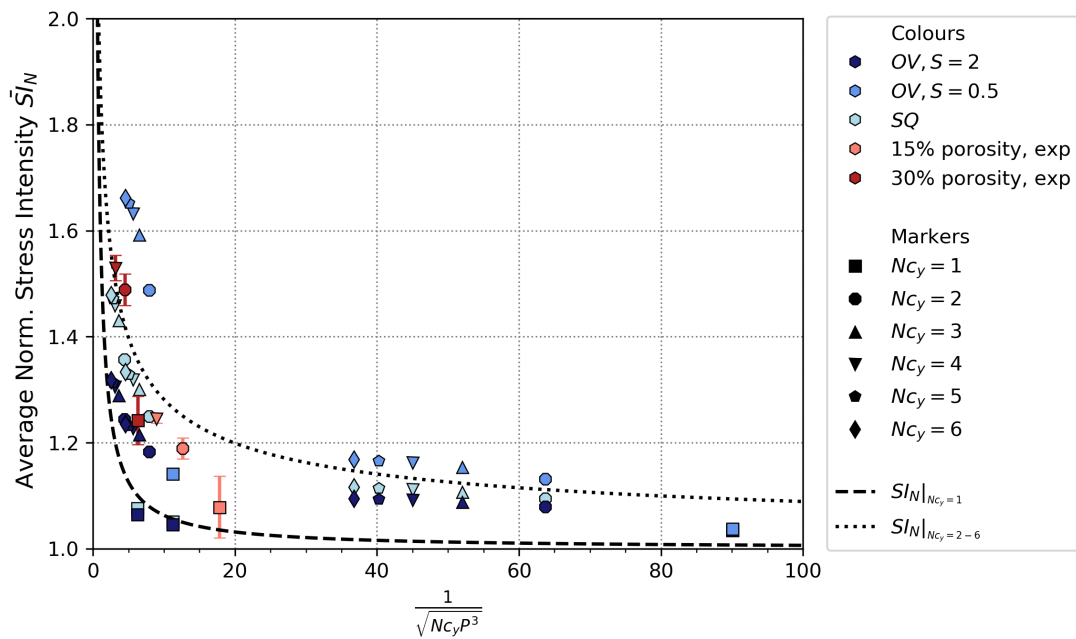


Figure 5.12: All parametric and experimental results against the empirical model of Equation 4.4. Although exact values may differ, the general trend can be captured by the geometrical dependency coefficient D_c for all cases.

the material's geometrical features may in fact be dependent on more factors than its porosity and number of voids in the y direction. An in-depth investigation should be performed, encompassing more parameters, in order to be able to achieve a better understanding of porous materials' behaviour and provide insight on how a material's mesostructure in the near-tip area can affect the material's properties.

5.4 Conclusions

This chapter experimentally validates the existence of a size-effect in brittle porous materials, which was first numerically predicted in the previous chapter. An attempt to address the significance of the non-singular $A_{1/2}$ stresses is also made. Finally, the effect of voids' shape on the measured properties is investigated numerically, in order to explain deviations between the experimental and numerical results. The key findings can be summarised as follows:

- Mode I experiments on DCB PMMA specimens were performed to validate the existence of a size effect in porous materials. Results showed that this size effect can indeed be experimentally observed and was found to follow the same trend

as the one predicted numerically. Small deviations between the numerical and experimental results can be attributed to manufacturing inaccuracies.

- Using photoelasticity, the near-tip stress field was observed during the experiments. Even though the results were only assessed qualitatively, the need to include more terms, apart from the singular one, in order to describe the stress field around a crack in the vicinity of a void was highlighted.
- In order to address the reported manufacturing inaccuracies, a numerical parametric analysis was conducted, investigating the influence of variations in the shape of the voids in the near-tip field. It was found that even though such variations can have a great influence on the exhibited stress at the crack tip, the amplitude of the $A_{1/2}$ stresses remain almost unaffected for all different void shapes studied.
- The geometrical dependency coefficient D_c has been found to be strongly correlated with the stress at the crack tip for both experimental and numerical parametric results. However, the empirical relationship predicted in Chapter 4 does not seem to be able to fully predict the normalised stress intensity for all cases. More parameters governing the mesostructure need to be investigated, which could also have a direct impact on material's behaviour in mode I loading, additional to the $A_{1/2}$ non-singular stress variations.

CHAPTER 6

In-depth investigation of the effect of porosity in applications of engineering interest

As it was discussed during the review of the literature (Chapter 2), there only exists a minimal amount of studies addressing the fracture behaviour of low to medium porosity materials. Yet, such materials are becoming increasingly common, especially with the rise of advanced manufacturing technologies like wire and arc manufacturing [25], selective laser melting [28] and other additive manufacturing technologies [27], which tend to create specimens with small levels of stochastically distributed, unwanted porosity. However, instead of viewing porosity as a negative feature, understanding the exact behaviour of a crack near a void can promote materials of new capabilities, including crack-arrest [34, 74] and controlled fracture [70, 71].

In the previous chapters, it was shown both experimentally and numerically, that brittle porous materials, of an ordered meso-structure can exhibit prominent size effects. Even though these size effects have been closely correlated to the increased significance of non-singular stresses in porous materials, there are indications that the mechanisms behind this size effect are more complicated.

This chapter focuses on more realistic materials and structures that can have an immediate engineering interest. Initially, porous materials of random microstructure are investigated to verify whether the size effect is still exhibited or whether it is concealed by their stochastic behaviour. An attempt is also made to correlate the exhibited stress intensity to their mesostructural features.

The next section of the chapter, takes a step back and focuses on the effect of isolated inhomogeneities (voids or inclusions) in the stress intensity at the crack tip in

order to provide insight into explaining patterns observed for the random materials. In previous research, it has been shown that even the presence of a single void or inclusion in the vicinity of a crack can change the local stress field [54, 56, 59]. Here, an in-depth designed numerical experiment is performed to map the relationship between the stress intensity and the mesostructural characteristics of each specimen. As an extension of this study, materials with stop-holes and stiff inclusions are also addressed. Finally, the interactions between multiple voids are investigated.

6.1 Stress intensity variations for porous materials with a random mesostructure

Porous materials, either naturally occurring or manufactured, are usually characterised by a stochastic distribution of their mesostructural features. This stochasticity is also reflected in their properties which, even if they exhibit a consistent average value, are usually also characterised by a statistical variation quantified by a standard deviation [13]. In the previous chapters, idealised porous materials were investigated in mode I fracture and found to be characterised by prominent size effects, with smaller specimens exhibiting apparently tougher behaviour than their larger counterparts. Nevertheless, it is yet unclear whether similar patterns would be found numerically for perfectly brittle but random materials, or if these are concealed by the stochasticity of their nature.

A numerical investigation into this was performed, using two-dimensional finite element models of DCB specimens created in ANSYS. Contrary to the previous chapters, the models were not created by arraying a single, identical unit cell. However, in order to ensure a constant and uniform cell density, the matrix material was divided into rectangular representative unit cells of dimensions $Size_x = 3.5\text{ mm}$ and $Size_y = \sqrt{3}Size_x/2 \approx 3\text{ mm}$ in the x - and y - direction respectively, as in the previous chapters. This ensured that the outer dimensions of all specimens throughout the thesis have consistent macroscopic dimensions, irrespectively of their mesostructural features.

Each unit cell then contained a single circular void positioned randomly around the cell's centroid, based on a pre-defined level of randomness, (R). This level of randomness was expressed both in the distribution of the void radius (R_d) as well as the deviation of the void's centroid from the centroid of the unit cell (R_{loc}) (Figure 6.1). For example, a model with 0% distribution in its void diameter and 0% distribution in its location would have voids of exactly the same size, each one located at the centroid of each unit cell, converging to the idealised case studied before. Three levels

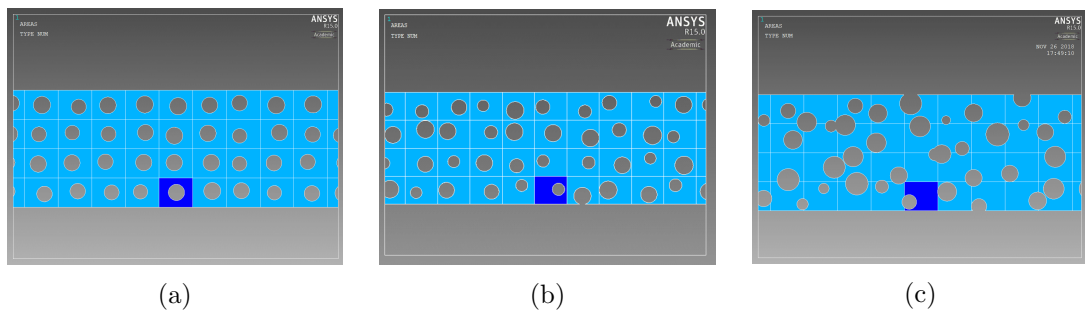


Figure 6.1: Models of $N_{c_y}=4$, $d_{av} = 1.64$ and different levels of randomness: (a) Small randomness, (b) Medium randomness, (c) Large randomness. The dark blue unit cell represents the unit cell on which the crack tip was located. Five different crack tip locations were assumed on that unit cell, from one end to the other at $Size_x/4$ increments. Note that voids were not allowed to intersect the bottom boundary of that unit cell.

of randomness were used for this study (Table 6.1), namely Low ($R_d = 10\%$, $R_{loc} = 25\%$, Figure 6.1a), Medium ($R_d = 25\%$, $R_{loc} = 50\%$, Figure 6.1b) and High ($R_d = 50\%$, $R_{loc} = 95\%$, Figure 6.1c). These randomness levels are used to estimate the upper and lower boundaries of either the location or the void diameter for each different type of model. The exact values characterizing each unit cell of these models were then randomly generated in ANSYS with a uniform distribution function.

Average void diameters (d_{av}) of $0.82mm$ and $1.64mm$ were considered, corresponding to average porosities of 5% and 20% respectively (Table 6.1). In order to investigate the size effect, models of different sizes were created by increasing the number of representative unit cells on each specimen arm in the y-direction, N_{c_y} . This study addresses sizes N_{c_y} in the range of 1 to 6 .

The models were meshed using the same element as in the previous chapters (8-node two-dimensional element ANSYS Plane 183), yet in this case the mesh was unstructured instead of mapped. The element size in the entirety of the model was $0.2mm$ (approximately the same as the far-field element used in the mapped meshes of the previous chapters), while, as before, in order to account for computational inaccura-

Table 6.1: Distribution values used for each randomness level and resulting porosities P for each different average void diameter

Randomness level (R)	R_d	R_{loc}	P, $d = 0.82mm$	P, $d = 1.64mm$
Small (S)	10%	25%	$5.01\% \pm 0.045\%$	$20.01\% \pm 0.21\%$
Medium (M)	25%	50%	$5.09\% \pm 0.1\%$	$20.42\% \pm 0.29\%$
Large (L)	50%	95%	$5.27\% \pm 0.37\%$	$20.13\% \pm 0.76\%$

cies near the crack tip singularity, the mesh was locally refined with $0.0025mm$ sized elements in the near-tip area ($25x$ smaller than the near-tip element in the mapped meshes of the previous chapters).

As before, only half of each specimen was modelled and appropriate boundary conditions were set. Although this may limit the concept of "randomness", since the mesostructure of the material equilaterally of the crack is by definition perfectly symmetrical, it was important for the scope of this study that mode I loading conditions are maintained. Each specimen was then loaded as described in previous chapters (for more details see Subsection 3.2.1) and the same material parameters were applied. For each different case (defined as a combination of a void diameter d , size Nc_y , and level of Randomness R) five specimens of differing topologies, all generated randomly, were considered in order to ensure repeatability.

Note that even though for large levels of randomness the voids did sometimes intersect the boundaries of the specimen, this was not allowed for the unit cell on which the crack tip was located, whose lower boundary was always intact (dark blue unit cell in Figure 6.1). Despite the fact that the void's location is expected to vary the estimated local stress intensity factor, as before, five measurements were assumed for each different model, with the crack tip ranging from one end of the unit cell to the other, at $Size_x/4$ increments. This was done in order to ensure that different crack tip locations relative to the void location are considered for all models, especially the ones with a small randomness level where the void location was always very close to the centroid of the unit cell. The results that follow present both, the stress intensity independently for each of the five different crack tip locations of each specimen (SI_N), and the averaged stress intensity of all 5 different crack tip locations resulting in a single average stress intensity for each specimen ($\overline{SI_N}$).

Results show that the variation of the averaged stress intensity at the crack tip, $\overline{SI_N}$, followed the expected pattern, with specimens of higher porosity generally exhibiting higher stress intensity at the crack tip than specimens of lower porosity (Figure 6.2a). Due to the stochastic nature of the specimens, there were deviations from the idealised behaviour, especially prevalent in specimens with a larger randomness level. Models of small and medium randomness level also exhibit a size effect, consistent with the trends of the idealised case for an averaged value throughout the unit cell, albeit a statistical variation from the idealised value is clearly existent. However, as the level of randomness increases, the stress intensity at the crack tip presents greater irregularities and deviations from the median, making the size effect indiscernible.

Previous research has attributed the variations on the stress intensity of brittle materials on the loss of K-dominance and the increased significance of non-singular

stresses [113, 139]. This trend has also been found in the previous chapters of this thesis. Plotting the independent stress values for each crack tip location (SI_N) for all specimens against the respective value of the amplitude of non-singular stresses, it seems that they are correlated with an almost monotonic pattern (Figure 6.2c). More specifically, higher values of the non-singular component of the total stress at the crack tip, C , generally mean higher values of the total stress at the crack tip, SI_N .

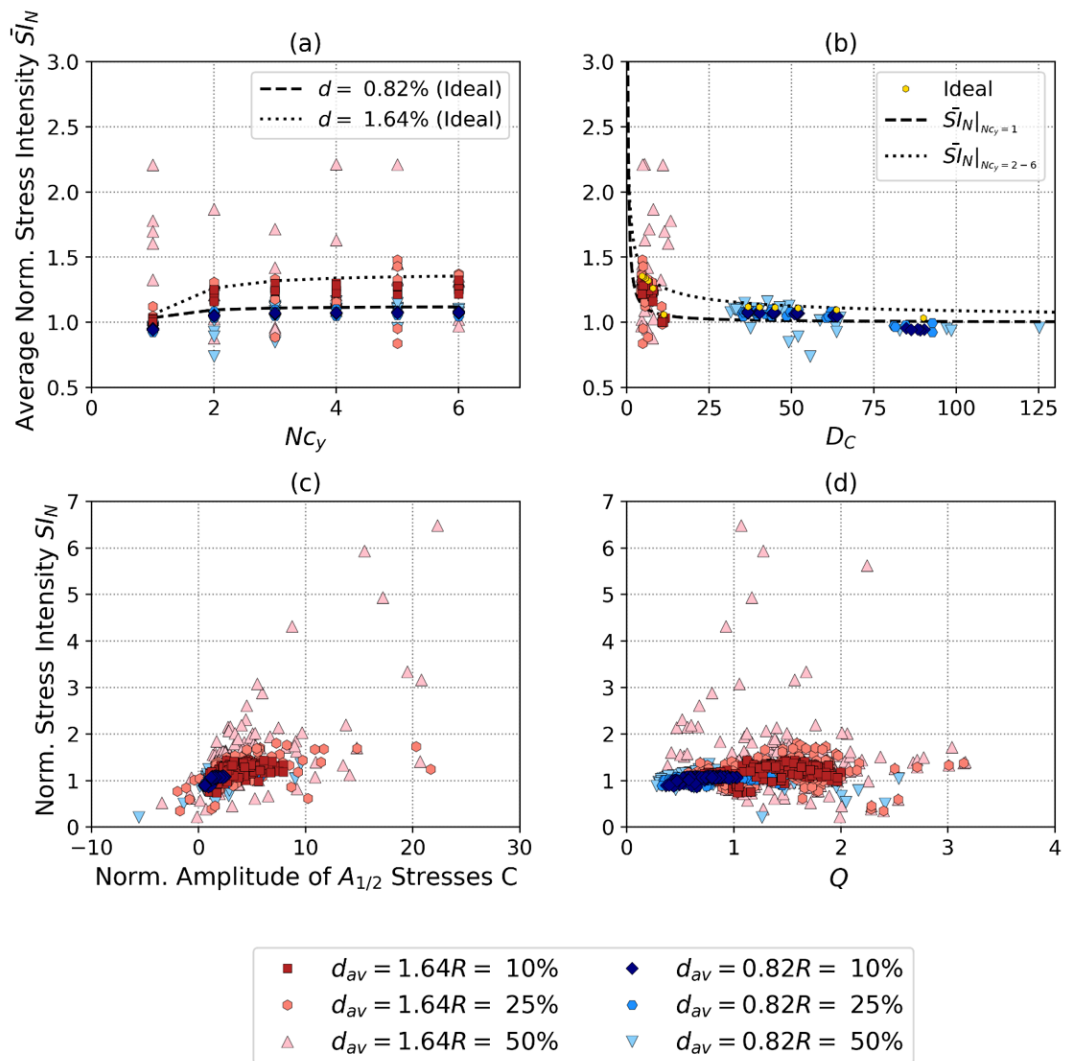


Figure 6.2: Results for random models. Top row: Normalised stress intensity results, averaged for all 5 locations in the unit cell where the crack tip was assumed, plotted against (a) specimen size, and (b) the value D_c , related to the material's mesostructure. $\bar{SI}_N|_{Nc_y=1}$ refers to models with $Nc_y = 1$ and $\bar{SI}_N|_{Nc_y=2-6}$ refers to models with $Nc_y = 2 - 6$. Bottom row: Individual values of normalised stress intensity plotted against (c) the normalised amplitude of the $A_{1/2}$ non-singular stresses, and (d) the value Q .

In Chapter 4, an empirical formula was suggested (Equation 4.4) based on the parameter D_c (Equation 4.3), which takes into account the porosity P of the material, and the number of unit cells in the y-direction of each specimen arm, Nc_y . Figure 6.2b plots the averaged FEA stress intensity results (again, averaged for all 5 locations within a unit cell for each specimen) for the random specimens against these predictive models. The empirical model provides adequate upper and lower boundaries for the variation of \overline{SI}_N , however, again, for models of larger porosity and randomness level, and smaller D_c values, there were noticeable deviations from the predicted values.

The strength of specimens of infinite dimensions reinforced with inclusions has been previously found to be more strongly affected by the near-tip area [140, 141] (even though the far-field heterogeneities are reported to additionally affect to some extent the stress intensity at the crack tip by modifying the materials elastic properties [140]). In order to evaluate whether it is in fact the near-tip area that is mainly responsible for the variations presented in the current results, the magnitude of SI_N is plotted against the sum over all voids of the inverse distance of the center of each void from the crack tip multiplied by its diameter (Figure 6.2d):

$$Q = \sum_{n=1}^n \frac{d_n}{r_n} \quad (6.1)$$

, where n is the total number of voids of the specimen, d_n is the void diameter of each void and r_n is the distance of each void from the crack tip.

The way that Q is calculated (Equation 6.1) decreases the weight of very small voids or voids located at large distances from the crack tip, on its estimated value. Figure 6.2d shows a clear correlation between the estimated moment and the normalised stress intensity at the crack tip, implying that the normalised stress intensity is mainly influenced by the mesostructure of the near-tip area. However, again, great deviations for specimens with larger randomness levels can be observed. These deviations may be attributed to boundary layer effects, either on the surface of the crack, near the crack tip, or on the upper boundary layer, compromising the specimen's integrity.

In order to obtain a more complete picture of the influence of porosity on finite specimens, in the following sections the behaviour of brittle porous materials is dissected into different components, which are investigated separately.

6.2 Influence of near-tip isolated heterogeneities in the stress intensity ahead of a crack

In order to precisely identify how the stress intensity at the crack is influenced by the existence of heterogeneities in the near-tip region, the simple case of a specimen with a single void in the vicinity of the crack tip is studied. A mixed level full factorial designed experiment (DOE) was used to identify statistically significant patterns, while minimizing the required resources.

Models of different sizes were created, corresponding to 1, 2, 4, 6 and 50 representative unit cells in the y -direction, N_{c_y} (as defined in the previous section and shown here in Figure 6.3). The latter size is simulating the case of infinite materials, since for the void dimensions selected, the size of the inhomogeneity is insignificant compared to the total specimen dimensions. The void's location was controlled by the angle and the distance of the centroid of the void relative to the crack tip (Figure 6.3). The same void diameters as in the random simulations were used to assess the effect of void size. All factors and levels of the designed experiment are shown in Table 6.2. As in section 6.1, element Plane 183 was used to mesh the model with a near-tip size of $0.0025mm$. The specimens were then loaded as described in the previous section.

Table 6.2: Factors and levels used in DOE

Factor Name	Levels								
Angle θ ($^\circ$)	0	45	90	135	180				
Distance r (mm)	1*	1.5	2	2.5	3	3.5	4	4.5	
Size N_{c_y}	1	2	4	6	50				
Void diameter d (mm)	0.82	1.64							

* For a distance $r = 1$ and void diameter $d = 1.64$, the placement of the void at angles $\theta = 45^\circ$ and 135° was not considered because the void intersected the surface. Instead, the results presented below for these models are estimated as an interpolation.

Figure 6.4 plots the influence of a void in the near-tip area on the stress at the crack tip, depending on its location for different sized models¹. Note that the colours on the contour plots represent the variations on the stress intensity when a void is placed on the respective angle and distance from the crack tip, and do not refer to a continuous stress field around the crack tip. For the seemingly infinite case (Figure 6.4e), the stress variation is clearly divided in two regions; voids placed in front of the

¹All contour plots in this chapter refer to specimens with $d_{av} = 1.64mm$. The ones for $d_{av} = 0.82mm$ are not presented here since they are very similar, but they can be found in Appendix D.1

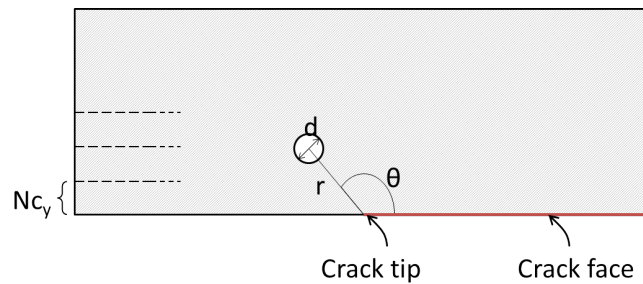


Figure 6.3: Illustration of factors used for DOE.

crack tip (left side of plot, angles $\theta = 135^\circ$ and 180°), which amplify the stress intensity at the crack tip, and voids behind the crack tip (right side of plot, angles $\theta = 45^\circ$ and 0°), whose presence shields the crack tip and lowers its stress intensity. This pattern of stress variations is consistent with that found for a single void or compliant inclusion in line with the path of the crack in infinite specimens [54, 56, 142, 143] (which would be relevant to the results for angles $\theta = 0^\circ$ and 180° as defined in the present study). However, as the specimens become smaller this pattern of variation starts changing form, with the zone shielding the crack tip moving to the left, right above the crack tip for specimens with N_{c_y} equal to 1 and 2 (Figure 6.4a and b respectively).

For all models, it can be observed that after exceeding a certain distance from the crack tip the presence of the void is no longer significant and does not have an effect on the stress intensity at the crack tip. This behaviour is observed even in models with $N_{c_y} = 1$ for larger distances in angles θ equal to 0° and 180° , even though they are not plotted here (larger distances are not feasible for other angles in the smallest specimen). However, in specimens with N_{c_y} in the range of 1 to 6, as the void approaches the upper boundary of the specimen, a new increase in the stress intensity at the crack tip is observed, even though the void may well be outside the near-tip area. Figure 6.4 (f) plots the stress intensity for all specimens, when the void is located at an angle $\theta = 90^\circ$ and its center is coincident with the specimen's upper surface. This behaviour gets less pronounced as the void's diameter becomes negligible compared to the specimen's dimensions, and vanishes for the seemingly infinite case of $N_{c_y} = 50$. The presence of boundary voids has been found to change the bending stiffness of small scale specimens in previous research [78]. A specimen's behaviour in mode I fracture can be attributed partly to the near-tip stress field and partly to the bending stiffness exhibited by each specimen arm. During 3-point bending simulations of high porosity specimens, it was found that the stress localizes in areas closest to the top and bottom surface of the specimen, forming a 'hinge' around which the specimen rotates [80]. Similarly, here the existence of a discontinuity on the upper layer of the material, which carries a major

component of the stress in bending, compromises its stiffness, leading to an apparently more compliant material and a subsequent rise in the stress intensity at the crack tip.

In previous research, when examining a single inclusion in the path of the crack, it was found that as the crack approached the discontinuity, the stress singularity was

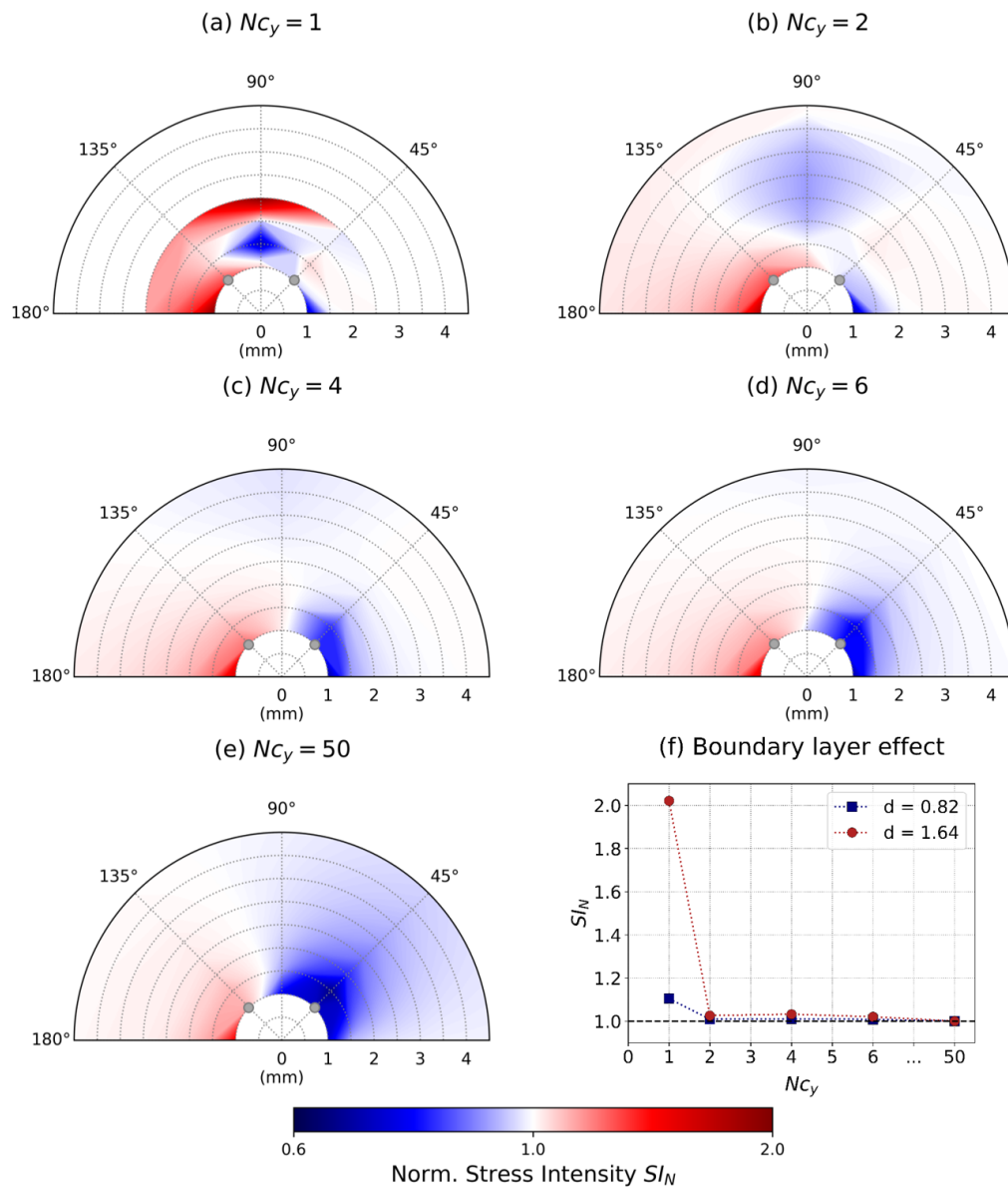


Figure 6.4: Contour plots representing the influence of a void with $d_{av} = 1.64\text{mm}$ in the near-tip area on the stress intensity at the crack tip for different sizes of specimens (a)-(e). For a distance $r = 1\text{mm}$, angles $\theta = 45^\circ$ and 135° are not considered. Plot (f) shows how a void near the boundary layer (at $\theta = 90^\circ$) affects the stress intensity at the crack tip.

no longer a function of $1/r^{1/2}$, as would be the case under the assumption of a large K-dominant zone [53, 59]. In fact, in Chapter 4 the presence of voids in the near-tip area was found to shrink the size of the K-dominant zone, making the $A_{1/2}$ non-singular stresses significant, and thus producing such variations in the stress intensity observed at the crack tip. Similar shielding and amplification patterns around a single void in infinite specimens have also been linked with analytically estimated variations of the constant non-singular term, the T-stress [60]. For the present study, the variation patterns of the normalised size of the K-dominant zone and the normalised amplitude of non-singular stress $A_{1/2}$ (C) are shown indicatively for sizes $N_{c_y}=1, 4$ and 50 in the left and right column of Figure 6.5 respectively.

Indeed, it appears that the presence of a void in the near-tip area can significantly shrink the size of the K-dominant zone for the majority of locations that it could assume (Figure 6.5, left column). Interestingly, there appear to be certain locations in the near-tip area where the presence of a void would not influence the size of the K-dominant zone. For smaller specimen these 'neutral' locations are located at angles 0° and 180° , however larger specimens exhibit a different pattern. In the seemingly infinite specimens voids on the extension of the crack tip ($\theta = 180^\circ$) have a strong influence on the size of the K-dominant zone, while voids located along 45° no longer compromise the K-dominance after they exceed a certain distance.

In contrast, the amplitude of non-singular stresses $A_{1/2}$ (C), is not as sensitive to the presence of voids in the near-tip area. More specifically, even though (C) is mainly reduced for the smallest specimens, as the specimens get larger a reduction of its magnitude only appears for a small area right above the crack tip (blue area in right column graphs of 6.5). The value C for any location outside this small area seems to converge to a near zero value (pink areas in right column graphs of 6.5). Note that the value of C for the homogeneous case -which was used for the normalisation- is negative when interpreting the results.

It is clear that all DOE factors (Table 6.2) affect the values of the estimated normalised stress intensity (SI_N), normalised amplitude of non-singular stress $A_{1/2}$ (C) and the normalised size of the K-dominant zone. The magnitude of influence of each design parameter on the estimated values can be identified from a pareto chart of effects (Figure 6.6).

The three graphs in the top row of Figure 6.6a show the effects of each design level on the material's fracture properties, when considering all specimens sizes. Results showed that the effect of the specimen's size is only averagely significant when considering the stress intensity (Figure 6.6a, left) and has a low to minimal effect on both the normalised amplitude of the non-singular stresses (Figure 6.6a, center) and the normalised size of

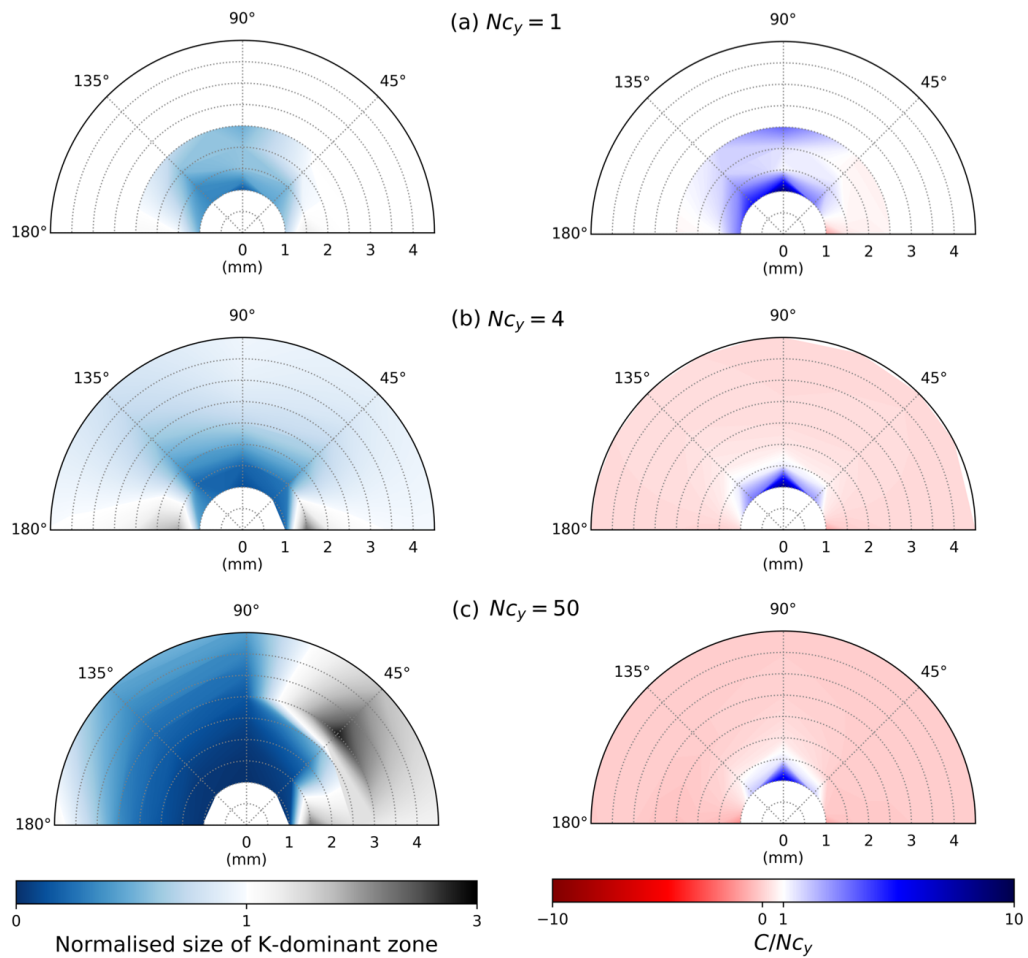


Figure 6.5: Contour plots to show the variations of fracture parameters for different locations of the near-tip void (here shown are the results for voids with $d_{av} = 1.64\text{mm}$) and different size specimens. Left graphs: Variations on normalised size of K-dominant zone. Only values smaller than the homogeneous case are considered significant due to the risk of losing K-dominance. Right graphs: Variations on the normalised amplitude of non-singular stresses C . Please note that the value of C for the homogeneous case is negative and thus the colourbar of the right column graphs in Figure 6.5 is reversed so that values higher than that of the homogeneous case are depicted in red and lower than that in blue. The values have been additionally divided by N_{c_y} so that they can be comparable with a common colourbar.

the K-dominant zone (Figure 6.6a, right). The increased size effect on SI_N is attributed to the influence of the boundary layer, as described earlier. Still, the angle θ of the void's location relative to the crack tip appears to be the most significant parameter on influencing all of the studied fracture properties of a brittle material. These findings explain the variations seen in Section 6.1, where a size effect was not clearly identifiable

and large variations in the stress intensity could be found even for larger specimens, in a seemingly random fashion, possibly attributed to the existence of voids of varying angle near the crack tip. However, for the cases where the voids were placed in a periodic array (Chapter 4), implying that the angle θ was consistent for different specimens, this size effect was much more prominent.

When the size effects are removed (bottom row of graph 6.6b, where only specimens of $N_{c_y}=50$ are considered), the angle θ is still the most influential DOE factor on all three fracture parameters of the material. Interestingly, it is found that the void's diameter is the least significant, far less than both indicators of the void's location (angle and distance from crack tip). This implies that a specimen's stress intensity and K-dominance can be affected by the existence of a heterogeneity in the near-tip area, regardless of its size.

So far, this study has highlighted the ways in which each of the material's mesostructural parameters affects its fracture properties and K-dominance. However, in the previous chapters it was reported that it is in fact the loss of K-dominance and the rising importance of non-singular stresses that are the underlying causes of the variations in

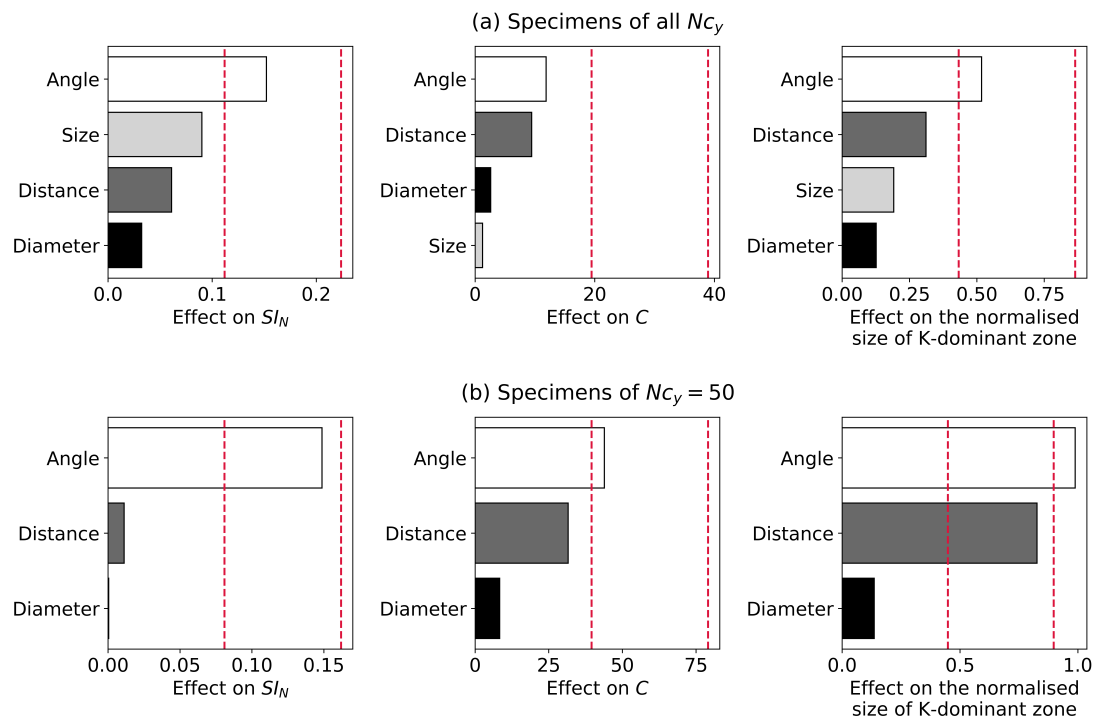


Figure 6.6: Pareto chart of effects for all DOE factors against the studied fracture parameters. The red dotted reference lines indicate statistical significance based on Lenth's pseudo standard error.

stress intensity.

Plotting the variations between the material's fracture properties with each other, some interesting observations emerge. Firstly, it appears that the amplitude of the $A_{1/2}$ -stress is uniquely correlated with the size of the K-dominant zone for all specimen sizes (Figure 6.7, left column). As expected, when the size of the K-dominant zone is small, the non-singular stresses exhibit high variations and are no longer negligible compared to the singular term. Yet, as the size of the K-dominant zone increases and K becomes the dominant parameter, non-singular stresses converge to the value of the homogeneous case.

A similar pattern can be seen when plotting the size of the K-dominant zone against the normalised stress intensity (Figure 6.7, center column). For seemingly infinite specimens, SI_N only presents large variations from the homogeneous value when the size of the K-dominant zone is considerably small. This finding confirms the hypothesis that in brittle materials it is the loss of K-dominance which causes variations in the estimated stress intensity. Any small variations in the values of the stress intensity for values of the K-dominance larger than the homogeneous case and for angles $\theta = 45^\circ$ and 0° could imply that there may be additional factors to be further investigated in the case where the void is behind the crack tip (e.g. a shielding effect may be in part attributable to energy dissipation from the void's deformation). As the size of the specimen gets smaller though, the variations in SI_N become independent from the size of the K-dominant zone. For the smallest specimen size the relationship between the size of the K-dominant zone and SI_N becomes even more unpredictable and does not seem to follow a specific pattern. Again, this is attributed to bending components due to the boundary layer, which as seen before (Figure 6.4e) is stronger for the smallest specimens.

Similar results were presented in the case of the idealised porous materials (Chapter 4), where larger specimens were characterised by an almost unique relationship between the size of the K-dominant zone and the estimated stress intensity, while smaller specimens presented a more complicated picture. Still though, in all cases, smaller sizes of the K-dominant zone were linked to higher variations of the stress intensity.

It is clear that both the stress intensity and the amplitude of the non-singular stresses vary under the condition that the size of the K-dominant zone is large enough. However, the relationship between the two is not linear (6.7, right column). Actually, for specimens where $Nc_y = 50$, SI_N and C are correlated with each other by a different linear expression for each angle θ of the void, giving a star-like pattern for the full range of angles studied here. Again, as the size of the specimen gets smaller and size effects become important this correlation becomes less prevalent. In fact, as the specimen size

becomes smaller, the pattern exhibited approaches the monotonic pattern also observed for random specimens, whose N_{c_y} values ranged from 1-6 (Figure 6.2c).

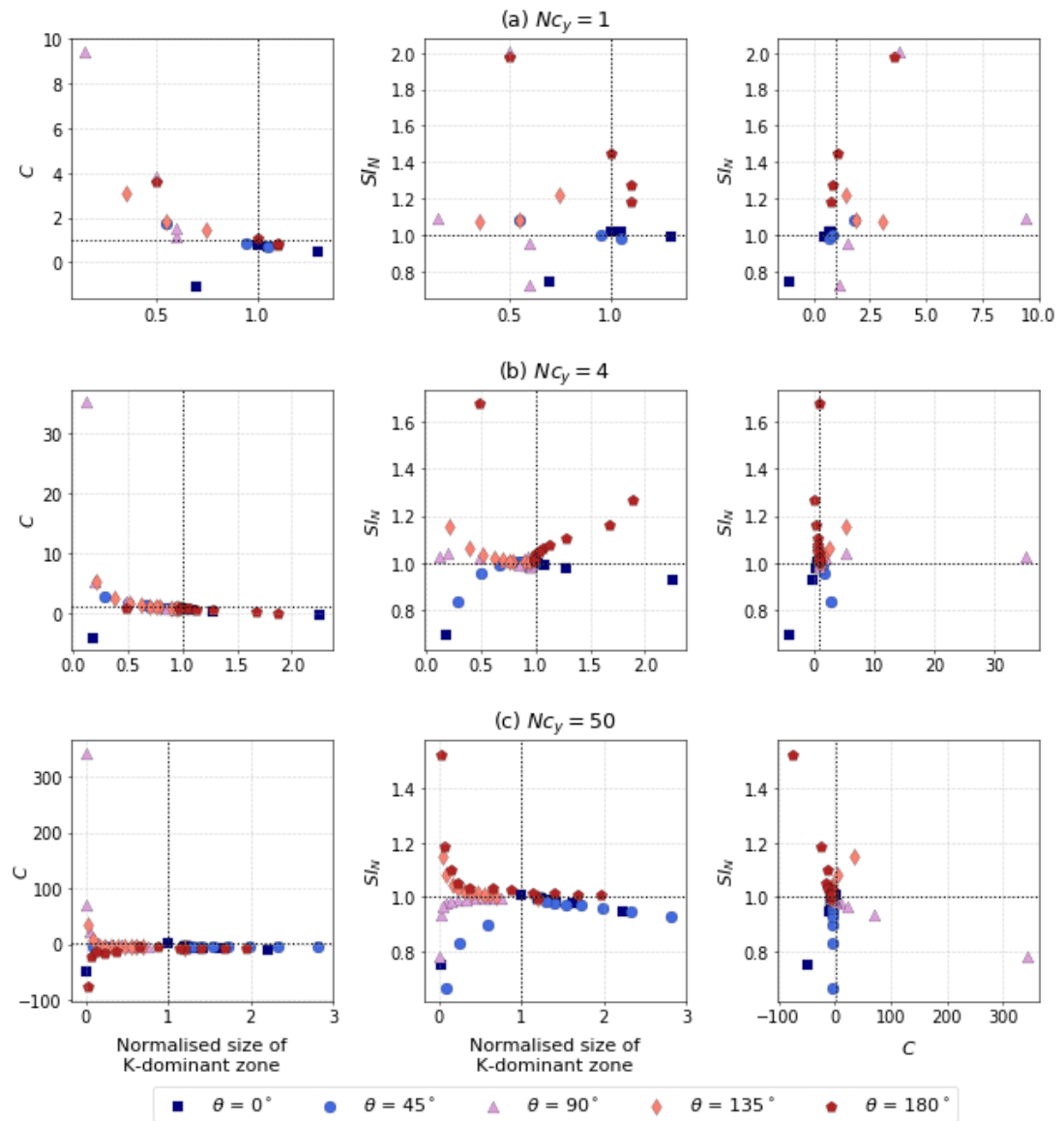


Figure 6.7: Relationship between material's fracture parameters for different specimen sizes. Left column: C -Normalised size of K-dominance zone, central column: S_{I_N} -Normalised size of K-dominance zone, right column: C - S_{I_N} . The black dotted lines are located at 1, representing the value of the homogeneous case.

6.2.1 Size effect in the design of stop-holes for finite size specimens

The limiting case for a void angle $\theta = 0^\circ$ is the practical case of the stop-hole, where the crack tip is located at the centre of the void (distance $r = 0$). It is well known [34, 70, 74] that voids can act as crack-stoppers by capturing cracks and delaying their propagation. When a crack tip is located inside a void, its radius becomes the crack tip's radius, which decreases the stress intensity compared to cases with a sharp crack tip. This implies that as the radius of the void tends to infinity, the stress at the crack tip tends to zero.

However, in the case of finite specimens, larger voids may result in an increase in the stress intensity at the crack tip if the void becomes large enough to compromise the specimen's bending stiffness. This antagonistic effect highlights the need to find a balance between the specimen's and the void's size. To investigate this, models of $Nc_y = 1, 2, 4, 6$ and 50 were created with stop-holes of sizes in the range of $d = 0.1, 0.82, 1.64$ and 2.46.

Results show that in all cases stop-holes reduce the stress at the crack tip (Figure 6.8). This is consistent with previous research and the results presented in section 6.2, as an extension of the case where $\theta = 0$. As expected [62], higher void diameters result in lower stress intensities at the crack tip. Interestingly, for specimens with $Nc_y = 1$ the stop-holes seem to be even more effective in lowering the stress, increasing slightly for larger specimens. This could be attributed to the ratio of the void's radius to the total specimen size: larger ratio would mean a greater percentage of the specimen's actual thickness, meaning a more effective contribution of the stop-hole. However, this effect

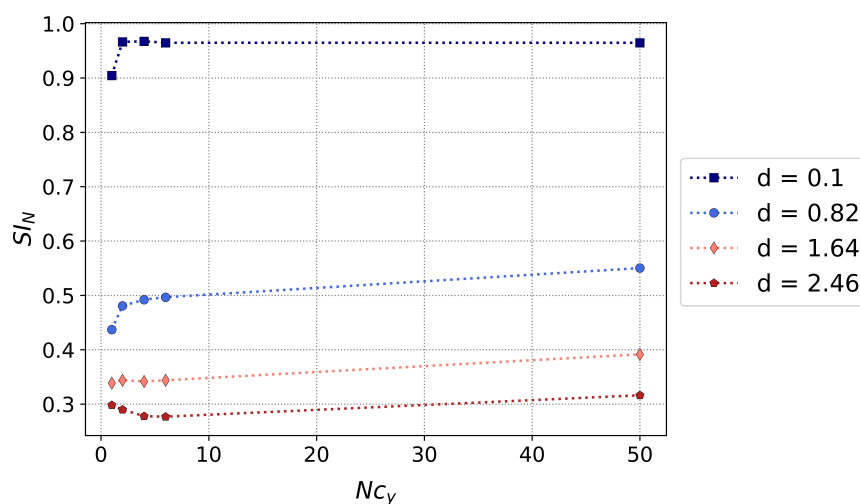


Figure 6.8: Effect of stop-holes of different radii on finite size specimens

gets inverted as the void's diameter is increased and approaches half of the specimen's total thickness, in which case boundary effects become distinguishable and the smallest specimen then produce higher stress intensities than their larger counterparts.

6.2.2 Influence of stress intensity on crack by single stiff inclusion instead of void

In the previous sections, it was argued that the existence of a void in the near-tip area impedes the K-dominant zone and causes it to shrink in size, giving rise to variations in the total observed stress intensity at the crack-tip. This section attempts to draw parallels between the case of a porous material (theoretically containing inclusions of a modulus $E=0$) and materials with inclusions of non-zero moduli. Specifically, the case of stiff inclusions is assumed, with the modulus of the inclusion E_I being 100 times higher than the modulus of the matrix material E_m . Such models can simulate composite materials or materials with impurities. For simplicity, the same Poisson ratio was assumed for both materials. The DOE factors and near-tip mesh parameters are the same as in section 6.2. However, this model covers a larger area and thus small changes in the mesh expansion have been performed that could give small numerical deviations.

Figure 6.9a shows the main effects plot for the stress intensity (i.e. averaged stress intensity) for each different specimen size with the distance from the crack tip. Materials with stiff inclusions exhibited a contrasting behaviour to that of the porous materials, that nevertheless again converges for larger specimens. It is interesting to note that even the boundary layer effect is reversed, with near-boundary inclusions lowering the stress intensity at the crack tip for smaller specimens (this can be observed more clearly for larger distances in the case of specimens with $N_{c_y} = 1$ and 2, which diverge from the otherwise converging pattern). Note that the variations in SI_N are less pronounced than those of porous materials. This is attributed to the fact that the porous material has an "inclusion" of zero modulus that can only be contrasted with the case of a stiff inclusion of infinite modulus. Since this is not feasible and a much smaller, finite value was used, the estimated patterns in the models with stiff inclusions are less prominent.

This reversed pattern in the averaged values of SI_N is similarly reflected for the stress variations in the near-tip area (Figure 6.9b), which is still divided into distinct zones, but of contrasting nature to that of the porous materials. More specifically, in contrast to materials with voids, the existence of a stiff inclusion in front of the crack tip (angles $\theta = 180^\circ$ and 135°) shields it from stress, while inclusions behind the crack tip (angles $\theta = 0^\circ$ and 45°) amplify the stress intensity on it. This behaviour is consistent with that found in previous research for a stiff inclusion located in line with the crack

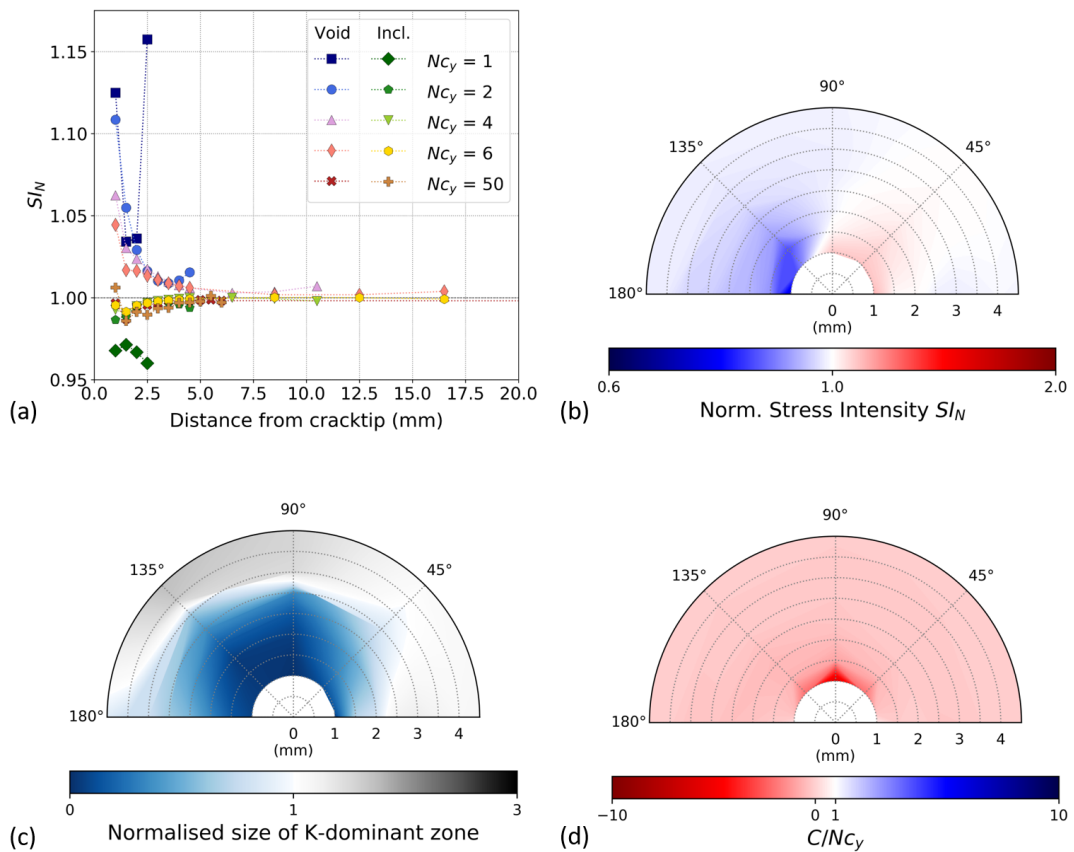


Figure 6.9: Results for specimens of $N_{Cy} = 50$, containing a single stiff inclusion in the near-tip area (graphs for the rest of the specimens sizes can be found in Appendix D.2). (a) Main effects plot comparing the variations of the stress intensity with distance for models with a single void (left side markers on legend) and stiff inclusion (right side markers on legend) in the near tip area. (b) Contour plot of the stress intensity variations for different locations of the inclusion (compare with 6.4e), (c) Contour plot of the variations on the size of the K-dominant zone for different locations of the inclusion (compare with the left graph of 6.5c), (d) Contour plot of the variations on the non-singular stresses for different locations of the inclusion (compare with the right graph of 6.5c)

(angles $\theta = 0^\circ$ and 180°) [54, 56]. Similarly, the amplitude of non-singular stresses also exhibits this inverted behaviour (Figure 6.9d), with a sharp increase on its magnitude for voids located right above the crack tip.

Despite this contrasting nature of the observed stresses at the crack tip, the void's influence pattern on the normalised size of the K-dominant zone remains very similar to that for the porous materials (FIG. 6.9c). This implies that in brittle materials, the loss of K-dominance due to a heterogeneity is consistent, regardless of the heterogeneity's

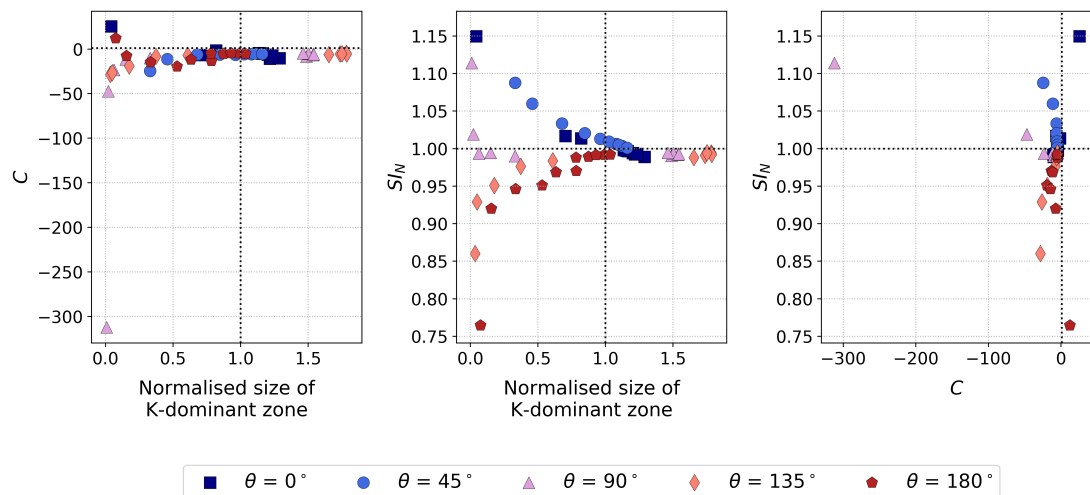


Figure 6.10: Relationship of fracture parameters for models with a single stiff inclusion

modulus. In fact, plotting both, the total stress intensity at the crack tip SI_N , and its non-singular component C , as a function of the normalised size of the K-dominant zone (Figure 6.10 left and center graph respectively, compare with Figure 6.7), it is observed that, again, large variations in their magnitude are closely correlated with the material's loss of K-dominance (the case of $N_{c_y} = 50$ is shown in order to avoid interference from boundary effects). In fact, the stress' non-singular component is still uniquely correlated with the total stress intensity at the crack tip (right graph of Figure 6.10), producing a star-like pattern as in Figure 6.7, although the values are again reversed.

6.3 Influence of two neighboring near-tip isolated heterogeneities in the stress intensity ahead of a crack

In porous materials, depending on their cell density, multiple voids may be present in the near-tip area. Previous studies have shown that the presence of heterogeneity clusters in the near-tip area has a more pronounced effect on the stress intensity, compared to a single heterogeneity, which is however subject to the location of the crack relative to the cluster [53, 54, 144]. In fact, when two voids are in close proximity, the width of the ligament created between them is additionally cited as an important parameter that may affect the stress field around the voids [54, 62, 145].

In this section, this synergistic effect is further examined and its impact on the non-singular component of the stress is also investigated. To achieve this, an additional void (void B) was placed in the vicinity of the first void (void A) in a combination of different

distances and angles relative to the crack tip. The following distance pairings and all possible angle combinations (θ_B for void B and θ_A for void A) between them were considered: a) both voids at $dist = 2.5mm$, b) void A at $dist_A = 1.5mm$ and void B at $dist_B = 3.5mm$, c) void A at $dist_A = 1.5mm$ and void B at $dist_B = 4.5mm$. For the above distances the voids can be placed in all possible combinations without overlapping. Only models with 50 rows of representative unit cells were considered in order to isolate the variations caused by void interactions from the additional noise resulting from the influence of the boundary layer.

The top row of Figure 6.11 plots the estimated values that originate from the mathematical addition or superposition of the variations that would be the result of each

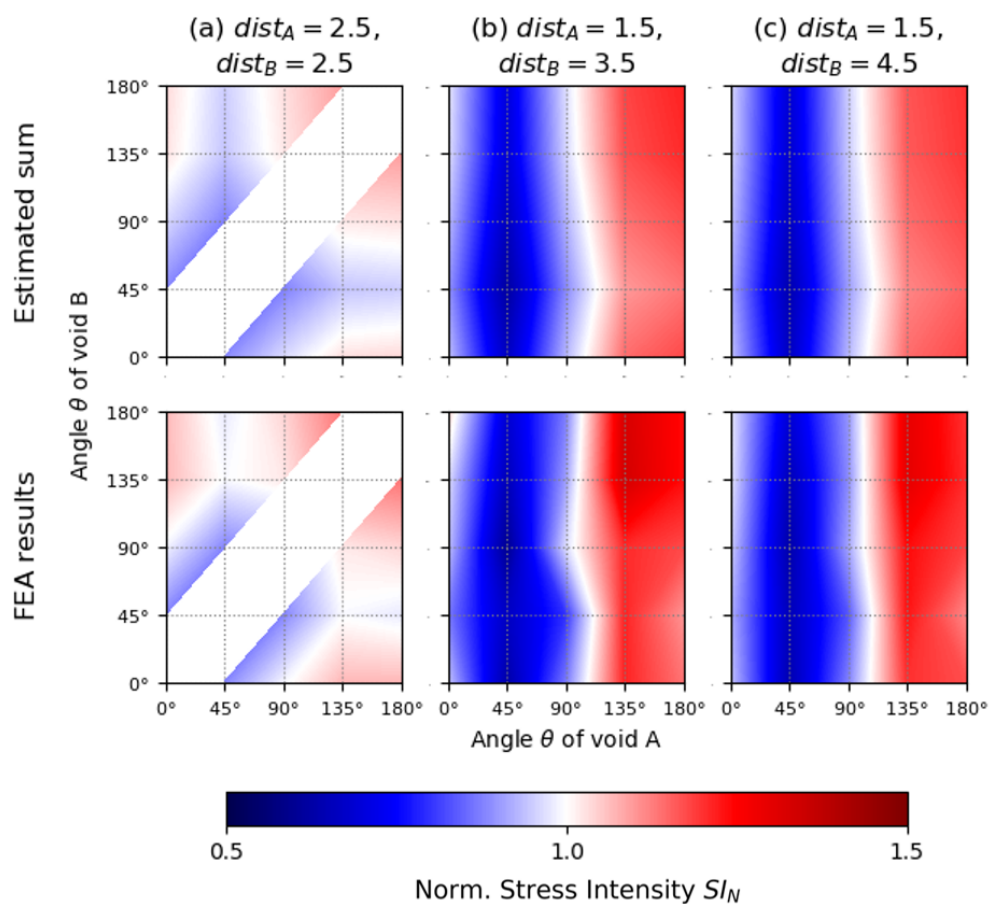


Figure 6.11: Variations of SI_N for models of different distance combinations between neighbouring voids. Top row: SI_N is estimated as the sum of the stress intensity variations that result from each single void independently. Bottom row: FEA results when both voids are modelled.

of the two voids being independently present at their given location. The actual FEA results of the behaviour for the models with the two neighboring voids are then plotted below them (bottom row of Figure 6.11). In all different distance combinations, simply adding the effect of the independent void values seems to approximate quite accurately the actual material behaviour as found by the FEA. However, small synergistic effects are observed that either enhance or attenuate the intensity of the stress at the crack tip.

As expected, in the cases where one void is closer to the crack tip, the stress intensity map is divided in two regions, showing an increase in SI_N for angle θ_A larger than 90° and a decrease for smaller values. This pattern is consistent with the behaviour of a single void in the near-tip area, implying that the void closer to the crack tip is dominant and becomes the main driver of the material's behaviour. As void B gets further away from the crack tip, this behaviour becomes even more prominent, and a smoothing of the two areas is observed, resulting in almost two equal halves.

Figure 6.12 plots the fracture parameters for the models with two neighbouring voids. Again, the loss of K-dominance seems to be a detrimental factor in the variations of the total stress intensity at the crack tip (central graph) and its singular component (left graph), with values converging to the homogeneous case as the size of the K-dominant zone converges to that of the homogeneous case. Note that for the models studied in this section at least one of the voids is always located in very close proximity to the crack-tip and hence the size of the K-dominant zone is always smaller than that

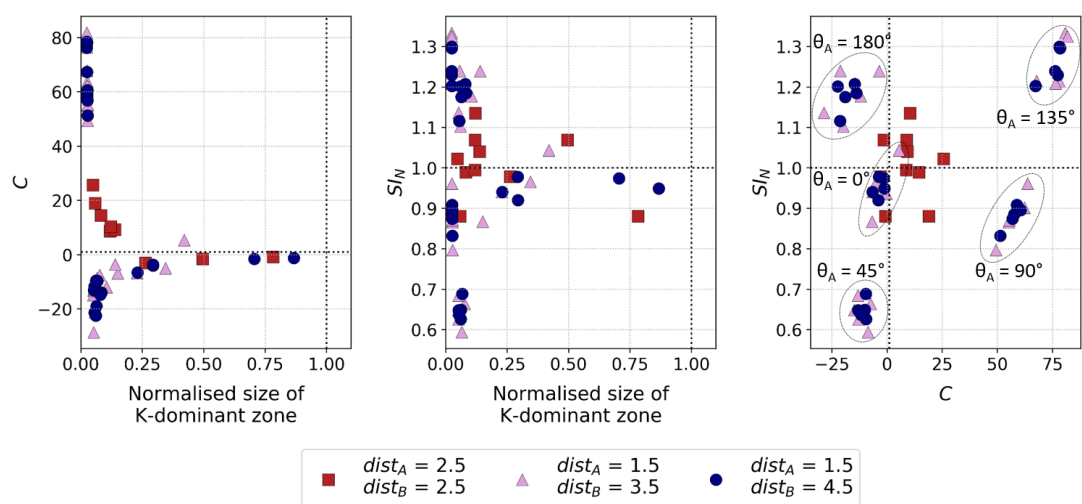


Figure 6.12: Relationship of fracture parameters for models with two neighbouring voids. The bubbles refer only to models when one void (void A) is closer to the crack tip and becomes the behaviour's driver.

of the homogeneous case.

Plotting the total stress intensity at the crack tip, SI_N , against its singular component SI_C , (right graph of Figure 6.12) it can be observed that the patterns are not as clearly monotonic as in the case of a single void. When one of the voids is closer to the crack tip, the general tendency of the results tends to agree with that of a single void, which in this case is the driving void (the one closer to the crack tip). However, for each angle θ_A the data points are scattered around a small area, which becomes smaller as the second void (void B) gets further away from the crack tip. This highlights the rise of additional parameters when two voids are in close proximity that needs to be further investigated.

6.4 Conclusions

The presented work investigates the existence of size effects in engineering materials and traces correlations between the material's mesostructure and their exhibited stress intensity at the crack tip, by identifying the contribution of non-singular components on that behaviour. This chapter provides a more in-depth investigation of the previously reported results, while attempting to remain relevant to applications of engineering interest. In general, the following conclusions can be made:

- Random materials of different levels of randomness and void diameters were investigated to establish whether they exhibit size effects consistent with predictions for idealised materials. Results showed that in general, the previously reported models provide reasonable approximations of the stress intensity in random materials. However, for large levels of randomness, large deviations were presented, which could be attributed to voids intersecting the top surface of the specimen's arm, thus compromising its bending stiffness. Further analysis indicated that the variations in the total stress intensity at the crack may partly be attributed to variations in the non-singular component of the stress. Moreover, it was observed that the mesostructure of the material in the near-tip area has a weighted influence on the material's exhibited behaviour, compared to the material's far-field properties.
- Consequently, the influence of a single void in the near-tip area on a specimen's stress intensity was investigated through a designed numerical experiment. The void's location, and particularly its angle relevant to the crack tip, was found to have a detrimental effect on the resulting stress intensity, either shielding or amplifying it. In fact, it was revealed that it is the shrinkage of the K-dominant

zone and the increased significance of the non-singular stress component that is most strongly correlated with these variations in the measured stress intensity.

- As a limiting case of a near-tip void, size effects in materials with stop-holes were also briefly investigated. Results showed that, generally, larger radii translate to a lower stress at the crack tip, which is consistent with findings for stop-holes in infinite materials. However, a prominent size effect was also observed, dependent on the ratio of the void's diameter to the specimen's arm thickness. More specifically, while the void remains small compared to the specimen's size, larger radii translate to a more efficient stress shielding. Yet, when the void's diameter surpasses a certain threshold (approximately 50% of the specimen's arm thickness), this behaviour is reversed and larger radii result in higher stresses at the crack tip in comparison to larger specimen of the same void radius.
- The above designed experiment for a single void in the near-tip area was repeated for the case of a single inclusion of higher modulus than the matrix. Results showed that the presence of the heterogeneity was still causing the K-dominant zone to shrink in the same way, regardless of the heterogeneity's modulus. However, the non-singular component of the stresses exhibited an inverted behaviour. Thus, the results showed consistent patterns with those of the porous materials, however the shielding and amplification areas were inverted.
- Finally, a second void was placed in the near-tip area to investigate the interactions between neighboring voids. Results showed that while some synergistic effects may be present, the total exhibited stress intensity can be adequately approximated by a simple sum of the stress intensities of each independent void. Consequently, when one void is located closer to the crack tip, this void is the main driver of the specimen's behaviour. Again, the loss of K-dominance is still found to be significant in the variations of the total and non-singular stress intensity at the crack tip. However, additional parameters are found to gain significance that need to be investigated further.

CHAPTER 7

Conclusions and future work

Porous materials are ubiquitous in nature, where materials are characterised by intricate mesostructures, offering them interesting properties. An interesting example is bones, a material that evolved to achieve, among other properties, low weight with high torsional and bending stiffness. In an attempt to mimic such properties in engineering, porous materials are becoming increasingly popular, from lightweight sandwich panels and shock-absorbing structures in the aerospace and automotive industries to thermal insulation layers.

In most cases, porosity is viewed as a means to reduce weight, increase the absorbed energy during impact or reduce the conducted heat or electric charge. However, when found in otherwise non-porous materials, voids are usually seen as defects, which compromise the strength of materials and structures. With the rise of additive manufacturing technologies the inclusion of even a low percentage of porosity on the newly manufactured components, is highly likely. At the same time, such technologies allow for the manufacturing of smaller, more delicate geometries and mesostructures, which deviate from the so far accepted failure theories.

Yet, a review of the literature showed that there is only limited research on the fracture properties of low to medium porosity materials, and size effects are mainly considered for non-brittle materials. This thesis attempts to address this gap by a campaign of both FEA simulations and experiments to investigate the relationship between a specimen's mesoscopic and macroscopic geometry and its resulting fracture properties. The main conclusion of the presented work is that the use of a single parameter, as described by LEFM, to describe the stress intensity of porous materials

is inadequate, even in the case of low porosity, brittle materials. In fact, prominent size effects were observed both numerically and experimentally and the effect of the presence of voids on the near-tip stress field was validated by means of photoelasticity. The behaviour of porous materials was then dissected into the following two components:

- The near-tip component, which was the main focus of this study:
 - The existence of a heterogeneity in the vicinity of a crack can substantially shrink the size of the K-dominant zone, thus increasing the significance of the non-singular stress components. This is subsequently translated to a difference in the observed stress intensity at the crack tip. In fact, when the effect of the boundary layer is insignificant, the largest stress intensity variations observed are related to the smallest K-dominance zones.
 - The effect of a near-tip heterogeneity on all the parameters studied here (the crack-tip stress intensity, the size of the K-dominant zone and the amplitude of the $A_{1/2}$ non-singular stresses), is predominantly affected by the relative angle at which the heterogeneity is located. The distance between the void and the crack tip is also, naturally, an important parameter, since as the distance increases, the heterogeneity is removed from the near-tip area. Notably, the void diameter, even though it affects the intensity of the observed patterns, is not as significant as other parameters.
 - More specifically, a void located in the near-tip area, will generally increase the average estimated stress intensity, implying an apparently weaker material. However, if the void is placed in front of the crack tip (between the crack tip and the loading point), it can shield the crack tip from the stress and stiffen the material. On the contrary, a void located behind the crack tip will amplify the stress on the crack tip. When more than one voids are located in the near-tip area, their effect is approximately additive, at least for the cases considered here.
 - Contrarily, when a stiff inclusion is located in the near-tip region it will lower the average stress intensity, thus implying an apparently tougher material. Again, the relative angle between the inclusion and the crack tip is significant and the relationship between the angle and the stress intensity is opposite to that of the voids: crack shielding is achieved by placing a stiff inclusion behind the crack tip, while stress amplification occurs when placing a stiff inclusion ahead of the crack tip.
- The effect of the boundary layer/specimen size:

- In finite size specimens the effect of the boundary layer is becoming increasingly significant. The effect of this layer is thought to be attributed to the compromise of the bending stiffness of the specimen.
- Idealised porous materials, as studied in Chapter 4, are characterised by prominent size effects. As the distribution of the voids becomes more random (i.e. the material becomes less idealised) this size effect is increasingly concealed by the stochasticity of the estimated results.

This thesis has made contributions towards the better understanding of the effects of porosity in brittle materials. The results drew tangents to potential applications of designed material mesostructures aiming to achieve tailored behaviour in specimens of “infinite” or “finite” size. This can be of value during the optimisation of materials, so that porosity may no longer be viewed as a defect, but rather as a means for damage tolerant design, offering novel materials with enhanced capabilities of controlled cracking and crack-arrest. However, the findings presented here are still in their infancy. In fact, the findings of this thesis are considered to be at a Technology Readiness Level 2-3 (the basic idea and concept have been developed and some initial experimental proof of concept has been performed). A significant amount of both experimental and computational work is still required to advance from a theoretical framework to practical solutions. The major concrete steps required are:

- The results of this study, showed that the relative angle between the heterogeneity and the crack tip is a deciding factor of whether the heterogeneity will amplify or shield the crack tip. Even though substantial evidence showed that this is linked to the increased significance of the non-singular stresses, the reason for the varying relationship between the amplitude of the non-singular stresses and the normalised stress intensity is not yet clear. This should be further investigated to obtain a more complete understanding of this phenomenon, and potentially a unique relationship between the singular and non-singular stresses.
- Even though it is clear that the boundary layers of finite size specimens can significantly weaken a specimen when disrupted, not enough data were collected to quantify this phenomenon. Ideally, in order to increase the accuracy of predictions of the stress intensity in finite size, porous specimens, a constitutive model should be created, combining the behaviour of both, the boundary layer and the near-tip component.
- In this study, only the case of a pure mode I loading was considered. However, in real-life porous materials, the porosity equilaterally of the crack may not be

symmetric, which would introduce mode II components. This should be studied if a more complete model is to be proposed. The presence of a mode II component, while the size of the K-dominant zone is shrunk, will potentially introduce the need to study the effect of the T-stresses as well.

- The present study focuses only on the linear accumulation of stress on a sharp crack tip, prior to fracture and observes a prominent size effect. However, it is not yet clear how that size effect would translate for the critical stress intensity factor of porous materials, which is a value of high importance for practical applications. Subsequently, after crack propagation is initiated, the behaviour of the crack front in specimens of different sizes would be of interest for applications of controlled fracture.
- In this study, only DCB specimens are investigated and the porosity of the material is considered to be the only characteristic size of the study. It would be of interest to study cases where a specimen, manufactured of a porous material, possesses a characteristic length of its own (e.g. specimen with holes for fittings of a diameter d_1 made of a porous material with a void diameter $d_2 \ll d_1$), to examine whether and how this dual level of heterogeneity would interact.
- Finally, an important next step would be to conduct case studies and initiate a strategic experimental campaign to demonstrate the potential of tailoring a material's mesostructure for damage tolerant design.

To summarise, the research described in this thesis has introduced theoretical and practical concepts that should be useful in the design and understanding of novel means of tailored strength. Although further research and development will be necessary before these ideas can be exploited in practical applications, the potential benefits are believed to be significant.

APPENDIX A

Clevis drawing

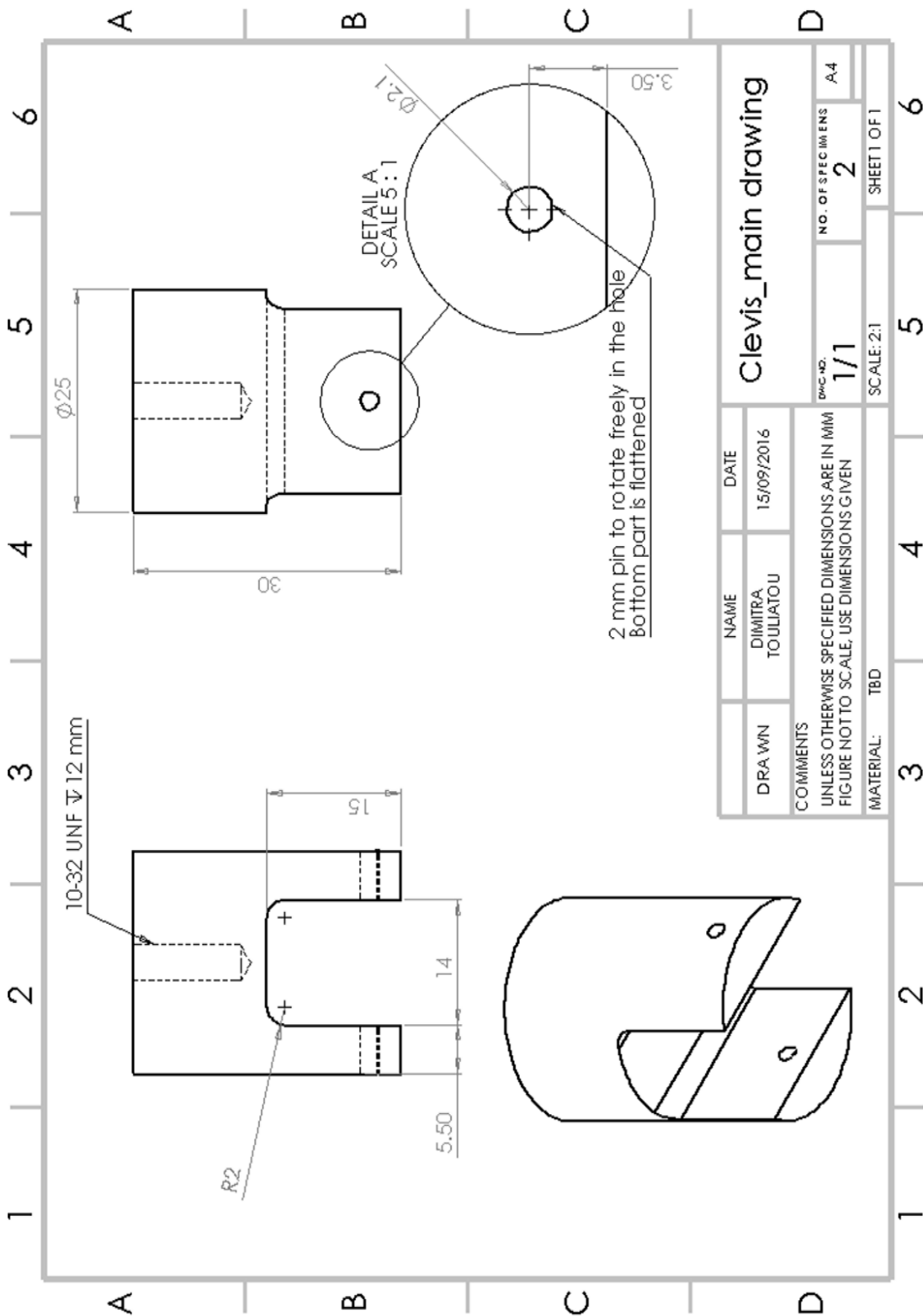


Figure A.1: Drawing of manufactured clevis

APPENDIX B

Supplementary material for Chapter 4

B.1 Additional plots for the mesoscopic behaviour of idealised materials

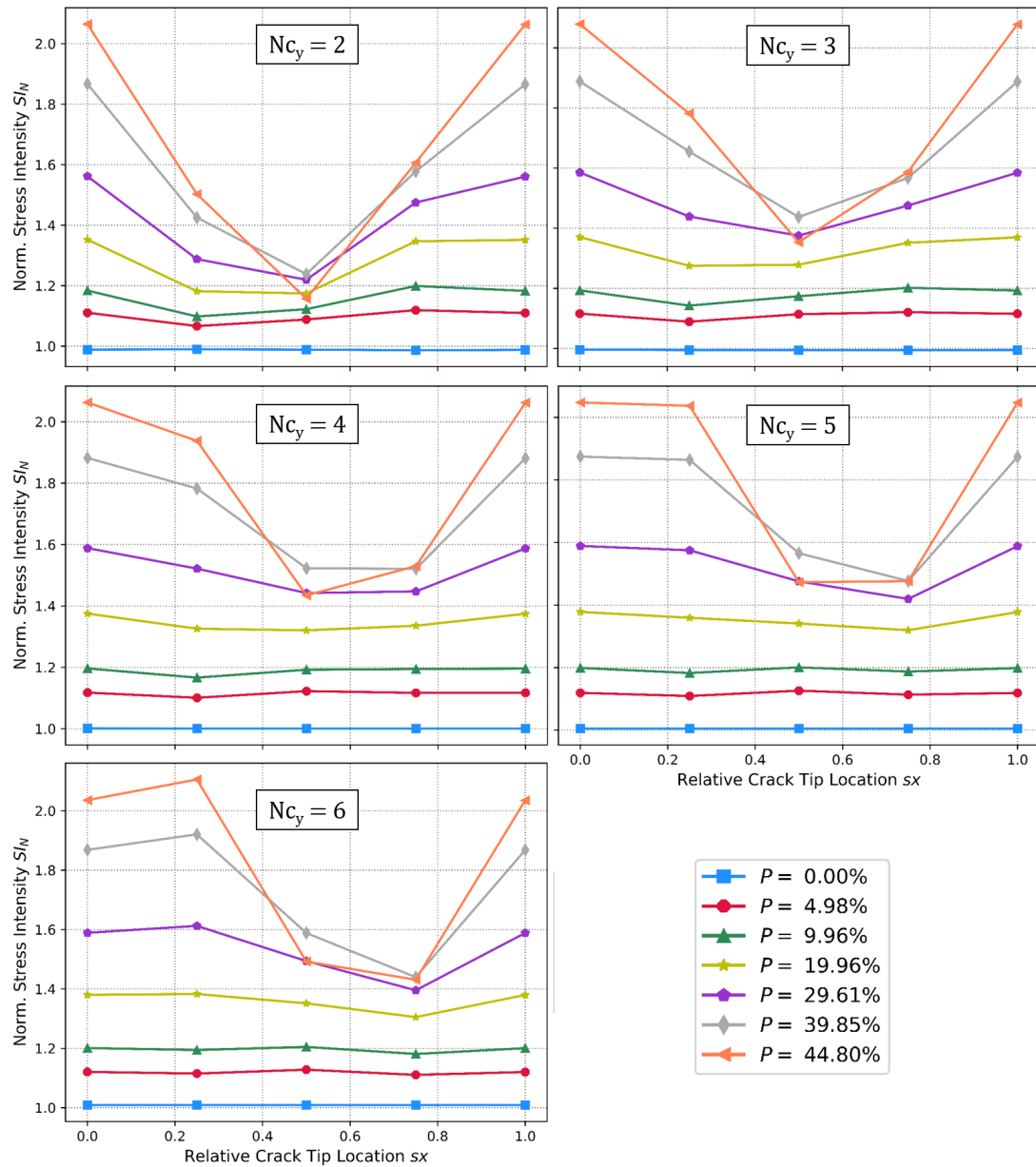


Figure B.1: Additional plots of the mesoscopic stress intensity variation of different specimens, categorised by their value of N_{c_y} .

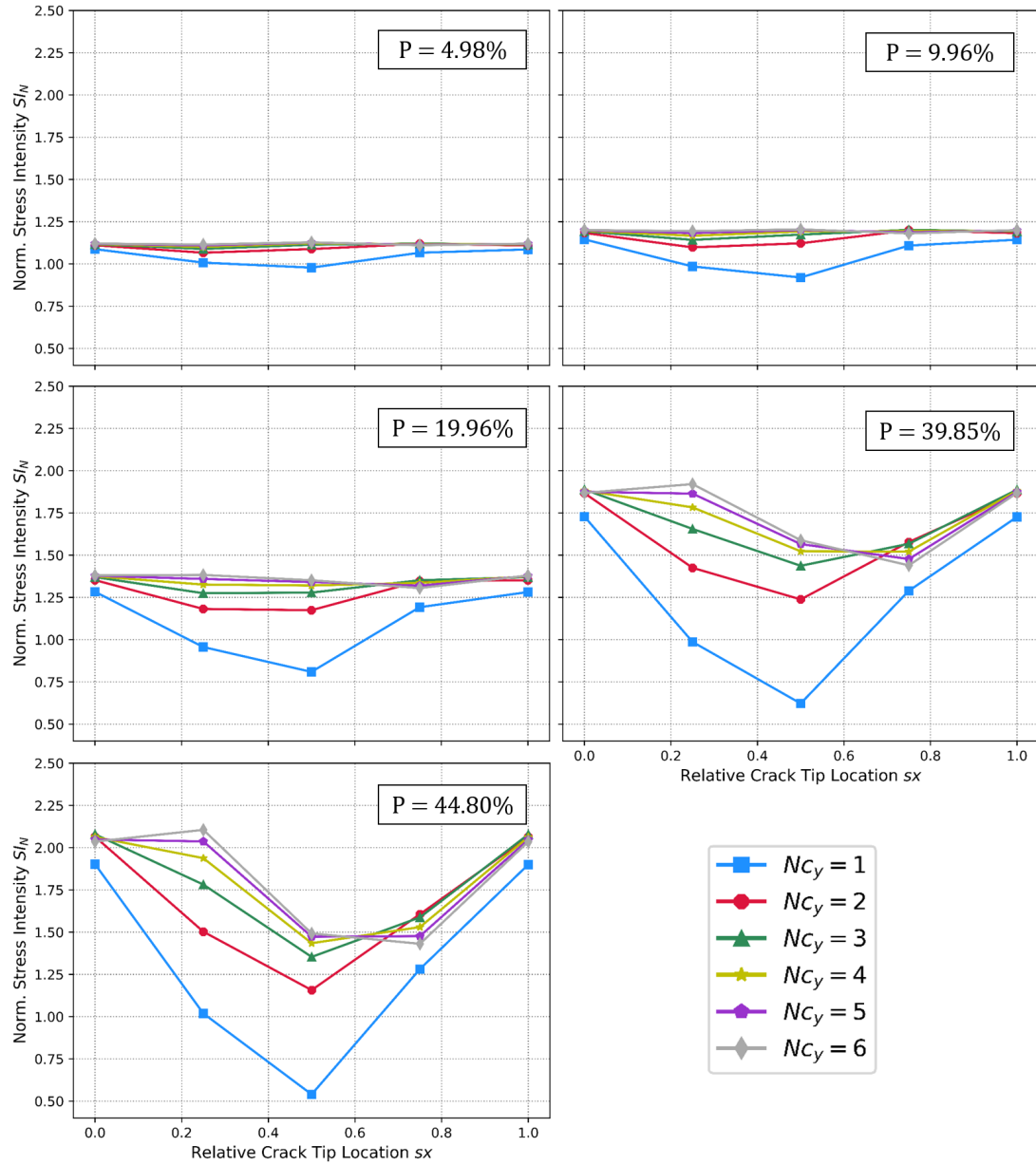


Figure B.2: Additional plots of the mesoscopic stress intensity variation of different specimens, categorised by their value of P .

APPENDIX C

Supplementary material for Chapter 5

The names of the specimens in the following tables and graphs are noted as "Specimen size - Void diameter - Specimen number". More specifically, the following options are used for each part of a specimen's name:

- Specimen size: S ($Nc_y = 1$), M ($Nc_y = 2$), L ($Nc_y = 4$)
- Void diameter: d0 ($d = 0mm$), d1.4 ($d = 1.4mm$), d2 ($d = 2mm$)
- Specimen number: 1,2,3...n. This value refers to the order of specimen manufacturing.

C.1 Quality assurance tables

In the following tables (Table C.1 and Table C.2), only the specimens that were not rejected and were actually used for testing are described. The date of manufacturing is also displayed on Table C.1, since the specimens were made in batches, which led to minor differences between them.

The values of the following graphs can be compared against the ones described in Chapters 3 and 5. The ratio h_1/h_2 refers to the ratio of the height of each specimen arm to ensure that the specimen is symmetric, implying mode I behaviour. Any significant differences between the designed and manufactured values are addressed in Chapter 5.

The differences observed in porosity from the designed value are due to the fact that the manufactured specimens have a different design (incorporating the loading block), which adds extra weight. The estimation of the porosity here is only indicative, to ensure self-similarity. In some specimens the voids were not successfully cut through the thickness of the specimen and the material could not be removed, thus adding weight. Such defects were left in the material only in the cases where they were not located in the near-tip area.

Finally, note that eccentricity is not the same as the shape anisotropy ratio SR described in Chapter 5.

Table C.1: Quality assurance of the tested specimens' macroscopic features

Specimen Name	Date of manufacturing	Weight (g)	Porosity (%)	h (mm)	AR	h_1/h_2	α/W
<i>S-d0-1</i>	29/11/2016	5.11	n/a	5.73	12.44	0.96	0.46
<i>S-d0-2</i>	29/11/2016	5.10	n/a	5.72	12.47	1.00	0.46
<i>S-d0-3</i>	29/11/2016	5.12	n/a	5.76	12.43	1.03	0.45
<i>M-d0-1</i>	07/03/2018	19.64	n/a	11.64	12.32	1.07	0.48
<i>M-d0-2</i>	07/03/2018	19.77	n/a	11.67	12.25	1.02	0.48
<i>M-d0-3</i>	07/03/2018	19.98	n/a	11.57	12.43	0.99	0.47
<i>L-d0-1</i>	07/03/2018	77.98	n/a	23.80	12.12	1.01	0.49
<i>L-d0-2</i>	07/03/2018	78.81	n/a	23.69	12.16	1.00	0.49
<i>L-d0-3</i>	07/03/2018	79.66	n/a	23.81	12.10	1.00	0.49
<i>S-d1.4-2</i>	29/11/2016	4.43	13.1	5.61	12.68	0.98	0.46
<i>S-d1.4-4</i>	29/11/2016	4.46	12.4	5.58	12.71	1.03	0.45
<i>S-d1.4-8</i>	29/11/2016	4.37	14.3	5.67	12.66	0.97	0.45
<i>M-d1.4-3</i>	07/03/2018	16.95	14.0	11.65	12.32	1.09	0.47
<i>M-d1.4-7</i>	24/05/2018	16.91	14.2	11.67	12.23	1.01	0.48
<i>M-d1.4-10</i>	24/05/2018	16.92	14.1	11.69	12.27	1.04	0.48
<i>L-d1.4-3</i>	07/03/2018	70.13	10.1	23.56	12.13	0.99	0.49
<i>L-d1.4-10</i>	24/05/2018	67.19	13.9	23.71	12.12	1.05	0.49
<i>L-d1.4-11</i>	24/05/2018	67.50	13.5	23.78	12.06	1.04	0.49
<i>S-d2-2</i>	29/11/2016	3.78	25.9	5.69	12.44	0.94	0.45
<i>S-d2-4</i>	29/11/2016	3.75	26.5	5.65	12.61	1.02	0.46
<i>S-d2-6</i>	29/11/2016	3.78	25.9	5.67	12.54	0.97	0.45
<i>M-d2-2</i>	07/03/2018	13.81	29.9	11.69	12.22	0.87	0.47
<i>M-d2-7</i>	24/05/2018	13.97	29.1	11.79	12.09	0.98	0.47
<i>M-d2-9</i>	24/05/2018	13.92	29.3	11.81	12.11	1.06	0.48
<i>L-d2-1</i>	24/05/2018	56.13	28.0	23.77	12.07	0.94	0.49
<i>L-d2-2</i>	24/05/2018	54.95	29.6	23.85	12.07	0.95	0.49
<i>L-d2-4</i>	24/05/2018	57.03	26.9	23.59	12.12	1.05	0.49

Table C.2: Quality assurance of the tested specimens' mesoscopic features as extracted by MATLAB

Specimen Name	Size x (mm)	Size y (mm)	Void circularity	Void eccentricity	Visual inspection comments
<i>S</i> - <i>d</i> 1.4 - 2	3.57	3.06	0.73	0.42	n/a
<i>S</i> - <i>d</i> 1.4 - 4	3.56	3.05	0.63	0.36	n/a
<i>S</i> - <i>d</i> 1.4 - 8	3.53	3.00	0.73	0.41	Sides of arms are curved.
<i>M</i> - <i>d</i> 1.4 - 3	3.51	3.03	1.08	0.48	n/a
<i>M</i> - <i>d</i> 1.4 - 7	3.57	3.01	1.06	0.06	n/a
<i>M</i> - <i>d</i> 1.4 - 10	3.57	3.09	1.11	0.52	n/a
<i>L</i> - <i>d</i> 1.4 - 3	3.56	3.09	1.13	0.39	Bent out of plane from the thermal stresses.
<i>L</i> - <i>d</i> 1.4 - 10	3.55	3.09	1.05	0.49	Bent out of plane from the thermal stresses.
<i>L</i> - <i>d</i> 1.4 - 11	3.57	3.08	1.04	0.15	Bent out of plane from the thermal stresses.
<i>S</i> - <i>d</i> 2 - 2	3.47	2.96	0.84	0.29	n/a
<i>S</i> - <i>d</i> 2 - 4	3.49	2.99	0.91	0.17	n/a
<i>S</i> - <i>d</i> 2 - 6	3.47	2.99	0.86	0.27	Sides of arms have a slight curvature.
<i>M</i> - <i>d</i> 2 - 2	3.56	3.70	0.95	0.55	Bent out of plane from the thermal stresses, minor burrs on the surface, voids on first row equilaterally of the crack tip have a larger distance than the rest of the specimen.
<i>M</i> - <i>d</i> 2 - 7	3.59	3.04	0.95	0.27	Bent out of plane from the thermal stresses.
<i>M</i> - <i>d</i> 2 - 9	3.58	3.08	1.05	0.31	Bent out of plane from the thermal stresses.
<i>L</i> - <i>d</i> 2 - 1	3.57	3.08	0.94	0.39	Bent out of plane from the thermal stresses.
<i>L</i> - <i>d</i> 2 - 2	3.58	3.11	0.95	0.29	Bent out of plane from the thermal stresses.
<i>L</i> - <i>d</i> 2 - 4	3.56	3.09	1.05	0.33	Bent out of plane from the thermal stresses.

C.2 Experimental force-displacement graphs

In this section, the force-displacement graphs for each specimen tested are presented, categorised by their porosity. It can be seen in the graph that each 3 specimens of the same size and porosity have a very similar behaviour with minimal variations. While the homogeneous specimens have an almost constant slope for all different sizes, this is not the case for the porous materials. This is also reflected in the results presented in Chapter 5.

Note that the unloading of the specimens is not plotted to reduce clutter from the graph.

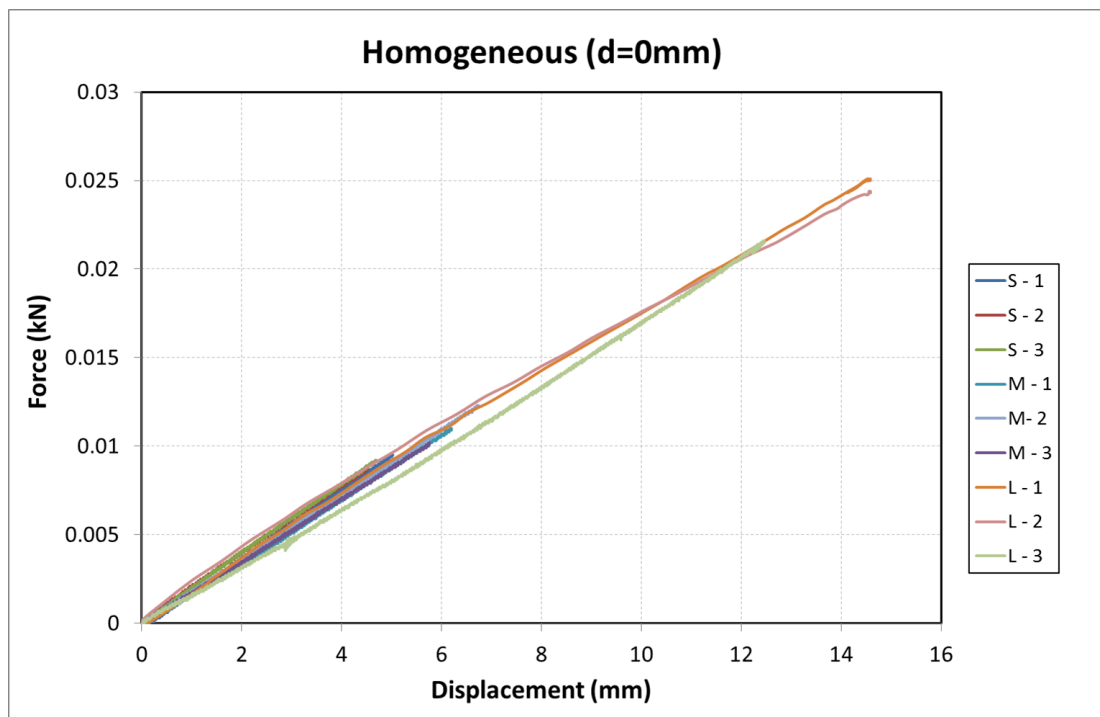
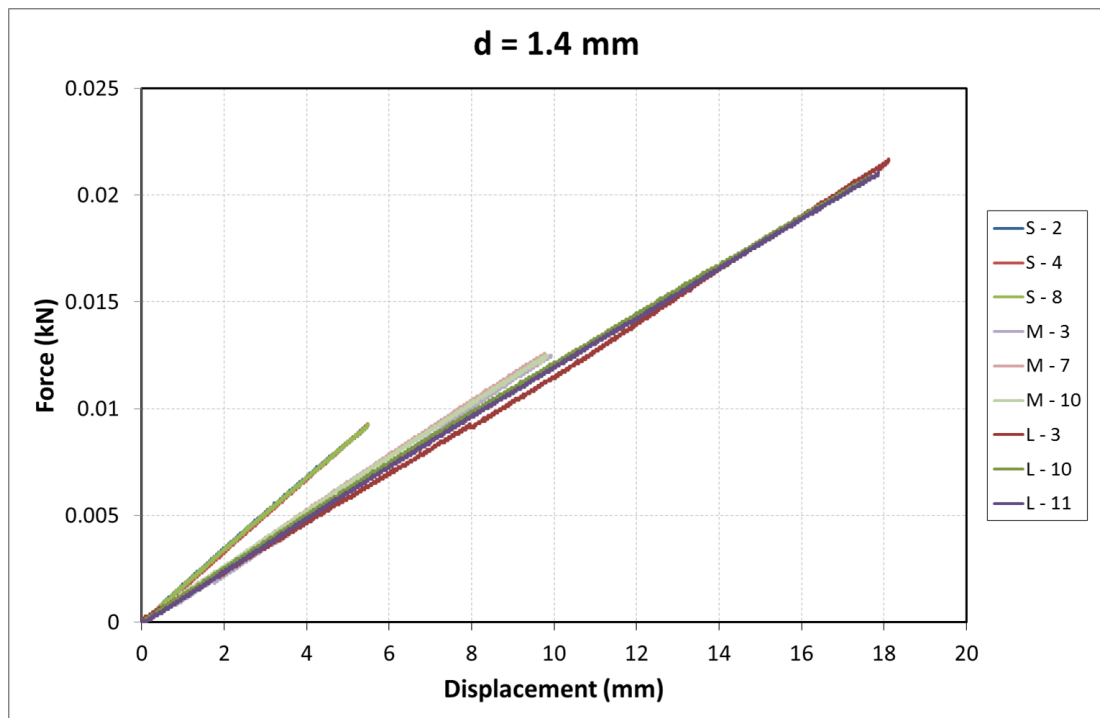
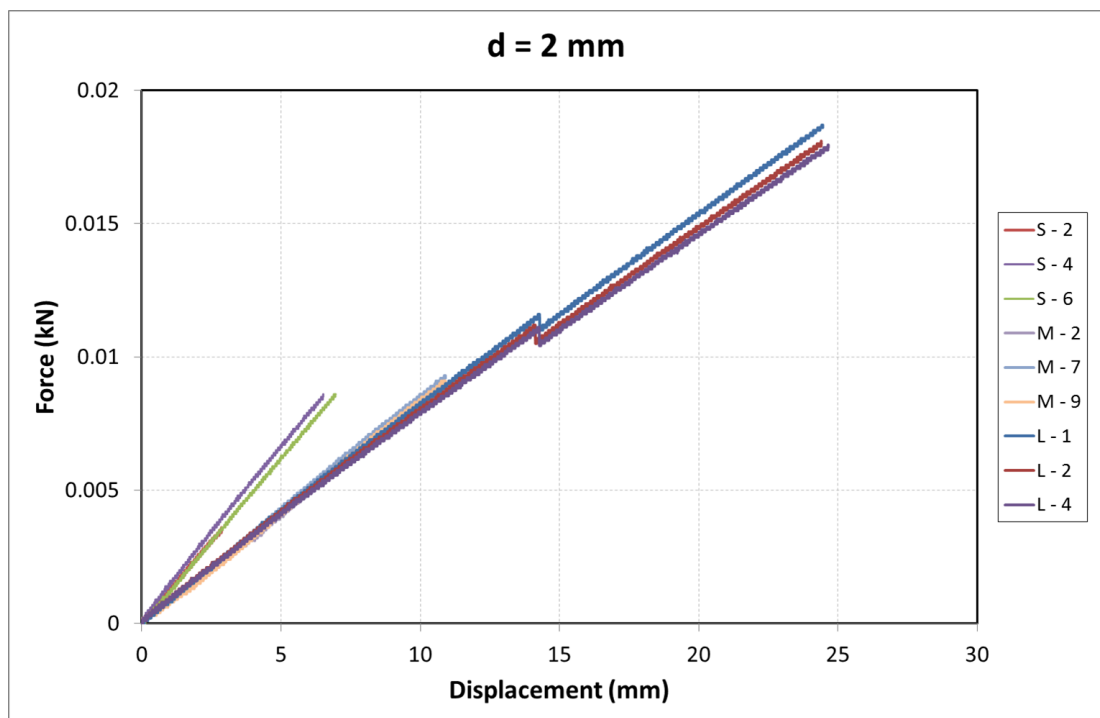


Figure C.1: Force-displacement graph for manufactured homogeneous specimens with $d = 0mm$

Figure C.2: Force-displacement graph for manufactured specimens with $d = 1.4 \text{ mm}$ Figure C.3: Force-displacement graph for manufactured specimens with $d = 2 \text{ mm}$

APPENDIX D

Supplementary material for Chapter 6

D.1 Additional contour plots for specimens with voids

Below are some additional contour plots from the DOE of Chapter 6, which were not included in the chapter, since they are similar to the ones presented and do not add to the conclusions.

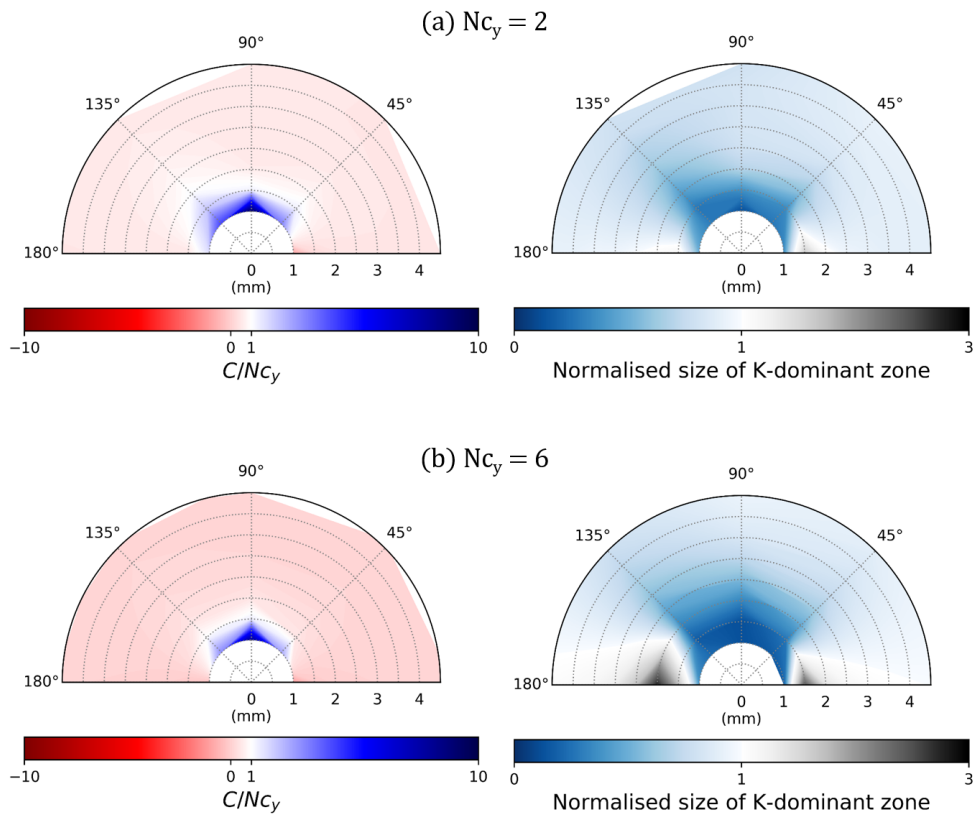


Figure D.1: Additional graphs for the variations of the amplitude of $A_{1/2}$ stress and the size of K-dominant zone for specimens with voids of $d = 1.64\text{mm}$

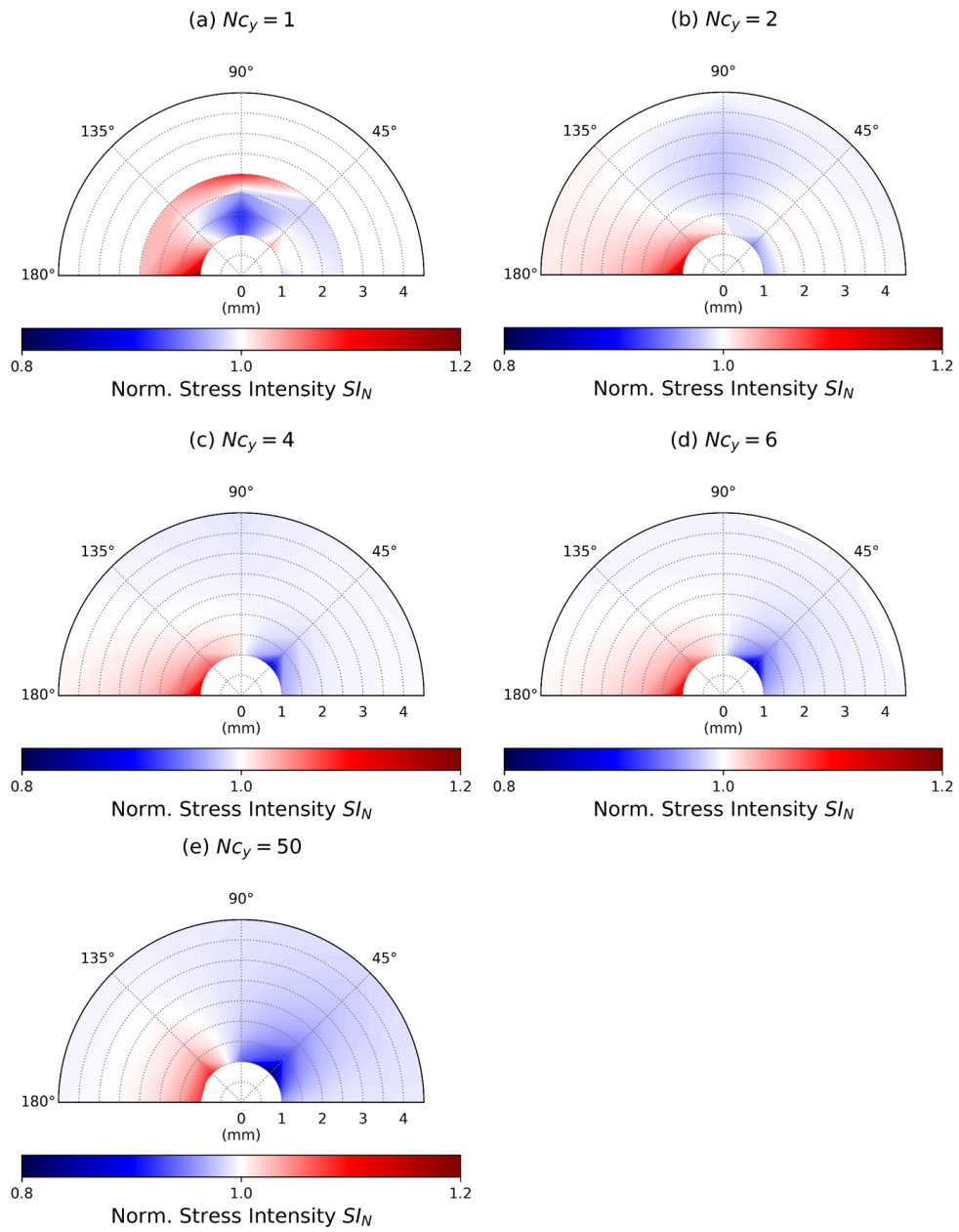


Figure D.2: Contour plots of stress intensity variations for specimens with voids of $d = 0.82\text{mm}$

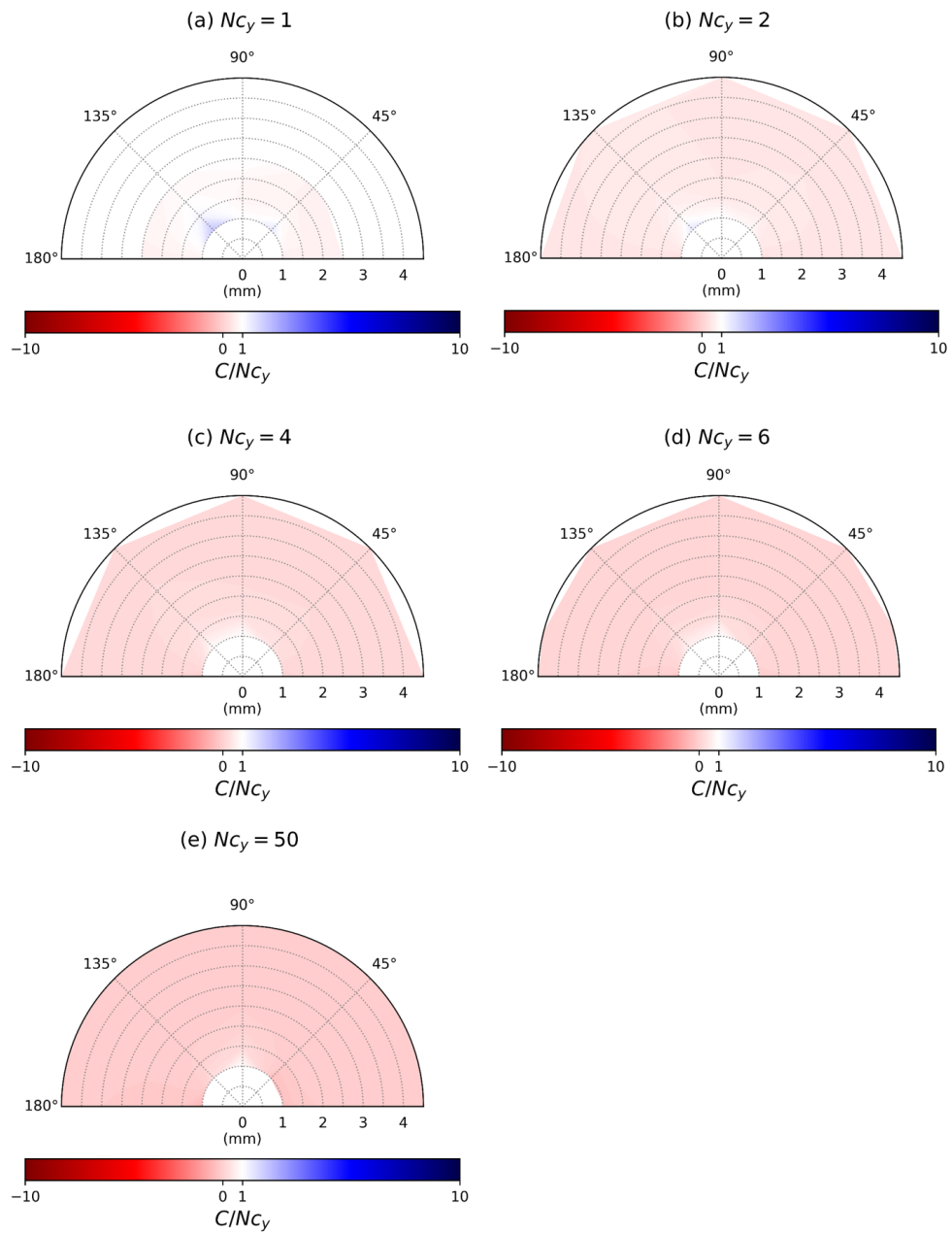


Figure D.3: Contour plots of the amplitude of $A_{1/2}$ stress variations for specimens with voids of $d = 0.82\text{mm}$

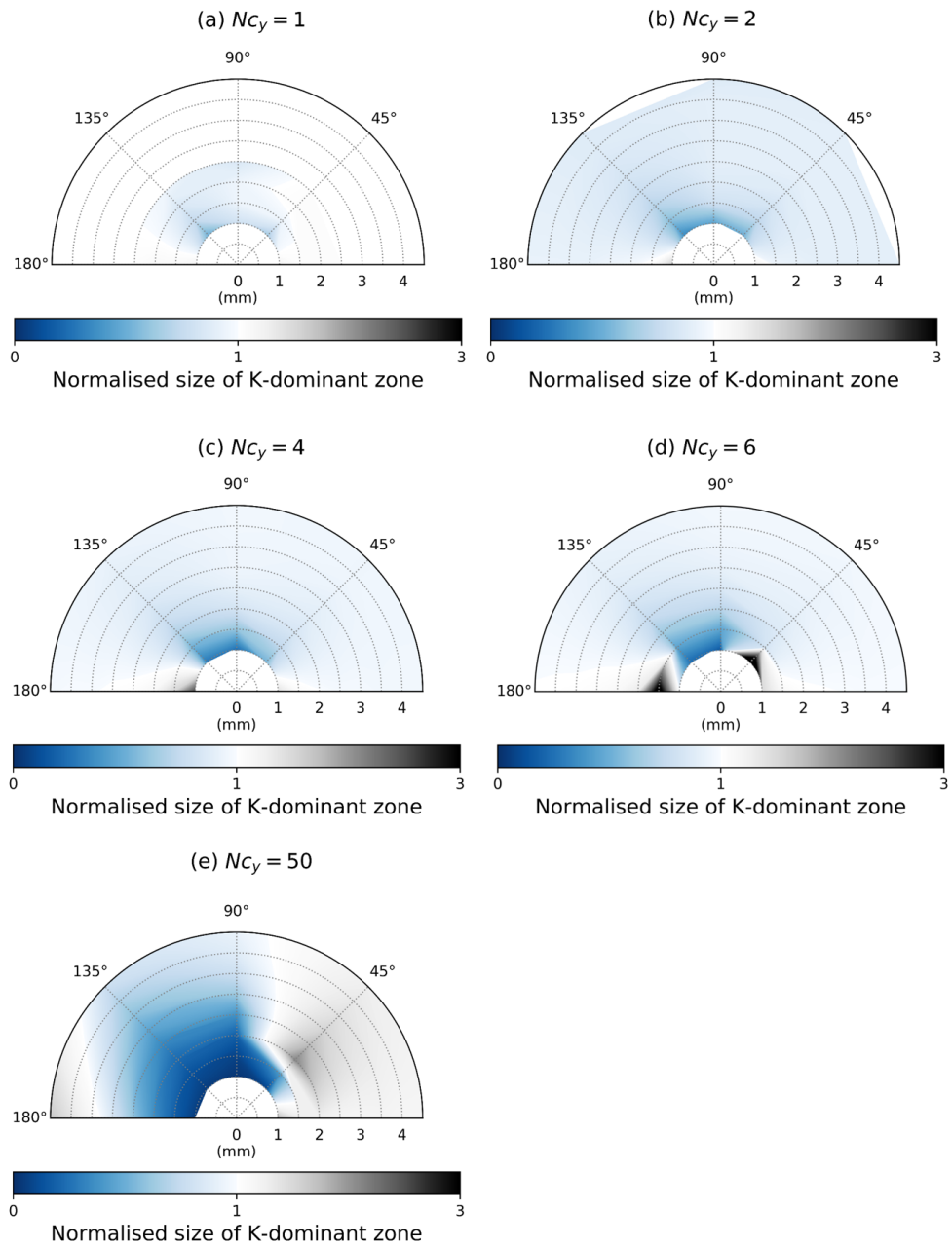


Figure D.4: Contour plots of the size of K-dominant zone for specimens with voids of $d = 0.82\text{mm}$

D.2 Additional contour plots for specimens with stiff inclusions

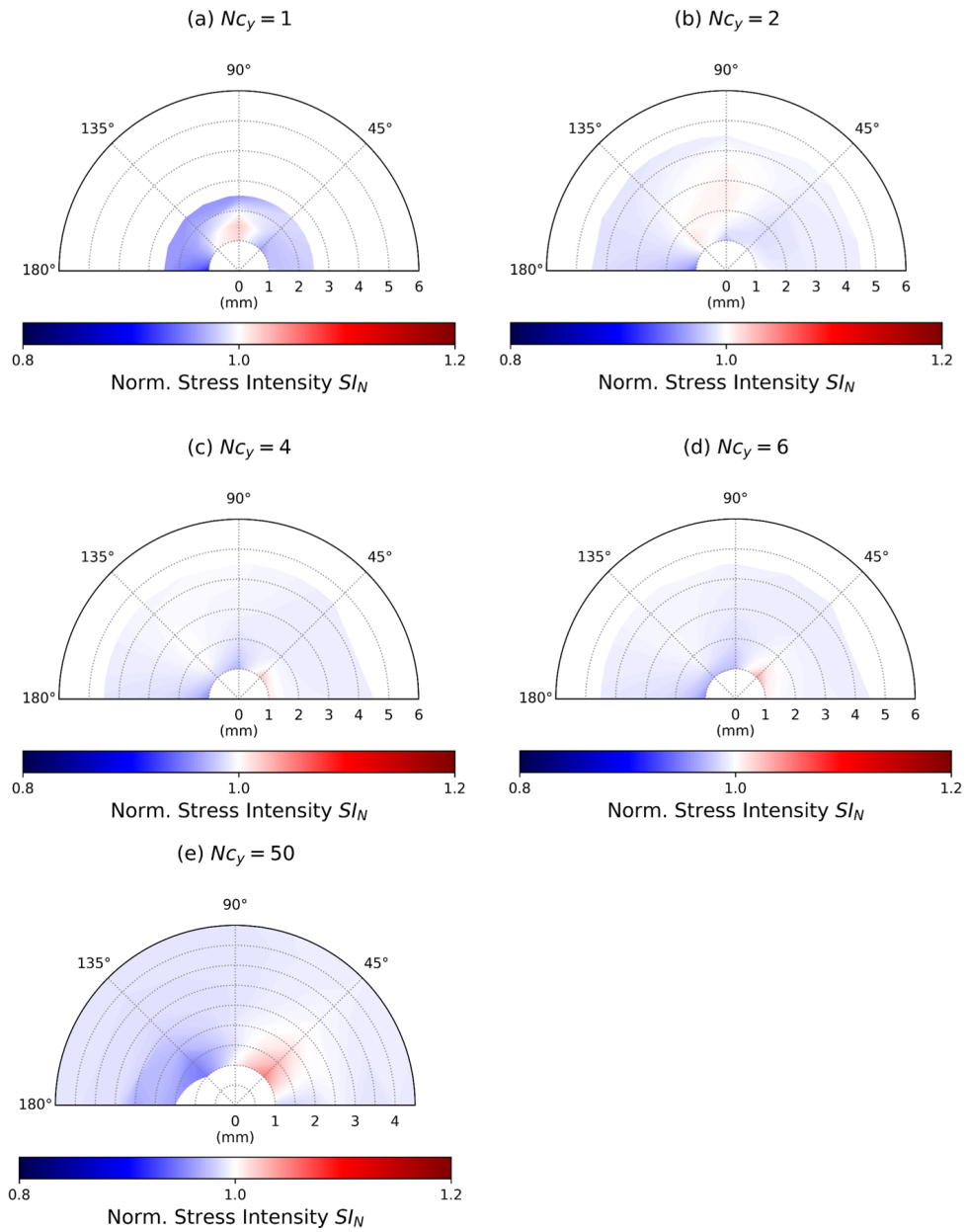


Figure D.5: Contour plots of stress intensity variations for specimens with stiff inclusions of $d = 0.82\text{mm}$

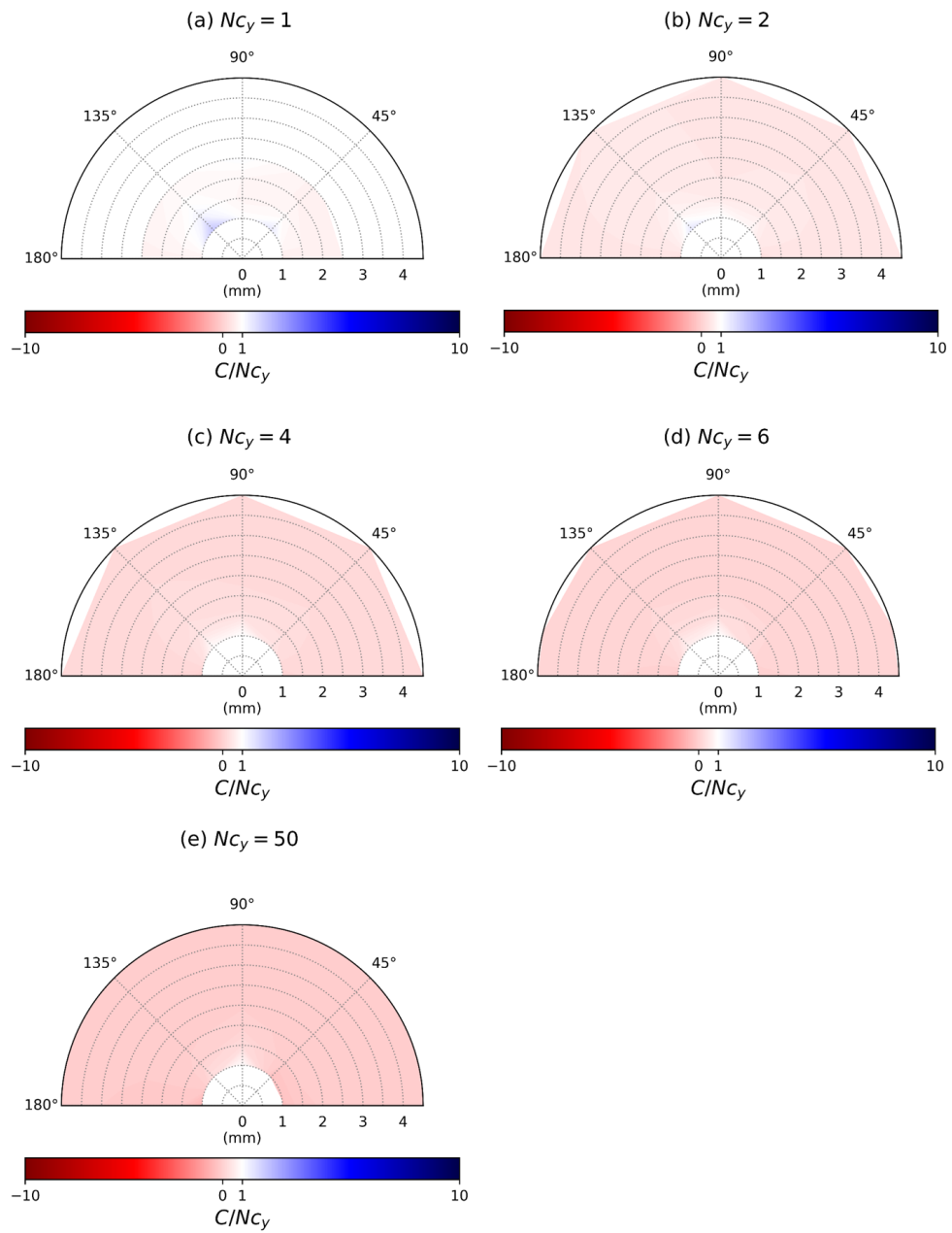


Figure D.6: Contour plots of the amplitude of $A_{1/2}$ stress variations for specimens with stiff inclusions of $d = 0.82\text{ mm}$

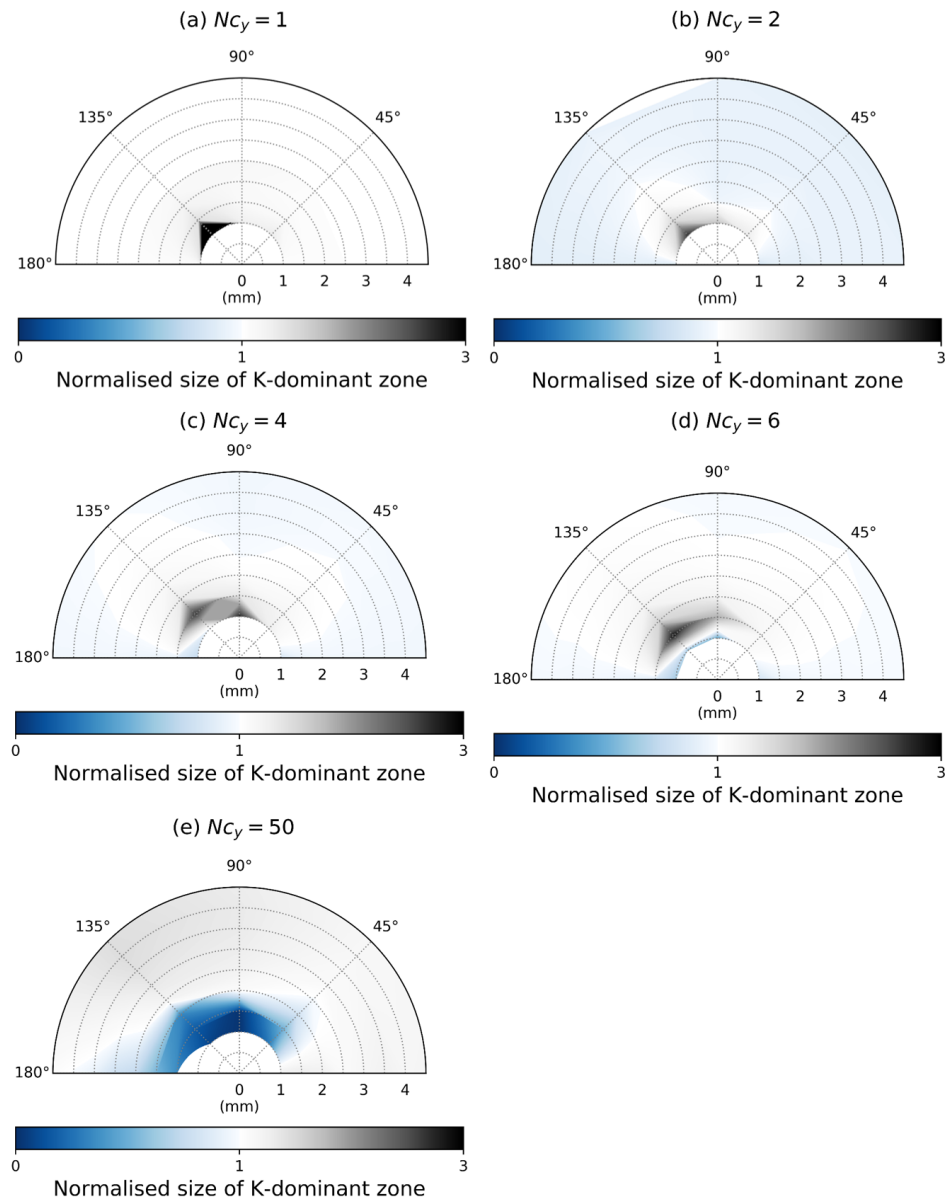


Figure D.7: Contour plots of the size of K-dominant zone for specimens with stiff inclusions of $d = 0.82\text{mm}$

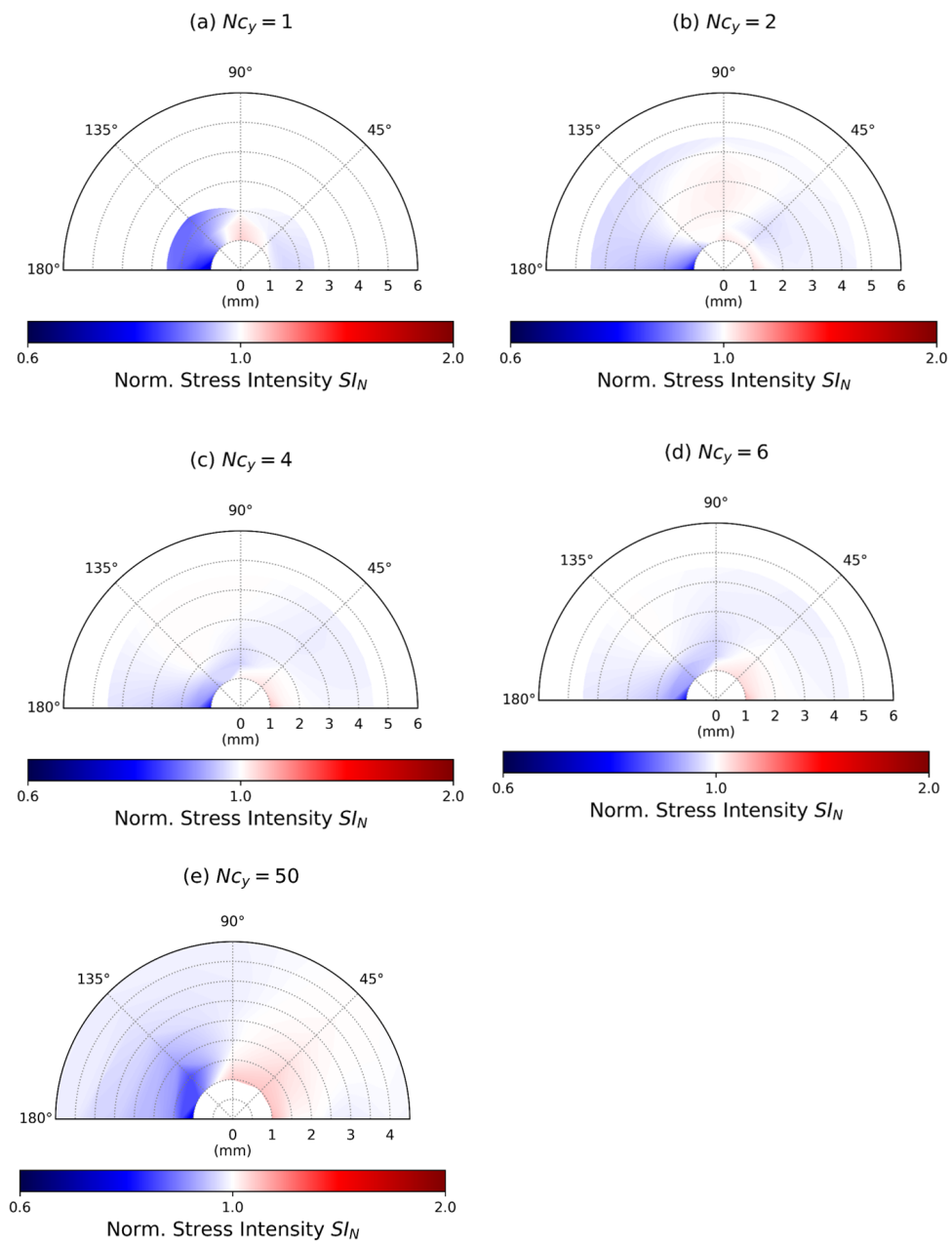


Figure D.8: Contour plots of stress intensity variations for specimens with stiff inclusions of $d = 1.64\text{mm}$

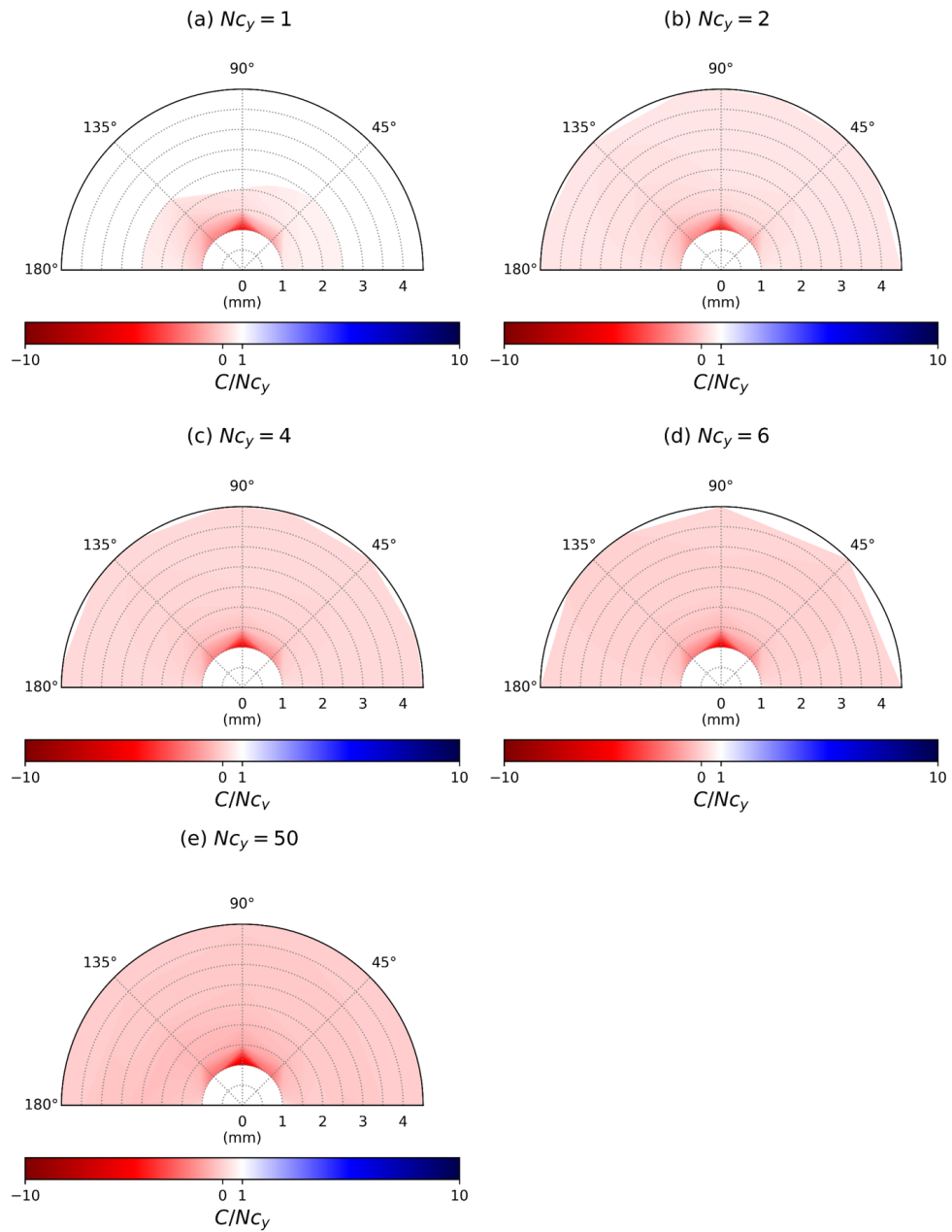


Figure D.9: Contour plots of the amplitude of $A_{1/2}$ stress variations for specimens with stiff inclusions of $d = 1.64\text{mm}$

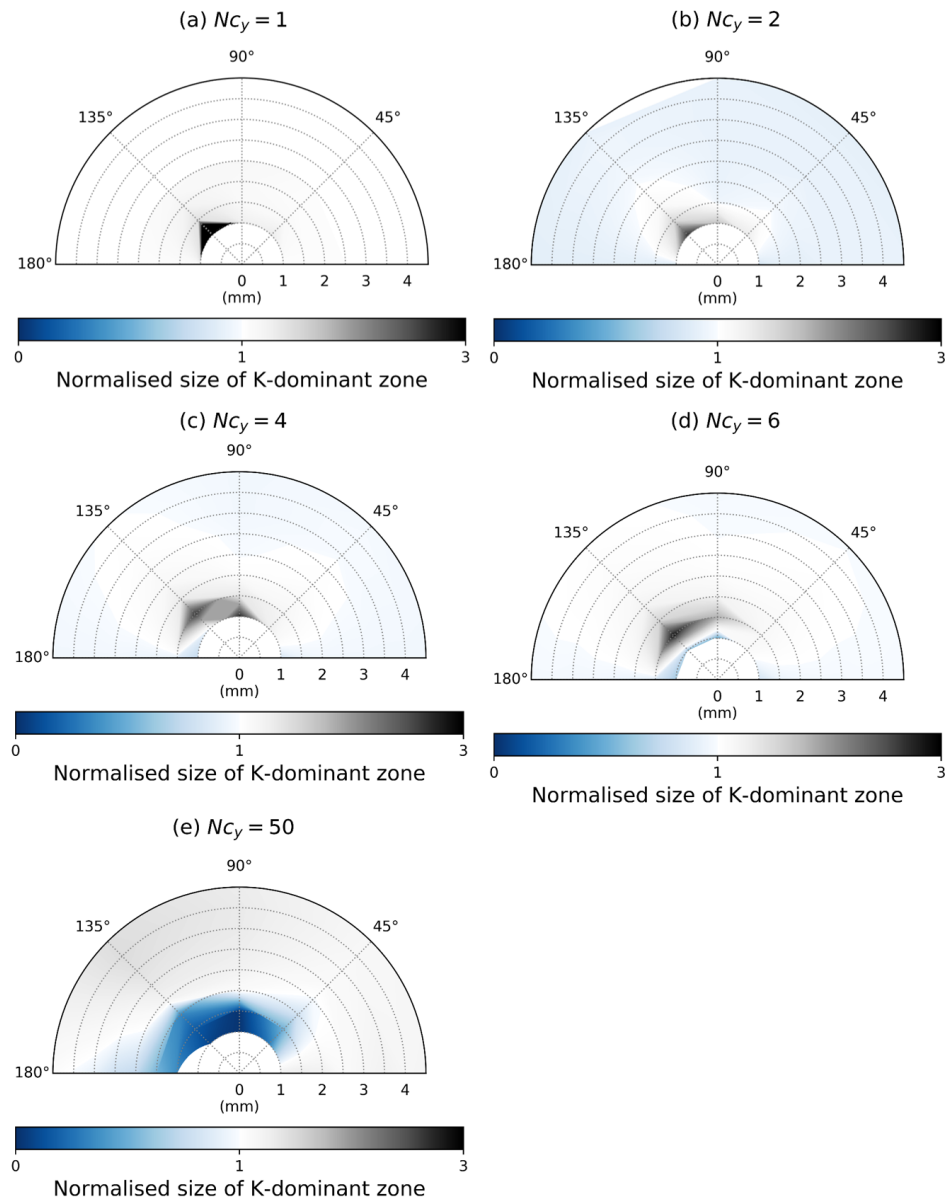


Figure D.10: Contour plots of the size of K-dominant zone for specimens with stiff inclusions of $d = 1.64\text{mm}$

Bibliography

- [1] T. Anderson. *Fracture Mechanics: Fundamentals and Applications*. 2005.
- [2] D. Gross. “Some remarks on the history of fracture mechanics”. In: *The History of Theoretical, Material and Computational Mechanics - Mathematics Meets Mechanics and Engineering. Lecture Notes in Applied Mathematics and Mechanics*. Ed. by S. E. (eds). Vol. 1. July. Berlin, Heidelberg: Springer, 2014.
- [3] S. D. Antolovich, A. Saxena, and W. W. Gerberich. “Fracture mechanics – An interpretive technical history”. In: *Mechanics Research Communications* 91 (2018), pp. 46–86.
- [4] M. D. Hayes, D. B. Edwards, and A. R. Shah. “Fractography Basics”. In: *Fractography in Failure Analysis of Polymers*. 2015, pp. 48–92.
- [5] NDT Resource Center. *Fracture Toughness*.
- [6] J. R. Rice. “Mathematical Analysis in the Mechanics of Fracture”. In: *Fracture: An Advanced Treatise Mathematical Fundamentals* N.Y 2 (1968), pp. 191–311.
- [7] M. L. Williams. “On the Stress Distribution at the Base of a Stationary Crack”. In: *Journal of Applied Mechanics* 24.3 (1957), pp. 109–114.
- [8] H. M. Westergaard. *Bearing pressures and cracks*. 1939.
- [9] G. Irwin and J. Kies. “Critical energy rate analysis of fracture strength”. In: *Welding Research Supplement* (1954).
- [10] Z. P. Bazant. “Size effect in blunt fracture: concrete, rock, metal”. In: *Journal of Engineering Mechanics* 110.4 (1984).
- [11] E. Linul et al. “Size Effect on Fracture Toughness of Rigid Polyurethane Foams”. In: *Solid State Phenomena* 188 (2012), pp. 205–210.
- [12] S.-H. Cheng and C. T. Sun. “Size-Dependent Fracture Toughness of Nanoscale Structures: Crack-Tip Stress Approach in Molecular Dynamics”. In: *Journal of Nanomechanics and Micromechanics* 4.4 (2014).
- [13] L. J. Gibson and M. F. Ashby. *Cellular Solids*. Vol. 2. 6. Cambridge: Cambridge University Press, 1997, pp. 546–8.
- [14] E. P. Erasmus et al. “Effects of Sintering Temperature on Crystallization and Fabrication of Porous Bioactive Glass Scaffolds for Bone Regeneration”. In: *Scientific Reports* 7 (2017).
- [15] L. Marsavina and D. M. Constantinescu. “Failure and Damage in Cellular Materials”. In: *Failure and Damage Analysis of Advanced Materials*. Ed. by H. Altenbach and T. Sadowski. 2015.

- [16] A. P. S. Lau and G.-F. Chen. *Porous materials : processing and applications*. Elsevier Science, 2014, p. 577.
- [17] W. Wei and Y. Xia. “Geometrical, fractal and hydraulic properties of fractured reservoirs: A mini-review”. In: *Ausasia Science and Technology Press Adv. Geo-energ. Res. Adv. Geo-energ. Res* 1.11 (2017), pp. 31–38.
- [18] B. Berkowitz. “Characterizing flow and transport in fractured geological media: A review”. In: *Advances in Water Resources* 25.8-12 (2002), pp. 861–884.
- [19] R. Bourcier et al. “The influence of porosity on the deformation and fracture of alloys”. In: *Acta Metallurgica* 34.12 (1986), pp. 2443–2453.
- [20] J. Holmes and R. A. Queeney. “Fatigue Crack Initiation in a Porous Steel”. In: *Powder Metallurgy* 28.4 (1985), pp. 231–235.
- [21] N. Chawla and X. Deng. “Microstructure and mechanical behavior of porous sintered steels”. In: *Materials Science and Engineering: A* 390.1-2 (2005), pp. 98–112.
- [22] A. Hadrboletz and B. Weiss. “Fatigue behaviour of iron based sintered material: a review”. In: *International Materials Reviews* 42.1 (1997), pp. 1–44.
- [23] Z. Yang et al. “Porosity elimination and heat treatment of diode laser-clad homogeneous coating on cast aluminum-copper alloy”. In: *Surface and Coatings Technology* 321 (2017), pp. 26–35.
- [24] R. Cunningham et al. “Synchrotron-Based X-ray Microtomography Characterization of the Effect of Processing Variables on Porosity Formation in Laser Power-Bed Additive Manufacturing of Ti-6Al-4V”. In: *JOM* 69.3 (2017), pp. 479–484.
- [25] S. W. Williams et al. “Wire + Arc Additive Manufacturing”. In: *Materials Science and Technology* 32.7 (2016), pp. 641–647.
- [26] R. Dorey. “Microstructure–property relationships: How the microstructure of the film affects its properties”. In: *Ceramic Thick Films for MEMS and Microdevices*. William Andrew Publishing, 2012. Chap. 4, pp. 85–112.
- [27] M. Qian et al. “Additive manufacturing and postprocessing of Ti-6Al-4V for superior mechanical properties”. In: *MRS Bulletin* 41.10 (2016), pp. 775–784.
- [28] M. Yakout et al. “The selection of process parameters in additive manufacturing for aerospace alloys”. In: *The International Journal of Advanced Manufacturing Technology* 92.5-8 (2017), pp. 2081–2098.
- [29] L. J. Vandeperre, J. Wang, and W. J. Clegg. “Effects of porosity on the measured fracture energy of brittle materials”. In: *Philosophical Magazine* 84.34 (2004), pp. 3689–3704.
- [30] E. Zhang and B. Wang. “On the compressive behaviour of sintered porous coppers with low to medium porosities—Part I: Experimental study”. In: *International Journal of Mechanical Sciences* 47.4-5 (2005), pp. 744–756.
- [31] M. Ryvkin. “Employing the Discrete Fourier Transform in the Analysis of Multiscale Problems”. In: *International Journal for Multiscale Computational Engineering* 6.5 (2008), pp. 435–449.
- [32] M. Ryvkin and L. Slepyan. “Crack in a 2D beam lattice: Analytical solutions for two bending modes”. In: *Journal of the Mechanics and Physics of Solids* 58.6 (2010), pp. 902–917.
- [33] M. Ryvkin and J. Aboudi. “Crack resistance in two-dimensional periodic materials of medium and low porosity”. In: *Engineering Fracture Mechanics* 78.10 (2011), pp. 2153–2160.

-
- [34] Z. Y. Deng et al. “Reinforcement by crack-tip blunting in porous ceramics”. In: *Journal of the European Ceramic Society* 24.7 (2004), pp. 2055–2059.
- [35] H. Altenbach and A. Ochsner, eds. *Cellular and Porous Materials in Structure and Processes*. SpringerWienNewYork, 2010.
- [36] G. M. Viana and L. A. Carlsson. “Mechanical Properties and Fracture Characterization of Cross-Linked PVC Foams”. In: *Journal of Sandwich Structures and Materials* 4.April (2002), pp. 99–113.
- [37] P. Poapongsakorn and L. A. Carlsson. “Fracture toughness of closed-cell PVC foam : Effects of loading configuration and cell size”. In: *Composite Structures* 102 (2013), pp. 1–8.
- [38] L. Marsavina and E. Linul. “Fracture toughness of polyurethane foams. Experiments versus micromechanical models.” In: *Proc 18th European Conference on Fracture*. 2010, pp. 1–8.
- [39] M. E. Kabir, M. C. Saha, and S. Jeelani. “Tensile and fracture behavior of polymer foams”. In: *Materials Science and Engineering A* 429.1-2 (2006), pp. 225–235.
- [40] A. Ableidinger. “Some aspects on the fracture behaviour of cellular foams”. PhD thesis. Vienna University of Technology, 2000.
- [41] S.-J. Lee, J. Wang, and B. V. Sankar. “A micromechanical model for predicting the fracture toughness of functionally graded foams”. In: *International Journal of Solids and Structures* 44.11-12 (2007), pp. 4053–4067.
- [42] I. Christodoulou and P. J. Tan. “Crack initiation and fracture toughness of random Voronoi honeycombs”. In: *Engineering Fracture Mechanics* 104 (2013), pp. 140–161.
- [43] F. Lipperman, M. Ryvkin, and M. B. Fuchs. “Fracture toughness of two-dimensional cellular material with periodic microstructure”. In: *International Journal of Fracture* 146.4 (2007), pp. 279–290.
- [44] N. A. Fleck and X. Qiu. “The damage tolerance of elastic-brittle, two-dimensional isotropic lattices”. In: *Journal of the Mechanics and Physics of Solids* 55.3 (2007), pp. 562–588.
- [45] N. E. R. Romijn and N. A. Fleck. “The fracture toughness of planar lattices: Imperfection sensitivity”. In: *Journal of the Mechanics and Physics of Solids* 55.12 (2007), pp. 2538–2564.
- [46] D. J. Green. “Fabrication and mechanical properties of lightweight ceramics produced by sintering of hollow spheres”. In: *Journal of American Ceramic Society* 409 (1985), pp. 403–409.
- [47] S. Choi and B. V. Sankar. “A micromechanical method to predict the fracture toughness of cellular materials”. In: *International Journal of Solids and Structures* 42.5-6 (2005), pp. 1797–1817.
- [48] M. F. Ashby. “The properties of foams and lattices.” In: *Philosophical transactions. Series A, Mathematical, physical, and engineering sciences* 364.1838 (2005), pp. 15–30.
- [49] M. V. Alonso, M. L. Auad, and S. Nutt. “Short-fiber-reinforced epoxy foams”. In: *Composites Part A: Applied Science and Manufacturing* 37.11 (2006), pp. 1952–1960.
- [50] N. A. Fleck, V. S. Deshpande, and M. F. Ashby. “Micro-architected materials: past, present and future”. In: *Proceedings of the Royal Society of London A: Mathematical, Physical and Engineering Sciences* 466.2121 (2010).

- [51] L. Hongyun, Y. Jianda, and L. Zhonghua. “An approximate solution for the plane stress mode I crack interacting with an inclusion of arbitrary shape”. In: *Engineering Fracture Mechanics* 116 (2014), pp. 190–196.
- [52] L. Hongyun and L. Zhonghua. “Approximate solution for crack interacting with a gas-filled void”. In: *Engineering Fracture Mechanics* 134 (2015), pp. 168–173.
- [53] Z. H. Kassam, R. J. Zhang, and Z. Wang. “Finite element simulation to investigate interaction between crack and particulate reinforcements in metal-matrix composites”. In: *Materials Science and Engineering: A* 203.1-2 (1995), pp. 286–299.
- [54] M. B. Bush. *The interaction between a crack and a particle cluster*. Tech. rep. 1997, pp. 215–232.
- [55] L. Zhonghua and C. Qiang. *Crack-inclusion interaction for mode I crack analyzed by Eshelby equivalent inclusion method*. Tech. rep. 2002, pp. 29–40.
- [56] N Li and A Chudnovsky. *Energy analysis of crack interaction with an elastic inclusion*. Tech. rep. 1993, pp. 247–261.
- [57] X.-H. Liu and F. Erdogan. “The crack-inclusion interaction problem”. In: *Engineering Fracture Mechanics* 23.5 (1986), pp. 821–832.
- [58] S. Thomas, M. Mhaskar, and R. Sethuraman. “Stress intensity factors for circular hole and inclusion using finite element alternating method”. In: *Theoretical and Applied Fracture Mechanics* 33.2 (2000), pp. 73–81.
- [59] C Atkinson. *The interaction between a crack and an inclusion*. Tech. rep. 1972, pp. 127–136.
- [60] J. J. Han and Y. H. Chen. “T-effect for the interaction problem of an interface macrocrack with a near-tip microvoid”. In: *International Journal of Fracture* 102.3 (2000), pp. 205–222.
- [61] K. Hu, A. Chandra, and Y. Huang. “Multiple void-crack interaction”. In: *International Journal of Solids and Structures* 30.11 (1993), pp. 1473–1489.
- [62] D Leguillon and R Piat. “Fracture of porous materials – Influence of the pore size”. In: *Engineering Fracture Mechanics* 75 (2007), pp. 1840–1853.
- [63] J. D. Eshelby. *The Elastic Field Outside an Ellipsoidal Inclusion*. Tech. rep. 1271. 1959, pp. 561–569.
- [64] J. D. Eshelby. *The determination of the elastic field of an ellipsoidal inclusion, and related problems*. Tech. rep. 1957.
- [65] M. Valentini et al. “Crack Propagation in a Brittle Elastic Material With Defects”. In: *Journal of Applied Mechanics* 66.1 (1999), p. 79.
- [66] R. L. Kranz. “Crack-crack and crack-pore interactions in stressed granite”. In: *International Journal of Rock Mechanics and Mining Sciences & Geomechanics Abstracts* 16.1 (1979), pp. 37–47.
- [67] D. Misseroni et al. “Stress concentration near stiff inclusions: Validation of rigid inclusion model and boundary layers by means of photoelasticity”. In: *Engineering Fracture Mechanics* 121-122 (2014), pp. 87–97.
- [68] D. Misseroni et al. “Experimental and analytical insights on fracture trajectories in brittle materials with voids”. In: *International Journal of Solids and Structures* 63 (2015), pp. 219–225.
- [69] D. Leguillon et al. “Prediction of crack deflection in porous/dense ceramic laminates”. In: *Journal of the European Ceramic Society* 26.3 (2006), pp. 343–349.

- [70] L. Liu and X. Chen. “Controlled crack arrest in brittle thin films: The effect of embedded voids”. In: *Acta Materialia* 56.20 (2008), pp. 6214–6223.
- [71] S. Mani and T. M. Saif. “Mechanism of controlled crack formation in thin-film dielectrics”. In: *Applied Physics Letters* 86.20 (2005), p. 201903.
- [72] C. Shin, C. Wang, and P. Song. “Fatigue damage repair: a comparison of some possible methods”. In: *International Journal of Fatigue* 18.8 (1996), pp. 535–546.
- [73] M. Ayatollahi, S. Razavi, and H. Chamani. “Fatigue Life Extension by Crack Repair Using Stop-hole Technique under Pure Mode-I and Pure mode-II Loading Conditions”. In: *Procedia Engineering* 74 (2014), pp. 18–21.
- [74] F. Lipperman, M. Ryvkin, and M. B. Fuchs. “Crack arresting low-density porous materials with periodic microstructure”. In: *International Journal of Engineering Science* 46.6 (2008), pp. 572–584.
- [75] D. Leguillon et al. “Prediction of crack initiation at blunt notches and cavities - : size effects”. eng. In: *Engineering fracture mechanics* 74.15 (2007), pp. 2420–2436.
- [76] M. A. Dunn and M. A. Wheel. “Computational Analysis of the Size Effects Displayed in Beams with Lattice Microstructures”. In: *Generalized Continua as Models for Classical and Advanced Materials*. 2016, pp. 129–143.
- [77] M. A. Wheel. “A control volume-based finite element method for plane micropolar elasticity”. In: *International Journal for Numerical Methods in Engineering* February (2008), pp. 992–1006.
- [78] M. A. Wheel, J. C. Frame, and P. E. Riches. “Is smaller always stiffer ? On size effects in supposedly generalised continua”. In: *International Journal of Solids and Structures* 67-68 (2015), pp. 84–92.
- [79] M. A. Wheel, J. C. Frame, and P. E. Riches. “Paradoxical Size Effects in Composite Laminates and Other Heterogeneous Materials”. In: 2016, pp. 443–457.
- [80] C Tekoglu et al. “Size effects in foams: Experiments and modeling”. In: *Progress in Materials Science journal* 56 (2011), pp. 109–138.
- [81] C. Tekoglu. *Size effects in cellular solids*. 2007, p. 133.
- [82] C. Tekoglu and P. R. Onck. “Size effects in the mechanical behavior of cellular materials”. In: *Journal of Materials Science* 40.22 (2005), pp. 5911–5917.
- [83] L. da Vinci. *Testing the Strength of Iron Wires of Various Lengths*. Madrid (Spain): Biblioteca Nacional.
- [84] G. Galilei. *Discorsi i Dimostrazioni Matematiche intorno a due Nuove Scienze*. 1638.
- [85] E Mariotte. “Traite du mouvement des eaux (posthumously), de la Hire M ed”. In: *English transl by Desvaguliers JT, London (1718)* 249 (1686).
- [86] Z. P. Bazant and E.-p. Chen. *Scaling of structural failure* *. 1997.
- [87] W. Weibull. *The phenomenon of rupture in solids*, Stockholm: Generalstabens litografiska anstalts forlag, 1939.
- [88] R. H. Leicester. “The size effect of nothces”. In: *Proc., 2nd Australasian Conf. on Mech. of Struct. Mater.* 4 (1969).
- [89] A. Carpinteri. “Decrease of apparent tensile and bending strength with specimen size: Two different explanations based on fracture mechanics”. In: *International Journal of Solids and Structures* 25.4 (1989), pp. 407–429.

- [90] A. Arslan and R. Ince. “The neural network approximation to the size effect in fracture of cementitious materials”. In: *Engineering Fracture Mechanics* 54.2 (1996), pp. 249–261.
- [91] B. L. Karihaloo. “Size effect in shallow and deep notched quasi-brittle structures”. In: *Fracture Scaling*. Dordrecht: Springer Netherlands, 1999, pp. 379–390.
- [92] J. Li and X. Zhang. “A criterion study for non-singular stress concentrations in brittle or quasi-brittle materials”. In: *Engineering Fracture Mechanics* 73.4 (2006), pp. 505–523.
- [93] Z. P. Bazant. “Crack Band Model for Fracture of Geomaterials”. In: *Proc., 4th Int. Conf. of Numer. Meth. in Geomech* (1982), pp. 1137–1152.
- [94] C. W. Fowlkes. “Fracture toughness tests of a rigid polyurethane foam”. In: *International Journal of Fracture* 10.1 (1974), pp. 99–108.
- [95] Z. P. Bazant and J. Planas. *Fracture and size effect in concrete and other quasi-brittle materials*. CRC Press, 1998, p. 616.
- [96] L. Marsavina et al. “Refinements on fracture toughness of PUR foams”. In: *Engineering Fracture Mechanics* 129. September 2014 (2014), pp. 54–66.
- [97] Z. P. Bazant et al. “Size effect and asymptotic matching analysis of fracture of closed-cell polymeric foam”. In: *International Journal of Solids and Structures* 40 (2003), pp. 7197–7217.
- [98] Z. P. Bazant, I. M. Daniel, and L. Zhengzhi. “Size Effect and Fracture Characteristics of Composite Laminates”. In: *Journal of Engineering Materials and Technology* 118. July (1996), pp. 317–324.
- [99] Z. P. Bazant et al. “Size effect in fracture of sandwich structure components: Foam and laminate”. In: *American Society of Mechanical Engineers, Applied Mechanics Division, AMD* 248 (2001), pp. 19–30.
- [100] M. R. Ayatollahi and J. Akbardoost. “Size effects on fracture toughness of quasi-brittle materials - A new approach”. In: *Engineering Fracture Mechanics* 92 (2012), pp. 89–100.
- [101] J. Rice. “Limitations to the small scale yielding approximation for crack tip plasticity”. In: *Journal of the Mechanics and Physics of Solids* 22.1 (1974), pp. 17–26.
- [102] D. Gardezabal, Z. He, and A. Kotousov. “On influence of non-singular stress states on brittle fracture”. In: *International Journal of Fracture* 185.1-2 (2014), pp. 201–208.
- [103] B. Kumar, S. Chitsiriphanit, and C. T. Sun. “Significance of K-dominance zone size and nonsingular stress field in brittle fracture”. In: *Engineering Fracture Mechanics* 78.9 (2011), pp. 2042–2051.
- [104] Y. J. Chao, S. Liu, and B. J. Broviak. “Brittle fracture: Variation of fracture toughness with constraint and crack curving under mode I conditions”. In: *Experimental Mechanics* 41.3 (2001), pp. 232–241.
- [105] D. J. Smith, M. R. Ayatollahi, and M. J. Pavier. “On the consequences of T-stress in elastic brittle fracture”. In: *Proceedings of the Royal Society A: Mathematical, Physical and Engineering Sciences* 462.2072 (2006), pp. 2415–2437.
- [106] K. Sedighiani et al. “The effect of T-stress on the brittle fracture under mixed mode loading”. In: *Procedia Engineering* 10 (2011), pp. 774–779.
- [107] M. Rashidi Moghaddam et al. “Mode II brittle fracture assessment using an energy based criterion”. In: *Physical Mesomechanics* 20.2 (2017), pp. 142–148.

-
- [108] M. R. Ayatollahi and J. Akbardoost. “Size effects in mode II brittle fracture of rocks”. In: *Engineering Fracture Mechanics* 112-113 (2013), pp. 165–180.
- [109] M. R. Ayatollahi, J. Akbardoost, and F. Berto. “Size effects on mixed-mode fracture behavior of polygranular graphite”. In: *Carbon* 103 (2016), pp. 394–403.
- [110] M. R. Ayatollahi and M Zakeri. “An improved definition for mode I and mode II crack problems”. In: *Engineering Fracture Mechanics* 175 (2017), pp. 235–246.
- [111] M. Gupta, R. Alderliesten, and R. Benedictus. “A review of T -stress and its effects in fracture mechanics”. In: *Engineering Fracture Mechanics* 134 (2015), pp. 218–241.
- [112] C. T. Sun and H. Qian. “Brittle fracture beyond the stress intensity factor”. In: *Journal of Mechanics of Materials and Structures* 4.April (2009), pp. 743–753.
- [113] O. G. Kravchenko, S. G. Kravchenko, and C.-T. Sun. “Thickness dependence of mode I interlaminar fracture toughness in a carbon fiber thermosetting composite”. In: *Composite Structures* 160 (2017), pp. 538–546.
- [114] L. V. Stepanova, V. S. Dolgikh, and V. A. Turkova. “Digital photoelasticity for calculating coefficients of the Williams series expansion in plate with two collinear cracks under mixed mode loading”. In: *Information Technology and Nanotechnology* (2017).
- [115] L. Stepanova, P. Roslyakov, and P. Lomakov. “A Photoelastic Study for Multiparametric Analysis of the Near Crack Tip Stress Field Under Mixed Mode Loading”. In: *Procedia Structural Integrity*. Vol. 2. 00. 2016, pp. 1797–1804.
- [116] M. R. Ayatollahi, M. M. Mirsayar, and M Dehghany. “Experimental determination of stress field parameters in bi-material notches using photoelasticity”. In: *Materials and Design* 32 (2011), pp. 4901–4908.
- [117] M Guagliano et al. “Multiparameter Analysis Of The Stress Field Around A Crack Tip”. In: *Procedia Engineering* 10 (2011), pp. 2931–2936.
- [118] K Ramesh, S Gupta, and A. Kelkar. “Evaluation of stress field parameters in fracture mechanics by photoelasticity - revisited”. In: *Engineering Fracture Mechanics* 56.1 (1997), 25–41 and 43–45.
- [119] J. Nakamura et al. “Effect of side-groove root configuration on edge fracture on DCB test”. In: *Corrosion 2016 Conference & Expo*. 7155. 2016, pp. 1–11.
- [120] A. Siriruk, D. Penumadu, and K. G. Thomas. “Mixed Mode Fracture Behavior of Cellular Foam Cores Used in Sandwich Structures”. In: *18th International Conference on Composite Materials*. 2011, pp. 1–6.
- [121] E. E. Saenz, L. A. Carlsson, and A. Karlsson. “Characterization of fracture toughness (G_c) of PVC and PES foams”. In: *Journal of Materials Science* 46.9 (2011), pp. 3207–3215.
- [122] J. W. Phillips. *Photoelasticity*. 1998.
- [123] Y. Morioka. “A simple method for determining stress intensity factors for a crack in bi-material interface”. In: *Theses and Dissertations Available from ProQuest* (2010).
- [124] C. Zhou and Z. Li. “The effect of T-stress on crack–inclusion interaction under mode I loading”. In: *Mechanics Research Communications* 34.3 (2007), pp. 283–288.
- [125] Z. P. Bazant. *Scaling laws in mechanics of failure*. 1993.

-
- [126] Z. P. Bazant, Y. Xi, and S. G. Reid. “Statistical size effect in quasi-brittle structures: I. Is Weibull theory applicable?” In: *Journal of Engineering Mechanics* 117.11 (1991), pp. 2609–2622.
- [127] Z. P. Bazant. “Concrete fracture models : testing and practice”. In: *Engineering Fracture Mechanics* 69 (2002), pp. 165–205.
- [128] D. Touliatou and M. A. Wheel. “K-dominance and size effect in mode I fracture of brittle materials with low to medium porosity”. In: *Engineering Fracture Mechanics* (2018).
- [129] M. Ryvkin and O. Hadar. “Employing of the discrete Fourier transform for evaluation of crack-tip field in periodic materials”. In: *International Journal of Engineering Science* 86 (2015), pp. 10–19.
- [130] L. Marsavina et al. “Evaluation of Mixed Mode Fracture for PUR Foams”. In: *Procedia Materials Science* 3.JUNE 2014 (2014), pp. 1342–1352.
- [131] M. S. Cayard and W. L. Bradley. “The effect of various pre-cracking techniques on the fracture toughness of plastics”. In: *ICF7*. Houston (USA), 1989.
- [132] J. M. De Souza et al. “Effect of sample pre-cracking method and notch geometry in plane strain fracture toughness tests as applied to a PMMA resin”. In: *Polymer Testing* 31.6 (2012), pp. 834–840.
- [133] M. Masmoudi et al. “Modeling of the effect of the void shape on effective ultimate tensile strength of porous materials: Numerical homogenization versus experimental results”. In: *International Journal of Mechanical Sciences* 130 (2017), pp. 497–507.
- [134] E. Amsterdam et al. “The Influence of Cell Shape Anisotropy on the Tensile Behavior of Open Cell Aluminum Foam”. In: *Advanced Engineering Materials* 10.9 (2008), pp. 877–881.
- [135] H Benouali, A et al. “Investigation on the influence of cell shape anisotropy on the mechanical performance of closed cell aluminium foams using micro-computed tomography”. In: *Journal of Materials Science* 40 (2005), pp. 5801–5811.
- [136] Y. Mosleh et al. “Effect of polymer foam anisotropy on energy absorption during combined shear-compression loading”. In: *Journal of Cellular Plastics* 54.3 (2018), pp. 597–613.
- [137] K. Vanden Bosche et al. “Anisotropic polyethersulfone foam for bicycle helmet liners to reduce rotational acceleration during oblique impact”. In: *Proceedings of the Institution of Mechanical Engineers, Part H: Journal of Engineering in Medicine* 231.9 (2017), pp. 851–861.
- [138] X. Gao, T. Wang, and J. Kim. “On ductile fracture initiation toughness: Effects of void volume fraction, void shape and void distribution”. In: *International Journal of Solids and Structures* 42.18-19 (2005), pp. 5097–5117.
- [139] M. R. Ayatollahi, M. J. Pavier, and D. J. Smith. “Determination of T -stress from finite element analysis for mode I and mixed mode I / II loading”. In: *International Journal of Fracture* 4505 (1998), pp. 283–298.
- [140] Z. G. Yang et al. “Study on the mechanical properties of hybrid reinforced rigid polyurethane composite foam”. In: *Journal of Applied Polymer Science* 92.3 (2004), pp. 1493–1500.
- [141] J. W. Leggoe, X. Z. Hu, and M. B. Bush. “Crack tip damage development and crack growth resistance in particulate reinforced metal matrix composites”. In: *Engineering Fracture Mechanics* 53.6 (1996), pp. 873–895.

- [142] M. Isida. “On the determination of stress intensity factors for some common structural problems”. In: *Engineering Fracture Mechanics* 2.1 (1970), pp. 61–79.
- [143] R. Evans et al. “Improved stress intensity factors for selected configurations in cracked plates”. In: *Engineering Fracture Mechanics* 127 (2014), pp. 296–312.
- [144] X. Z. Hu and F. H. Wittmann. “Fracture energy and fracture process zone”. In: *Materials and Structures* 25.6 (1992), pp. 319–326.
- [145] T. Davis et al. “Stress concentrations around voids in three dimensions: The roots of failure”. In: *Journal of Structural Geology* 102 (2017), pp. 193–207.